Title: Performance Enhancement for LTE and Beyond Systems

Name: Wei Li

Performance Enhancement for LTE and Beyond Systems

Wei Li
Institute for Research in Applicable Computing
University of Bedfordshire

A thesis submitted to the University of Bedfordshire in fulfilment of the requirements for the degree of Doctor of Philosophy

September 2014

Abstract

Wireless communication systems have undergone fast development in recent years. Based on GSM/EDGE and UMTS/HSPA, the 3rd Generation Partnership Project (3GPP) specified the Long Term Evolution (LTE) standard to cope with rapidly increasing demands, including capacity, coverage, and data rate. To achieve this goal, several key techniques have been adopted by LTE, such as Multiple-Input and Multiple-Output (MIMO), Orthogonal Frequency-Division Multiplexing (OFDM), and heterogeneous network (HetNet). However, there are some inherent drawbacks regarding these techniques. Direct conversion architecture is adopted to provide a simple, low cost transmitter solution. The problem of I/Q imbalance arises due to the imperfection of circuit components; the orthogonality of OFDM is vulnerable to carrier frequency offset (CFO) and sampling frequency offset (SFO). The doubly selective channel can also severely deteriorate the receiver performance. In addition, the deployment of Heterogeneous Network (HetNet), which permits the co-existence of macro and pico cells, incurs inter-cell interference for cell edge users. The impact of these factors then results in significant degradation in relation to system performance.

This dissertation aims to investigate the key techniques which can be used to mitigate the above problems. First, I/Q imbalance for the wideband transmitter is studied and a self-IQ-demodulation based compensation scheme for frequency-dependent (FD) I/Q imbalance is proposed. This combats the FD I/Q imbalance by using the internal diode of the transmitter and a specially designed test signal without any external calibration instruments or internal low-IF feedback path. The instrument test results show that the proposed scheme can enhance signal quality by 10 dB in terms of image rejection ratio (IRR).

In addition to the I/Q imbalance, the system suffers from CFO, SFO and frequency-time selective channel. To mitigate this, a hybrid optimum OFDM receiver with decision feedback equalizer (DFE) to cope with the CFO, SFO and doubly selective channel. The algorithm firstly estimates the CFO and channel frequency response (CFR) in the coarse estimation, with the help of hybrid

classical timing and frequency synchronization algorithms. Afterwards, a pilot-aided polynomial interpolation channel estimation, combined with a low complexity DFE scheme, based on minimum mean squared error (MMSE) criteria, is developed to alleviate the impact of the residual SFO, CFO, and Doppler effect. A subspace-based signal-to-noise ratio (SNR) estimation algorithm is proposed to estimate the SNR in the doubly selective channel. This provides prior knowledge for MMSE-DFE and automatic modulation and coding (AMC). Simulation results show that this proposed estimation algorithm significantly improves the system performance. In order to speed up algorithm verification process, an FPGA based co-simulation is developed.

Inter-cell interference caused by the co-existence of macro and pico cells has a big impact on system performance. Although an almost blank subframe (ABS) is proposed to mitigate this problem, the residual control signal in the ABS still inevitably causes interference. Hence, a cell-specific reference signal (CRS) interference cancellation algorithm, utilizing the information in the ABS, is proposed. First, the timing and carrier frequency offset of the interference signal is compensated by utilizing the cross-correlation properties of the synchronization signal. Afterwards, the reference signal is generated locally and channel response is estimated by making use of channel statistics. Then, the interference signal is reconstructed based on the previous estimate of the channel, timing and carrier frequency offset. The interference is mitigated by subtracting the estimation of the interference signal and LLR puncturing. The block error rate (BLER) performance of the signal is notably improved by this algorithm, according to the simulation results of different channel scenarios.

The proposed techniques provide low cost, low complexity solutions for LTE and beyond systems. The simulation and measurements show good overall system performance can be achieved.

Acknowledgements

Firstly, I would like to thank my supervisor, Dr. Yue Zhang and Dr. Vladimir Dyo, for their guidance and invaluable comments. I would also like to thank Professor Edmond C. Prakash and Dr. Dayou Li for their advice during my research period in Bedfordshire. Special thanks goes to Dr. Li-Ke Huang, Dr. Hong Wei and Kexuan Sun for their valuable input into discussions, and suggestions, relating to my thesis.

The financial support for this work was provided by Aeroflex Ltd. as part of their student research program and this is hereby acknowledged.

Finally, I would like to express my gratitude to my parents and brother for their inexhaustible love, support and encouragement.

Contents

List of Figures

List of Tables

Abbreviations

3GPP	3rd Generation Partnership Project
ABS	Almost Blank Subframe
AMC	Adaptive Modulation and Coding
AWGN	Additive White Gaussian Noise
BLER	Block Error Rate
CDMA	Code Division Multiple Access
CIR	Channel Impulse Response
CoMP	Coordinated Multipoint Transmission
CP	Cyclic Prefix
CQI	Channel Quality Indicator
CRS	Cell Specific Reference Signal
DAC	Digital-to-Analog Convert
DCI	Downlink Control Information
DCT	Direct conversion transmitter
DFE	Decision feedback equalizer
DSP	Digital Signal Processing
EDGE	Enhanced Data rates for GSM Evolution
EPA	Extended Pedestrian A model
ETU	Extended Typical Urban model
EVA	Extended Vehicular A model
eICIC	Enhanced Inter Cell Interference Coordination
FD	Frequency-Dependent
FDD	Frequency-Division Duplexing
FDM	Frequency Division Multiplexing
FDMA	Frequency division multiple access
FEC	Forward Error Correction
FeICIC	Further eICIC
FI	Frequency-Independent
FM	Frequency modulation
GI	Guard Interval

GPRS	General Packet Radio Service
GSM	Global System for Mobile
HetNet	Heterogeneous Network
HSPA	High Speed Packet Access
ICI	Inter-Carrier Interference
IF	Intermediate Frequency
IFFT	Inverse Fast Fourier Transform
IRR	Image Rejection Ratio
ISI	Inter-Symbol Interference
LLR	Log-Likelihood Ratio
LO	Local oscillator
LPF	Lowpass Filter
LTE	Long term Evolution
MAC	Media Access Control
MIMO	Multiple-Input and Multiple-Output
OFDM	Orthogonal Frequency-Division Multiplexing
OFDMA	Orthogonal Frequency-Division Multiple Access
SNR	Signal-to-Noise Ratio
SSS	Secondary Syncrhonization Signal
STO	Symbol Timing Offset
PAR	Peak-to-Average Ratio
PBCH	Physical Broadcast Channel
PCFICH	Physical Control Format Indicator Channel
PCH	Physical Channel
PDCCH	Physical Downlink Control Channel
PDCP	Packet data Convergence Protocol
PDF	Probability Density Function
PDP	Power Delay Profile
PDSCH	Physical Downlink Shared Channel
PHICH	Physical Hybrid ARQ Indicator Channel
PHY	Physical Layer
PMCH	Physical Multicast Channel

PMI	Precoding Matrix Indicator
PSD	Power Spectrum Density
PSS	Primary Synchronization Signal
QAM	Quadrature amplitude modulation
RAN	Radio Access Network
RCL	Radio Link Control
RB	Resource Block
RE	Resource Element
RI	Rank Indicator
RRC	Radio Resource Control
SINR	Signal-to-Interference plus Noise Ratio
SNR	Signal-to-Noise Ratio
STBC	Space-Time Block Coding
TB	Transport Block
TDD	Time-Division Duplexing
TDL	Tapped Delay Line
TTI	Transmission Time Interval
UE	User Equipment
UMTS	Universal Mobile Telecommunications System
WLAN	Wireless Local Area Network
W-CDMA	Wideband Code Division Multiple Access

1. Introduction

1.1 Research background

Due to the rapid development of hardware and signal processing theory, the last few years have witnessed a tremendous growth in the wireless communication industry. The amount of mobile users was 6.62 billion globally in 2013, and ownership ratio of mobile handsets was 93.1%. In contrast to this, the figures in 2008 were, respectively, 4.1 billion and 61% [1]. In addition, there is a clear trend implying fixed-communication will shift to mobile communication.

The inherent motivation for this trend can be attributed to a variety of factors. Because of the development of the very-large-scale integration circuits (VLSI), hardware is much more powerful in terms of computation capability, noise performance, and dynamic range, which enables hardware platforms to support much higher transmission data rates, signal bandwidth, transmission power, and receiver sensitivity. In addition, improvements in electronics technology have provided lower cost, lower power consumption, and smaller sizes, which affords electronic equipment users a much better mobility experience. On the other hand, the increasing demand for ubiquitous access to networks in both stationary and mobile scenarios has continuously required more sophisticated equipment. The demand for higher data rates, and denser equipment also drives the development of wirelss communication systems in the direction of high data throughput, and better user experience. The development of wireless communication systems can be divided into four stages, according to techniques and services:

First generation (1G): The first generation system began operation in the 1970s and used analog transimssion for voice services. Different systems were deployed, for example, NMT and TACS in Europe, and AMPS in North America. These systems adopt techniques such as freqeuncy modulation (FM), directional

antennas, handover and roaming and frequency division multiple access (FDMA) which support data rate less that 100 kbps [2], [3].

Second generation (2G): The second generation system was launched at the beginning of the 1980s. Compared with 1G, 2G systems are mostly based on circuit-switched technology. The most popular 2G system is the Global System for Mobile Communication (GSM), which makes use of spectrum resource by splitting the frequency spectrum into several 200 KHz bandwidth channels. In addition, GSM also adopts Time Division Multiple Access (TDMA), which allows more users to access frequency resources. In addition to GSM technology in Europe, Code Division Multiple Access (CDMA) technology was developed in North America, which increased network capacity and provided clearer voice quality. 2G has seen the introduction of General Packet Radio Service (GPRS) and Enhanced Data rates for GSM Evolution (EDGE) to cope with the demand for higher data rates and voice services. These technologies have enabled data rates to reach 150 kbps and 384 kbps respectively [4].

Third Generation (3G): Aiming to provide a high speed data service, global accessibility and high capacity, the International Telecommunication Union defined International Mobile Telecommunications-2000 (IMT-2000) as 3G technology. Due to reasons regarding different technical routes and business policies, IMT-2000 has included a variety of systems in different areas: UMTS in Europe, W-CDMA as the evolution of GSM, TD-SCDMA based on CDMA, CDMA2000, and so forth. A variety of techniques are adopted in these systems including adaptive modulation & coding (AMC), Orthogonal Transmit Diversity (OTD), Space Time Spreading (STS), and virtual soft handoff. These techniques result in a peak data rate of up to 2 Mbps for stationary users. An essential definition of 3G is that it relates to different technologies and these technologies are moving towards a converged worldwide network.

Fourth Generation (4G): 4G technology long term evolution (LTE) will try to integrate almost every wireless standard in use and provide an enhanced user

experience. In this system, the user will have ubiquitous access to the network and multiple varieties of services at a low cost. Accordingly, the 3rd Generation Partnership Project (3GPP) proposed some key requirements: data rate ranges from 500-100 Mbps for high mobility users to Gbps for low mobility users; mobility up to 350 km/h, scalable bandwidth and spectrum aggregation (Release 11) with bandwidths of more than 40 MHz. In order to achieve these goals, the first LTE release (Release 8) adopted some key techniques including: Multi-input and multiple-output (MIMO) antenna, Orthogonal Frequency-Division Multiple Access (OFDMA) in downlink, inter-cell interference mitigation, Adaptive Modulation and Coding (AMC) depending on radio link quality, and an all-IP based network. The 4G network has been deployed all over the world and provides a new level of user experience.

LTE is evolving along the lines of high data rate, high mobility, high energy efficiency, and low cost. The LTE beyond system is expected to provide 1000 fold increase in network capacity [5]. The technologies in systems beyond LTE will comprise better local area access, enhanced multi-antenna, machine-type communication (MTC), and device-to-device communication. In order to realize this, heterogeneous networks, which consist mainly of macro cells and complementary low-power cells will be deployed, which is a further densification of the network. Multi-antenna enhancement technologies, including elevation beamforming, and massive MIMO will be adopted. Coordinated multipoint transmission/reception will be introduced to improve coverage and reduce inter-cell interference.

Aside from these long range communication technologies, varieties of short range communication standards have also been developed. The Wireless Personal Area Network (WPAN) was established to address wireless networks of mobile and portable computing devices. WPAN makes uses of some advanced technologies to provide interconnection between different kinds of communications devices within a short range. Bluetooth and Zigbee [6] are the two main WPAN standards. Bluetooth is designed to interconnect mobile devices with relatively low cost and

low data rate (2-3Mpbs). The Zigbee provides lower data rate (20-250 kpbs) and is widely used in low power scenarios such as wireless sensor networks [7]. On the other hand, a Wireless Local Area Network (WLAN) is intended to link several devices with a high data rate. In order to achieve a high data rate, WLAN adopts techniques such as OFDM, MIMO, and carrier aggregation. A typical WLAN standard is 802.11n which supports up to a 300 Mpbs data rate [8]. Similar to LTE, the WiMax standard was proposed to provide low delay, large coverage and high real-time throughput. The latest version of WiMax supports up to a 365 Mbps data rate with 2×40 Mhz bandwidth. WiMax adopts some similar technologies as in LTE, such as OFDM, carrier aggregation, and MIMO [9].

Fig. 1.1 gives an overview of the evolution of different communication standards. These standards are defined by standardization bodies, such as: IEEE, Standardization of Information and Communication Technology and Consumer Electronics (ECMA), European Telecommunications Standards Institute (ETSI), and the International Telecommunication Union (ITU). It can be seen from this figure that all wireless communication technologies are evolving towards high speed and high mobility. And there is also an evident trend that different wireless technologies are merging together.

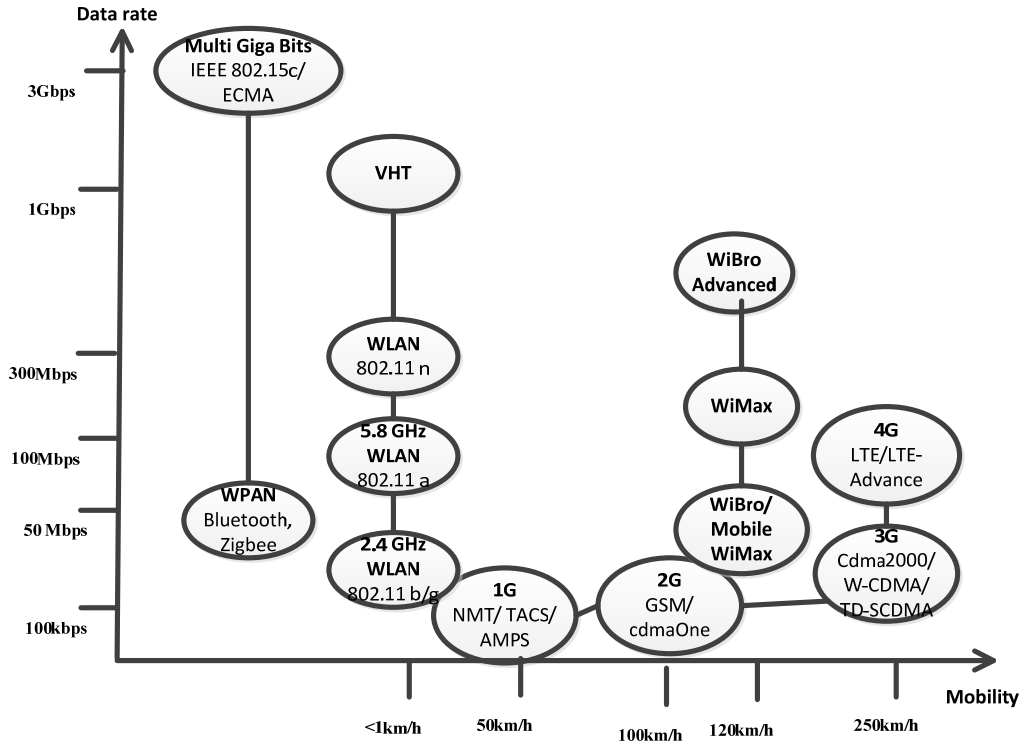

Figure 1.1 The Evolution of Wireless Communication Systems

Problems arise when new techniques are applied to different systems. In direct conversion-based architectures, the transceiver suffers from a mismatched frequency response on the inphase and quadrature signal branches, namely, I/Q imbalance. The timing/frequency difference between transmitter and receivers results in symbol timing offset (STO), carrier frequency offset (CFO) and sampling frequency offset (SFO). In addition, the inter-cell interference between neighbouring cells is more severe as the cell density increases. The aim of this dissertation is to investigate and propose solutions for these problems in LTE and beyond systems. Though wireless systems are evolving in different directions, they adopt similar techniques to some extent, such as OFDM, MIMO, and direct conversion transmitters. Hence, the proposed algorithms can also be applied to other systems.

1.2 Research problem

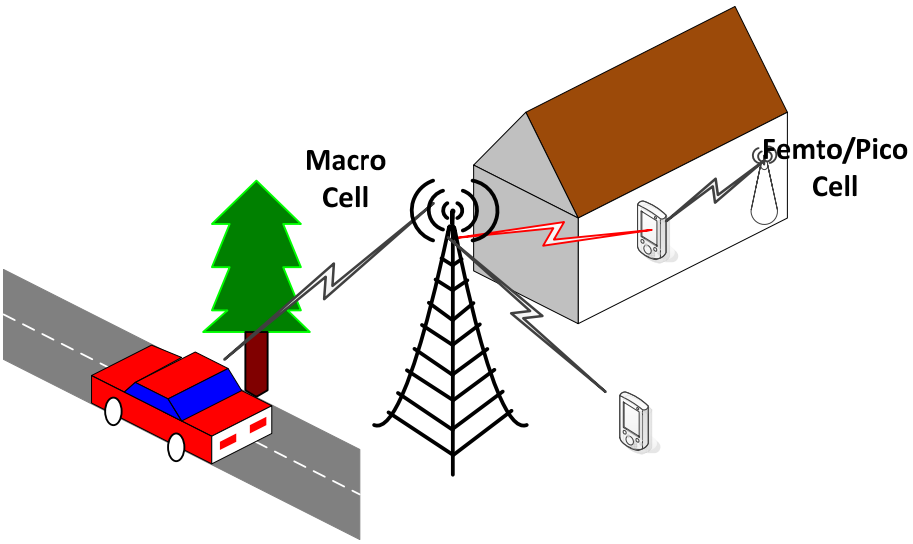

Figure 1.2 Typical LTE Network.

To achieve high capacity, a high data rate, and good quality of service in LTE, the 3GPP has proposed a variety of techniques including MIMO, OFDMA, AMC, and heterogeneous networks. Fig. 1.2 presents a typical heterogeneous LTE network in which a macro cell and femto/pico cell coexist [10], [11]. In this network, multimedia/voice services are delivered by the radio link between macro cell and user equipment (UE). To complement the conventional macro cell, low power pico/femto cells also provide an LTE connection with a much smaller coverage, which increases system capacity and extends system coverage [12]. However, there exist many problems when implementing such a system in the real world. This section will describe research problems in two aspects: I/Q imbalance and receiver algorithm.

1.2.1 I/Q imbalance

I/Q imbalance is mainly caused by hardware impairments of transceivers, which is a common problem in wireless transceivers. One goal of this thesis is to investigate into the transmitter I/Q problem.

Direct conversion transmitter is adopted due to its low cost, low complexity and flexibility [13], [14], [15], [16], [17]. The direct conversion transmitter (DCT) utilizes the non-Hermitian symmetry property of the complex signal in the

frequency domain, and modulates this complex signal by suppressing the image frequency components around the carrier frequency. Ideally, the real and imaginary part of the baseband complex signal is modulated by a pair of quadrature mixers on the inphase and quadrature branch respectively. Theoretically, the image frequency components around the carrier frequency can be completely eliminated by adding the modulation results of the two branches. However, the nonideal hardware devices result in a mismatch on the two branches [18], [19]:

1). DAC and low pass filters on the baseband modules bring mismatched amplitude and phase delay due to non-linearity.

2). The two local oscillators (LO) of the mixer do not have the same amplitude and 90° phase difference.

3). The RF amplifier and radio signal path on the two branches exhibit asymmetric frequency responses around the carrier frequency. For narrowband system, this results in FI I/Q imbalance. Whereas for wideband system, this results in FD I/Q imbalance, as shown in Fig. 1.3. The criterion for I/Q imbalance is Image Rejection Ratio (IRR). For FI I/Q imbalance, the IRR is a constant over the whole frequency band. Whereas for FD I/Q imbalance, the IRR varies over different frequency points. For uncalibrated DCTs, the typical IRR is 25~40 dB [20], [21]. For a double sideband system, the superposition of image and desired frequency components decreases signal quality, which causes considerable performance degradation especially for wideband systems such as LTE and WiMax etc.

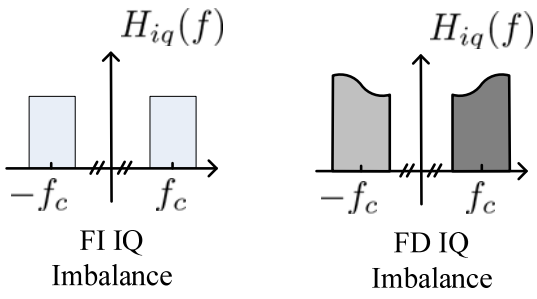

Figure 1.3 Frequency Response of FD and FI IQ Imbalance

There has been much research into I/Q imbalance calibration. The works in [13], [22], [23] and [24] estimate the I/Q imbalance of the narrow band signal, which relies on the assumption that I/Q imbalance is frequency-independent (FI) within the signal band, whereas the studies in [25], [18], [26] and [27] address FD I/Q imbalance which is common in wideband DCTs. In terms of realization architecture, the transmitters in [22], [13] and [28] utilize a diode or power detector circuit to estimate the I/Q imbalance. This architecture usually requires predefined test tones, which indicates the estimation is off-line. Besides, low-IF architecture is most popular in I/Q calibration [25], [26] and [27]. In this architecture, the external down converter and ADC forms a low-IF receiver. Due to this extra receiver, on-line estimation can be realized.

For the aforementioned diode based approaches, test signals are generated by the transmitter, and the output of the diode or power-detector is sampled by the ADC. These kinds of methods make use of the square law of the diode. Because it assumes the I/Q imbalance is FI, the target estimation parameters are only the LO mismatch and DC offset.

In [29], the author transmits a two-tone signal and the output of the diode carries the information pertaining to the LO mismatch. The two-tone signal modulates with itself in the diode. The output signal can be represented by an information array of LO and DC offset parameters. Then, this information matrix can be estimated by using Least Square (LS) methods. This method brings reasonable image suppression improvement within a 5 MHz bandwidth. However, it requires considerable computation resources when the sampling data increases as the LS methods employ a matrix inversion operation. Based on the same feedback path, the author proposes the low computation complexity method in [22], The output of the diode is a monotonic function . Hence, the author proposes to calibrate such DC offsets by iteratively tuning the input to DC level. Similarly, the gain has a straightforward influence on the diode output. Hence, the gain imbalance can be calibrated in the same way. For phase imbalance, the output of the diode is an ellipse function of phase error, which indicates the phase error is calculated by

solving different sampled ellipse functions. In general, the diode based method provides a low cost solution for LO I/Q imbalance. However, it is a constraint to narrow the band signal.

For low-IF based methods, an external receiver or internal feedback path which consists of a downconverter, ADC, and digital signal processor (DSP), is introduced to measure the I/Q imbalance parameters. The RF signal is downconverted to low intermediate frequency (IF) and then digitized by the ADC. The digital signal is then I/Q demodulated by digital I/Q demodulator, which enables it to measure the wideband FD I/Q imbalance.

In [22], the I/Q imbalance is calibrated pair-by-pair which assumes there are no image components during the calibration stage. In [25], only the mismatch of DAC and signal path is considered, whereas the mismatch of LO is assumed to be ideal. These methods make use of wideband receiver and design special test signals. Apart from this, [18] and [26], the cross-processing between I and Q signal and LS methods are used to estimate the imbalance parameters. These approaches are applicable to the majority signal which indicates on-line calibration can be realized. [18] studies the second-order statistics of the complex random signal and takes into account the overall frequency response of the internal feedback path. A widely linear (WL) LS method is proposed in which the FD I/Q parameters are calculated by applying the pseudo-inverse of the transmitted signal matrix. This method provides a flat 75 dB image rejection ratio within a 10 MHz bandwidth. However, an ill conditioning matrix can happen when the signal is narrowband. In general, low-IF based methods provide a good on-line solution to calibrate an FD I/Q imbalance which is crucial for wideband systems such as LTE, DVB and WiMax . However, the cost and implementation complexity is relatively high because an extra downconverter and IF frequency source are introduced.

In summary, there still exist some problems for both diode and low-IF based I/Q imbalance compensation schemes:

1). For diode based schemes, it can effectively measure the I/Q imbalance at low cost. Because the power detection in most DCTs is a low pass filter, the output of diode will be constraint to narrowband. Hence, the conventional diode based I/Q imbalance estimation schemes loss the wideband I/Q imbalance information.

2). For low-IF based schemes, the low-IF receiver can effectively estimate wideband I/Q imbalance. However, the cost will be high, because extra mixer and LO is introduced.

This paper aims to propose a low wideband (FD) I/Q imbalance compensation scheme that makes use of cost diode, which will be presented later.

1.2.2 Receiver algorithm

The received signal on the receiver side may experience severe deterioration due to a variety of influences:

1). As shown in Fig. 1.2, the propagation condition of the RF signal is complex. Due to multi path effects and reflections, the replicates of the transmitted signal, with different amplitude and phase delay, will arrive at the receiver side simultaneously. As a result, the channel exhibits a frequency selective fading [21], [30] and [31]. For UEs that are moving, the channel condition may change rapidly due to the Doppler effect. As a result, the channel will be time-varying as well [32]. For OFDM systems, this induces Inter-Symbol Interference (ISI) and Inter-Carrier Interference (ICI) [33].

2). Nonideal frequency sources generate different reference frequencies at the transmitter and receiver side. In addition, the reference frequency will drift with varying temperature and unstable power supply. Hence, the unsynchronized reference frequency causes CFO and SFO, which destroy the orthogonality among all sub-carriers of the OFDM signal. This results in ICI [34]. For LTE UEs, the typical CFO is 25 KHz, which is ±1.67 subcarrier spacing with an SFO of about 10 ppm [35]. Besides this, there exists a timing offset. As the OFDM signal is

transmitted symbol by symbol, the receivers usually have no prior information about when the symbols start. This induces a timing offset which significantly influences the following signal demodulation process [21].

Much literature examines these problems. The majority of research treats the influence of CFO and a fading channel jointly, see [36], [37] and [38]. In [37], the channel is modelled by a basis expansion model (BEM) to reduce the amount of estimation parameters. The CFO ad BEM coefficients are jointly estimated by a pilot-based maximum a posteriori (MAP) technique. An iterative soft decoder is adopted to improve performance. This algorithm achieves close to the ideal performance. Similarly, [36] proposes a recursive least-square (RLS) method to estimate CFO, SFO and channel impulse response (CIR) jointly. A simple maximum-likelihood (ML) estimator provides a coarse estimation of CFO and SFO based on the training signal. The coarse estimation results are then fed into a fine estimator, where the CIR, CFO and SFO is estimated by optimizing the LS cost function on the corresponding pilot tones. Though the BEM model and ML method help to reduce estimation parameters, the MAP algorithm and cost function optimization consume considerable computation resources to achieve good performance. This class of joint estimation approaches mainly makes use of a certain cost or probability function, which requires iterative optimization and is computationally heavy. Instead, [39] thoroughly investigates the impact of the above individual impairments: imperfect channel estimation, STO, CFO and SFO. An optimization criterion based on SNR loss is developed. And the minimum requirements on each module are systematically derived. Based on the results in [39], [40] designs a complete receiver to cope with the above impairments. The impact of synchronization algorithms and complexity is qualitatively analysed. As the LTE system is evolving in the direction of high data rate, high mobility, an optimum receiver is required. These two pieces of research provide a good reference point for the receiver algorithm design in this dissertation.

The estimation error contributes to the ICI and ISI [39]. A robust equalizer is required to mitigate this impact. Equalizers can be categorized into zero-forcing

equalizer (ZFE), minimum mean square error linear (MMSE-LE) and decision-feedback equalizers (MMSE-DFE) [41]. ZFE provides simple architecture but often limited effectiveness. MMSE-LE and MMSE-DFE is more widely used because of higher performance. MMSE-LE performs better than ZFE because of noise enhancement in which coloured noise will be whitened. MMSE-DFE exhibits superior BER performance compared to linear equalizers such as ZFE and MMSE-LE [42]. [41] presents a serial MMSE-DFE which is suitable for serial QAM modulation. It makes use of the statistics of serial channel information and yields good performance. However, this is not suitable for block transmission such as OFDM in LTE systems. [43], [44] and [42] investigates the MMSE-DFE in block transmission. The MMSE-DFE is derived using the orthogonal principle and MMSE criteria based on the assumption that the feedback filter is upper triangular. However, these approaches are computationally heavy, for it calculates the feedback and feedforward filters through Cholesky factorization.

SNR provides channel and signal condition criteria to channel equalizers. The most popular SNR estimation algorithm is the moving average method [45]. However, the method is inaccurate in time variant channel in LTE system. The data-aided methods in [46] and [47] realize accurate SNR estimation, which requires a specially designed data sequence. [47] proposes a subspace-based algorithm which is robust in time variant channel. However, it is not compatible with LTE pilot structures: the accuracy decreases when the signal is narrowband or assigned to distributed resource blocks. Hence, a robust SNR estimation algorithm is required in this context. To sum up, many problems arise and cause significant performance degradation when an LTE OFDM receiver is applied to a high mobility and complexity environment.

Apart from the above impairments caused by the channel and transceiver, there exists interference from other cells. As shown in Fig. 1.2, the UEs in heterogeneous LTE can acquire service via pico/femto cells due to reasons of data traffic offloading, lower system power or range extension [48], [49]. However,

when the UE is served by one cell, e.g. pico/femto, it still receives a signal from macro cells when it is located in the cover of the macro cell. This inter-cell interference severely degrades signal quality. Though an enhanced inter-cell interference cancellation (eICIC) scheme is proposed after LTE Release 10 [50], the UE suffers from residual cell specific reference signal (CRS) interference [51]. Solutions such as direct CRS cancellation, data muting and LLR puncturing are studied in [52] and [53], which reveals direct CRS cancellation, achieving superior interference cancellation (IC) performance. [54] and [55] proposes two methods that make use of a classical channel estimation algorithm. However, these methods are suitable for a non-synchronized interference signal.

In summary, the problems this thesis will address are:

1). Though there exists some receiver algorithms, the receiver in 5G will still face CFO, SFO, STO and channel problems. In terms of complexity and verification, these algorithms are still complex to be implemented in DSP or FPGA.

2). For fast fading channel, it still requires an accurate SNR estimation algorithm to support further equalization in receiver.

3). For future heterogeneous network, the receiver may face severe inter-cell interference. Though ABS scheme is proposed to alleviate this, the remaining CRS still cause interference.

These problems are crucial for LTE system performance. This dissertation deals with the above problems with low cost and high performance solutions. The other effects of transceiver nonidealities, such as non-linearity of amplifier, receiver I/Q imbalance, are out of the scope of this dissertation.

1.3 Objectives and solution approach

The overall objective of this dissertation is to provide solutions that optimize LTE transceiver performance. More specifically, the dissertation overcomes the previously mentioned problems with low cost and high performance methods:

1. Develop a low cost automatic I/Q imbalance compensation scheme for DCTs.

In order to reduce the cost of FD I/Q imbalance compensation, diode-based compensation scheme will be adopted. This paper will firstly investigate into the conventional diode-based I/Q imbalance compensation scheme. Then the feasibility of diode-based scheme for FD I/Q imbalance will be discussed. In order to estimation and compensate FD related I/Q imbalance factors, this thesis will investigate DCT hardware impairments and analyze factors that cause I/Q imbalance. This should cover wideband scenarios in which I/Q imbalance is FD. Based on this, FD I/Q imbalance model will be derived for development of I/Q imbalance estimation and compensation algorithm.

A low cost estimation and compensation algorithm that combines the advantage of diode and low-IF schemes will be proposed based on the derived model. The estimation algorithm aims to estimate overall FD I/Q imbalance for any modulation scheme (QPSK, QAM, etc.). It can estimate the amplitude and phase imbalance caused by pure LO. The compensator should be based on a baseband digital signal processing algorithm. It should be able to compensate the FD I/Q imbalance. The whole compensation scheme should be low cost, possess low computational complexity, and be automatic with IRR improvement larger than 10 dB. Because the output of diode contains abundant harmonics, which degrades the estimation performance, this scheme designed single tone for estimation, whereas the conventional low-IF schemes adopt multi-tone estimation. In addition, this scheme does not take the non-linearity of amplified into account. Furthermore, the work will be on joint estimation of I/Q imbalance and non-linearity by designing special training sequence.

2. Develop LTE downlink receiver algorithm with inter-cell interference cancellation capability.

The downlink receiver algorithm should take into account the detrimental effects of CFO, SFO, frequency and time selective channel (doubly selective channel), and timing offset. The downlink receiver algorithm should be able to be applied in typical mobile scenarios, e.g. 25 KHz CFO, 10 ppm SFO, fading channel with 50 Hz Doppler frequency. Apart from this, the receiver should be able to cope with CRS interference from neighbouring cells.

Based on existing algorithms, the hybrid receiver will be developed. This receiver makes use of some conventional frequency/timing synchronization and channel estimation methods, which is able to estimate and compensate timing offset, CFO, SFO, and doubly selective channel with low computational complexity. The computation complexity of these methods are low, which is easy for further implementation and verification. In addition, an MMSE-DFE is derived to alleviate the residual impairments. Unlike the conventional MMSE-DFE that is derived by using matrix factorization, the factors of proposed MMSE-DFE are derived by using Lagrange Multiplier, which reduces the computation burden. Simulation results show that the receiver algorithm give satisfactory performance with low implementation cost. The proposed DFE gives similar performance as the convetional DFE does. However, the simulation also shows that the proposed DFE brings limited performance improvement at the cost of high computation burden.

In order to perform accurate SNR estimation, this thesis proposed a sub-space based SNR estimation algorithm. By doing eigen-decomposition to the covariance matrix of received signal and estimating channel length, the power of signal and noise could be obtained from eigenvalues. In addition, this thesis proposed an inter-cell interference cancellation algorithm. The algorithm firstly makes use of statistics of received signal. The channel response could be estimated then. Afterwards, the interfering signal could be reconstructed and subtracted from the received signal. Simulation results show that the proposed algorithm gives much less estimation error compared with classical sub-space methods over the interested algorithm under different time-varying channels.

The simulation results show that the proposed algorithm is robust for different pilot patterns. However, it shows that this algorithm gives considerable estimation error when larger numbers of pilots is used and SNR is high. It is recommended that less numbers of pilots to be used for SNR estimation, which is more robust and consumes less computation resources.

In addition, this thesis also investigated into the problem of CRS interference in the future heterogeneous networks. The signal structure and interfering channel conditions will firstly be analysed. Then an algorithm that makes of channel statistics is proposed. As the channel in this scenario is slow fading, the interfering channel could be accurately estimated by moving average method. Then the interfering signal could be locally reconstructed and subtracted from the received signal. Simulation results show that this algorithm significantly improves the block error rate (BLER) performance under different channels and MCS. It also shows that this method is robust to timing and frequency error at the cell edge. This method estimates timing and frequency error by using synchronization symbols, where the number of synchronization symbols is limited. Hence there could be an issue that inaccurate timing and frequency estimation is conducted when SNR is low. Future work will be on accurate timing and frequency synchronization by making use of pilot symbols.

Although there exist I/Q imbalance compensation schemes and wireless receiver algorithms in many literatures [13, 18, 19, 21, 32, 37, 39], this dissertation will present innovative, low cost and high performance solutions for LTE transceivers, detailed in the following chapters.

1.4 Outline of the thesis

The structure of this dissertation and its major contributions are:

Chapter 2 presents a general overview of a system model for LTE downlink physical layer. The model takes into account the important aspects of LTE downlink communication link. A brief overview of typical LTE transceiver

architecture, along with some of the most common hardware impairments, is presented including the principle of DCT transmission, I/Q imbalance, and frequency offsets. Then, the frequency-time selective channel model in different propagation scenarios is introduced. The LTE physical layer standards and the existing eICIC scheme are presented. The research in the subsequent chapters will be based on these models.

Chapter 3 focuses on the DCT I/Q imbalance compensation scheme. The FD I/Q imbalance model will be derived to develop a novel estimation algorithm. The characteristics of transmitter devices such as mixer, and power detector, will be analyzed in detail. The principles of conventional estimation methods will be presented and analysed. Based on this, a self-IQ-demodulation based estimation method is developed which only requires a transmitter's internal power detector and ADC. Accordingly, the corresponding test tone and hardware requirements will be studied. It will be shown how the LO imbalance parameters and other nonideal devices can be separately estimated. The FD baseband compensator will also be introduced. Finally, the overall performance of the proposed scheme will be assessed using a computer and laboratory instruments.

Chapter 4 investigates the optimum OFDM receiver for the LTE downlink receiver. The impact of CFO, SFO and doubly selective channel will be presented. Then, a hybrid estimation scheme is proposed. Within this scheme, joint estimation algorithms will be adopted to deal with the impact of CFO, SFO, and doubly-selective channel. A low cost minimum mean square error (MMSE) decision feedback equalizer (DFE) is developed to minimize the error. In addition, an FPGA-based co-simulation platform is built to speed up the algorithm verification process. The overall performance of the whole compensation scheme is verified by computer simulation and the co-simulation platform.

Chapter 5 proposes a subspace-based noise estimation algorithm for time-varying channels. The requirements for SNR estimation in LTE systems are analyzed and it will be shown that the conventional moving average based SNR estimation

method gives biased estimation in time-variant channels. The eigenvalue decomposition for the signal correlation matrix shows that the received signal space can be divided into signal space and noise space. Signal and noise power is projected into these two spaces. The MDL method and modified MDL method is applied to estimate the noise power. Simulation results verify the robustness of this method.

Chapter 6 presents another contribution, which aims to alleviate the CRS interference. The CRS interference scenario and the major factors of CRS interference on the receiver side will be represented. The dominant STO and CFO are compensated by exploiting the synchronization channel. Then, the statistics of the interfering channel of the neighbouring cell will be investigated, according to the information of the LTE control channel. Based on this, an interference reconstruction and a cancellation algorithm are proposed. Computer simulation verifies the effectiveness of this proposed algorithm in different scenarios.

Chapter 7 concludes the contributions of this dissertation and puts forward potential further research directions.

1.5 Main contributions

The main contributions of this thesis are to:

1. Designed a new FD I/Q imbalance calibration scheme for DCTs. Achieved satisfactory performance for both, and narrowband signals. Reduced the overall feedback cost. Verified the feasibility of using a self-IQ-demodulation method to calibrate I/Q imbalance and other non-linear distortions.

2. Designed a computationally low complexity OFDM receiver which adopts the simplified MMSE-DFE. Designed a co-simulation platform and speed up the algorithm verification process.

3. Proposed a robust SNR estimator for flexible pilot allocation scenarios for a time variant channel.

4. Proposed a robust CRS interference cancellation algorithm that is robust for timing and synchronization errors.

1.6 Papers published and submitted

The following papers and reports have been published and submitted to journals, conferences and companies, that report the results of this thesis:

1. **Wei Li**, Yue Zhang, Li-Ke Huang, Jian Xiong, C. Maple, "Diode-based IQ imbalance estimation in direct conversion transmitters", Electronics Letters, Vol. 50, Issue 5, pp. 409-411 Feb, 2014
2. **Wei Li**, Yue Zhang, Li-Ke Huang, C. Maple, J. Cosmos, "Implementation and Co-Simulation of Hybrid Pilot-Aided Channel Estimation With Decision Feedback Equalizer for OFDM Systems", IEEE transaction on Broadcasting, Vol 58, Issue 4, pp. 590-602, Dec. 2012
3. **Wei Li**, Yue Zhang, Li-ke Huang, Jin Wang, John Cosmas, Carsten Maple, Jian Xiong, "Self-IQ-Demodulation Based Compensation Scheme of FD IQ Imbalance for Wideband Direct-Conversion Transmitters". Submitted to IEEE Transactions on Broadcasting
4. **Wei Li**, Yue Zhang, Li-ke Huang, John Cosmas, Qiang Ni," 2015 IEEE International Symposium on Broadband Multimedia Systems and Broadcasting (BMSB 2015), Jun. 2015, Ghent
5. **Wei Li**, Yue Zhang, Li-ke Huang, John Cosmas, Carsten Maple, Jian Xiong, "Self-IQ-Demodulation Based Compensation Scheme of FD IQ Imbalance for Wideband Direct-Conversion Transmitters ", 2014 IEEE International Symposium on Broadband Multimedia Systems and Broadcasting (BMSB 2014), Jun. 2014, Beijing
6. **Wei Li**, Yue Zhang, Yuan Zhang, Li-ke Huang, J. Cosmos, C. Maple, "Subspace-Based SNR Estimator for OFDM System under Different

Channel Conditions", 2013 IEEE International Symposium on Broadband Multimedia Systems and Broadcasting (BMSB 2013), Jun. 2013, London

7. **Wei Li** "Aeroflex PXI 3050 Signal Generate IQ Imbalance Calibration Test Report", Aeroflex, Stevenage, Oct. 2012

2. Physical Layer Model of LTE and Beyond Systems

2.1 Introduction

As an IP based network, LTE Radio Access Network (RAN) provides access to core networks with the functionalities of Radio Resource Control (RRC), Packet data Convergence Protocol (PDCP), Radio Link Control (RLC), Media Access Control (MAC) and Physical Layer (PHY). Fig. 2.1 demonstrates a brief LTE network topology. The upper layers process the packet data from/towards the core network and the PHY then conveys the information from the upper layers through physical channels [10, 11, 29, 56]. This dissertation will focus on the physical layer, which is responsible for the bottommost data exchange process in the network. The other functionalities of PHY, such as link adaption and power control, are out of this dissertation's scope.

The 3GPP LTE standards specify all of the PHY techniques. LTE standards first began to be examined in 2004. In 2008, 3GPP Release 8 was completed, this serving as the first specification of LTE. In this Release, techniques of OFDMA, MIMO, automatic modulation and coding (AMS) were specified. The complex data is conveyed by groups of resource blocks (RB) in an OFDMA time-frequency grid. Different physical channels are specified to carry control, synchronization, and user data [10]. The maximum bandwidth is 20 MHz. Up to 2×2 MIMO in downlink is supported in this release. In the coming Release 12, maximum bandwidth is enlarged to 40 Mhz with the help of a carrier aggregation technique and massive MIMO is adopted. Turbo code is employed to mitigate channel effects [41]. In Release 9, the concept of heterogeneous network was introduced in improve system coverage, capacity and power efficiency. This also included a coordinated multipoint technique, to enable the dynamic coordination of transmission and reception between different cells. The enhanced interference coordination (eICIC), which is based on inter-cell interference coordination (ICIC)

in Release 9, was introduced to cope with inter-cell interference. Further eICIC (FeICIC) is proposed for Release 12, to cancel the residual interference due to the densification of cells and interconnections [5].

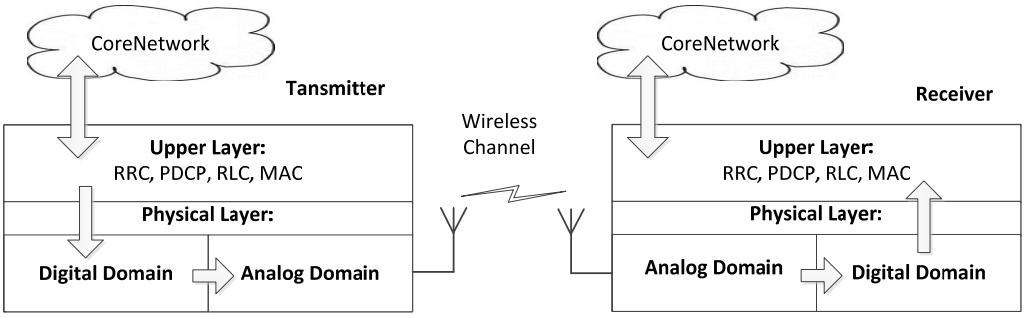

Figure 2.1 LTE Network Topology

As Fig. 2.1 shows, the LTE PHY can be divided into digital and analog domain. On the transmitter side, in order to achieve a high data rate and combat impairments, the information from the upper layer is processed by several functional modules, such as channel coding, layer mapper, OFDM [29, 56]. Then the data is presented to the analog domain in the form of a complex signal which allows for higher frequency efficiency and a lower data rate than the real signal [57],[58]. The digital complex signal will first be converted to a baseband analog complex signal. The baseband analog signal is up-converted to the desired RF band and then amplified. Finally, the transmitter antenna sends the RF signal to the receiver side via a multipath channel.

The receiver antenna then picks up the corrupted RF signal. Inside the receiver, the received weak RF signal will be amplified and down-converted to baseband. During this process, the receiver adopts direct conversion or superheterodyne technology to recover the baseband complex signal from the real RF signal. The analog signal is then digitized and transferred to the digital domain again. In the digital domain, the receiver algorithm deals with the effects of impairments from non-linearity, the fading channel, and additive white noise etc. Afterwards, the decoded signal can be recovered by reverse operations to that of the transmitter.

This decoded data is then finally sent to the upper layer for further processing [16], [59] and [60].

The remaining part of this chapter will firstly give a brief description of the direct conversion transceiver model and its impairments. Then, the multipath wireless channel model and the OFDM signal model will be introduced. Later, the LTE physical layer standard, including signal structure, key techniques and eICIC scheme, will briefly be presented for further study.

2.2 Transceiver impairments

The PHY transmitter and receiver can be implemented based on superheterodyne or direct conversion architecture [59-61]. Superheterodyne architecture realizes complex signal modulation/demodulation by using an RF stage and an Intermediate Frequency (IF) stage [57, 60, 62]. In contrast, direct conversion architecture realizes complex signal modulation/demodulation by using only one frequency on one stage. Superheterodyne architecture is less popular than direct conversion architecture due to complexity and cost reasons [57, 60]. The discussion of this dissertation will be based on direct conversion architecture.

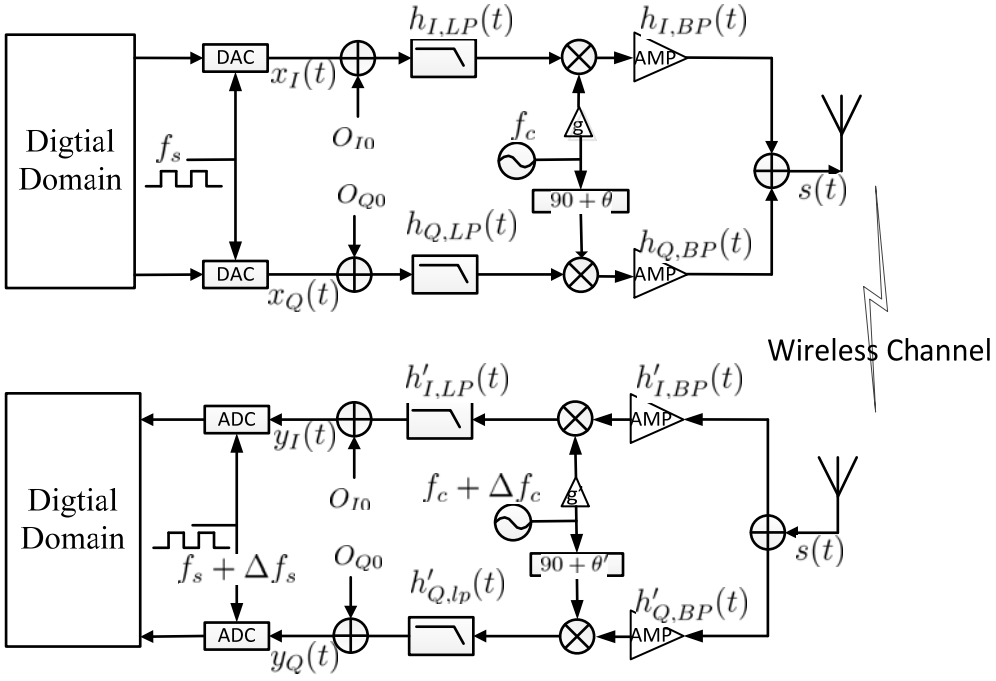

Figure 2.2 Direct Conversion Transmitter and Receiver Model

Fig. 2.2 shows the direct conversion transmitter and receiver model. On the transmitter side, the digital-to-analog converters (DACs) and lowpass filters (LPFs) reconstruct the baseband complex signal, which will be separately modulated on the inphase and quadrature branches by a pair of quadrature LOs. This quadrature modulator converts the baseband complex signal to the RF passband, then RF signals are amplified and transmitted. On the receiver side, the received RF signal will be amplified and down-converted by a pair of quadrature LOs, of which the frequency is expected to be the same with that of the transmitter LOs. This quadrature modulator converts the RF signal to two baseband signals which can be viewed as inphase and quadrature components of a complex signal. Then the baseband complex signals on each branch are digitized by ADCs, of which the sampling frequency is the same as that of transmitter. The digital baseband complex signal can then be further processed by receiver algorithms in the digital domain. In real systems, there exist some nonidealities that will corrupt the overall signal quality:

- **I/Q imbalance**

The most notorious problem of direct conversion architecture is I/Q imbalance [16-19]. This is caused by the mismatched LPF, mixer and amplifiers on inphase and quadrature branches, as shown in Fig. 2.2. A lot of literature investigates FI I/Q imbalance [13-15]. However, the mismatch will exhibit an FD property for the wideband signal, which means these models fail to describe the wideband scenario. In this dissertation, the wideband frequency response of LPFs, mixers and amplifiers will be modelled, as shown in Fig. 2.2. Furthermore, a detailed FD I/Q imbalance model is presented in Section 3.2.

- **Frequency offset**

Apart from the I/Q imbalance problem, frequency and timing error also exerts a significant impact regarding signal quality. As shown in Fig. 2.2, the quadrature modulation and demodulation operates with different frequency sources. In addition, the sampling clocks of ADC and DAC on the transmitter and receiver sides also operate in accordance with different clock sources. This causes a frequency offset between transmitter and receiver. For LTE systems, the demodulation of OFDM signal in the presence of frequency and timing error destroys the orthogonality of subcarriers. The frequency error is briefly modelled in Fig. 2.2. Furthermore, Section 4.2 depicts in detail the impact of the frequency offset.

This dissertation will investigate the effect impairments of transmitter I/Q imbalance and frequency offset. The other impairments, including receiver I/Q imbalance and non-linearity distortion, will be modelled as Additive White Gaussian Noise (AWGN) noise. Furthermore, the baseband equivalent models for frequency response of transmitter analog devices and frequency offset will be considered, which makes it straightforward to simulate the whole system. Based on this baseband equivalent model, a lost baseband compensation technique can be realized.

2.3 Wireless channel model

2.3.1 Wireless channel environment

The radio signals are also degrade by the wireless channel. As depicted in Fig. 2.3, the transmitted radio wave, which will be reflected, attenuated by various obstacles, travels along a different path before arriving at the receiver antenna. As a result, the receiver antenna picks the radio signals which consist of different duplicates of the original signal with different time delays and amplitudes. This combination of different delayed original signals leads to *constructive* or *destructive* results, known as the 'multipath effect'. Aside from the multipath effect, the relative dynamic movement of transmitters, obstacles and receivers causes a time varying effect, which is referred to as 'fading'.

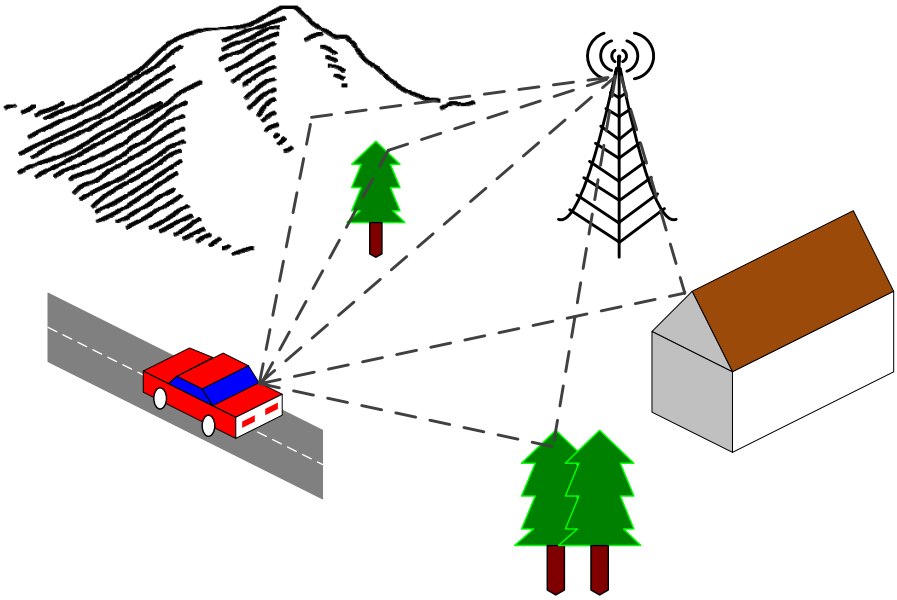

Figure 2.3 Propagation of Radio Signal in Wireless Channel

The channel impulse response (CIR) $h(\tau, t)$ at time t and propagation delay τ can be modelled as [63, 64]:

$$h(\tau,t) = \sum_{k-1}^{K(t)} \alpha_k(t) e^{-j2\pi f_c \tau_k(t)} \delta(\tau - \tau_k(t)) \tag{2.1}$$

where $\alpha_k(t)$ is the attenuation factor for the signal receiver on the k^{th} path; $\tau_k(t)$ is the delay of k^{th} path and $K(t)$ is the number of path at t. Assuming there are a

great many paths, the channel impulse response $h(\tau, t)$ can be modelled as a complex valued Gaussian process according to the central limit theorem. For a channel that has no fixed reflectors or scatters, the Gaussian process is zero-mean and has a Rayleigh probability density function (PDF):

$$f_{|h|}(\tau, t) = \frac{\sqrt{\tau^2 + t^2}}{\sigma^2} e^{-\frac{\tau^2+t^2}{2\sigma^2}} \tag{2.2}$$

where $|h|$ is the envelope of $h(\tau, t)$ in Eq. (2.1), and σ is a constant. Another PDF can be used to model the envelope of the channel with respect to delay τ and t based on the channel scattering and reflection condition, such as Ricean and Nakagami-m distribution. The channel model in Eq. (2.1) will be used for simulation

2.4 OFDM signal model

LTE downlink transmission adopts OFDM modulation. As a special case of Frequency Division Multiplexing (FDM), OFDM modulates bit streams on several subcarriers in parallel. In FDM systems, the data bits are modulated by different subcarriers and these subcarriers are separated by a guard band in the frequency domain to prevent the overlap between different subcarriers, as shown in Fig. 2.4. The extra guard band reduces the spectral efficiency. By contrast, an OFDM system utilizes the overlapped subcarriers which are orthogonal to each other. Because of orthogonality, the subcarriers of interest locate on the nulls of the other subcarriers without introducing any interference to the subcarriers of interest, as shown in Fig. 2.5. The OFDM system avoids using the guard band in this way and achieves higher spectral efficiency. Another benefit is that the bit rate could be reduced as data streams can be transmitted on different subcarriers in parallel. As a result, the symbol duration is increased. And the system is more robust to the frequency-selective channel if it has longer symbol duration than the *maximum delay spread* T_m.

The FMD signal can be expressed in the linear form:

$$x(t) = \sum_{k=0}^{N} X_k \mathbf{\Phi}_k(t) \tag{2.3}$$

where X_k is the coefficient of k^{th} subcarrier; K is the number of subcarriers and $\mathbf{\Phi}_k(t)$ is expression of subcarrier in time domain:

$$\mathbf{\Phi}_k(t) = w(t)e^{j\pi f_k t} \tag{2.4}$$

where $w(t)$ is the time window for the symbol of interest. For the sake of simplicity, the rectangular window with length of T is used:

$$w(t) = \frac{1}{\sqrt{T}}\text{rect}(Tt) \tag{2.5}$$

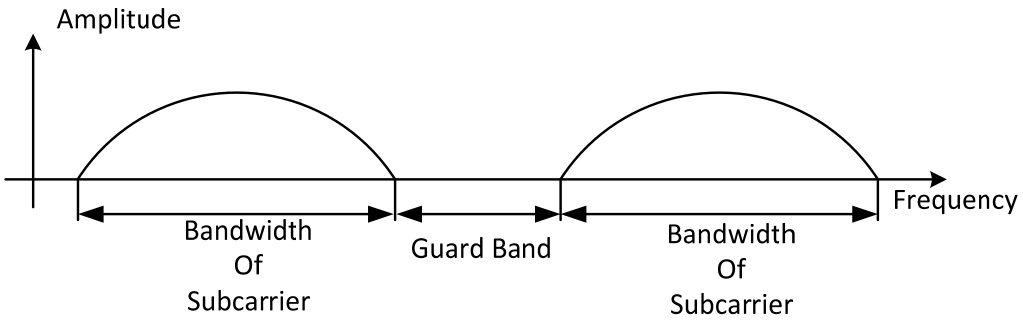

Figure 2.4 Subcarriers in FDM Systems

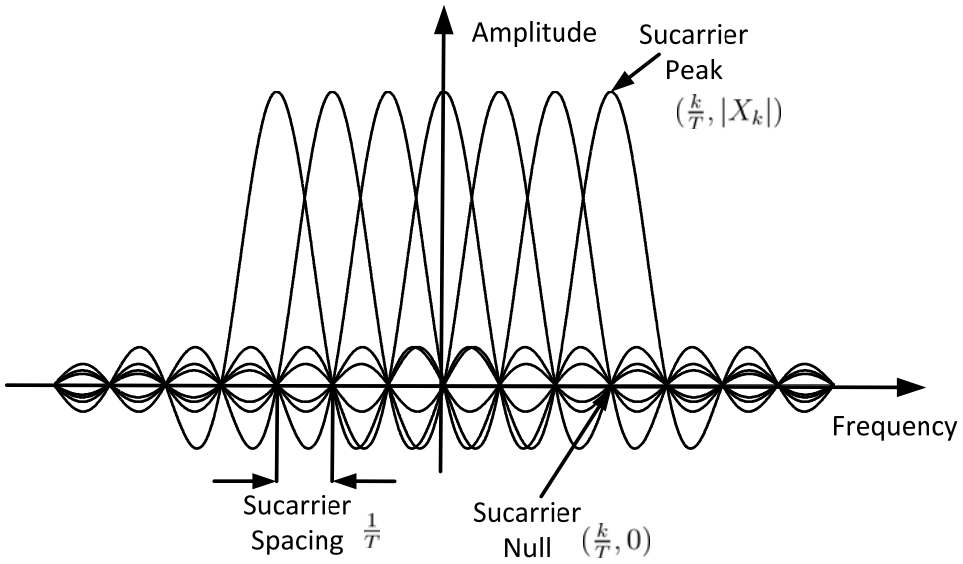

Figure 2.5 Subcarriers in OFDM Systems

The window length T can also be viewed as the symbol period. In OFDM, the subcarriers are orthogonal to each other, hence the subcarriers satisfy the following relationship:

$$\int_{-\infty}^{\infty} \mathbf{\Phi}_l(t)\mathbf{\Phi}_m^*(t) = \begin{cases} 1 & \text{for } l = m \\ 0 & \text{for } l \neq m \end{cases} \tag{2.6}$$

Substitute Eq. (2.4) for the $\mathbf{\Phi}(t)$ in Eq. (2.6), there is:

$$\begin{aligned} \int_{-\infty}^{\infty} \mathbf{\Phi}_l(t)\mathbf{\Phi}_m^*(t) &= \frac{1}{T}\int_{-T}^{T} e^{j2\pi(f_l - f_m)t} \\ &= \frac{\sin(\pi(f_l - f_m)T)}{\pi(f_l - f_m)T} \\ &= \begin{cases} 1 & \text{for } l = m \\ 0 & \text{for } l \neq m \end{cases} \end{aligned} \tag{2.7}$$

In solving this equation, we have $f_l - f_m = n/T$. This shows that, in order to meet the requirement for orthogonality, the subcarrier spacing should be a multiple of $1/T$. This can be verified with the Fourier transform of Eq. (2.3):

$$\begin{aligned} X(f) &= \sqrt{T}\sum_{k=0}^{K} X_k \frac{\sin(\pi T(f-f_k))}{\pi T(f-f_k)} \\ &= \sqrt{T}\sum_{k=0}^{K} X_k \mathrm{sinc}(T(f-f_k)) \end{aligned} \tag{2.8}$$

According to Eq. (2.8), the OFDM signal can be viewed as the summation of several *sinc* functions with a frequency shift of k/T as shown in Fig. 2.5. As the nulls of *sinc* function locate on k/T, the overlapping of a different subcarrier does not bring interference to the frequency points k/T. The orthogonality between different subcarriers is achieved in this way. However, this is vulnerable to frequency offset. If the orthogonality is broken by the carrier frequency offset or Doppler effect, the side lopes for the other subcarrier will accumulate at the interested frequency point, which causes inter-carrier interference (ICI).

Due to the stringent requirement for subcarrier orthogonality, it is difficult to generate the OFDM signal using analog devices. Instead, the digital signal process (DSP) technique makes it possible to generate an OFDM signal by Inverse Fast Fourier Transform (IFFT). If the subcarrier of OFDM signal with frequency k/T and $x(t)$ in Eq. (2.3) is processed in the digital domain with the sampling frequency $f_s = K/T$, then Eq. (2.3) in the digital domain can be rewritten as:

$$\begin{aligned} x(n\Delta T) &= \sum_{k=0}^{N} X_k w(nT_s) e^{j\pi f_k n T_s} \\ &= w(nT_s) \sum_{k=-N/2}^{N/2-1} X_k e^{j\frac{\pi}{N}nk} \\ &= w(nT_s) \cdot \mathrm{IFFT}\left\{X_k\right\} \end{aligned} \tag{2.9}$$

where $T_s = 1/f_s$. It shows that the time domain OFDM can be easily obtained by applying IFFT to the frequency domain data. Thus, the generation of an OFDM symbol can be summarized as:

In order to achieve orthogonality, the subcarrier spacing is set to multiple of symbol rate $1/T$. Then, the data in the frequency domain is assigned to every subcarrier's frequency for modulation. Afterwards, the time domain OFDM signal is generated by applying IFFT to the corresponding frequency domain data. With the development of DSP, the implementation of IFFT operation becomes cheap and fast – Dedicated IFFT core is embedded in the chip and it only takes several clock periods to complete the IFFT operation.

Thesymbol length will be extended by *maximum delay spread* T_m when passing through the frequency selective channel, which causes ISI between adjacent symbols. Inserting a guard interval (GI) between the symbols can prevent ISI. Furthermore, OFDM avoids this problem by inserting a Cyclic Prefix (CP) in the GI. As shown in Fig. 2.10, the content of CP is the copy of last OFDM symbols with length longer than T_m. When transmitting in the frequency selective channel, the interference from the previous symbols is limited within the CP. At the receiver side, the CP part will be removed. In this way, the remaining uncontaminated part can still retain more than one cycle of subcarriers as shown in Fig. 2.6, which guarantees orthogonality among subcarriers.

After the insertion of CP, the time window $w(nT_s)$ expands to $T_o = T + T_g$ where T_g is the length of CP and T the symbol length without CP. Hence the l^{th} transmitted OFDM symbol in a successive transmission is expressed as:

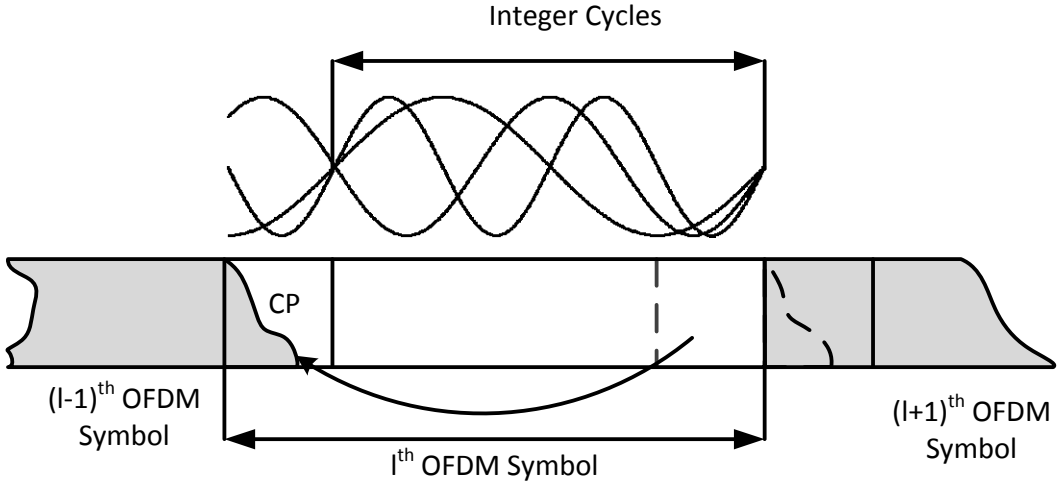

Figure 2.6 Cyclic Prefix in OFDM

$$x(t) = \frac{1}{\sqrt{T}} \sum_{l=-\infty}^{+\infty} \sum_{k=-N/2}^{N/2-1} X_{k,l} e^{j\frac{\pi}{N}(t-lT_o-T_g)} w(t-(l-1/2)T_o) \quad (2.10)$$

where $w(t)$ is the window function specified in Eq. (2.5).

Using the channel model in Section 2.3, the received signal can be represented as:

$$y(t) = h(\tau(t), t) * x(t) + n(t) \quad (2.11)$$

where $n(t)$ is the additive noise. In the frequency domain, this can be expressed as: $Y(f) = H(f) \cdot X(f) + N(f)$. Intuitively, it is easy to recover the transmitted OFDM signal $X(f)$ with $Y(f)/H(f)$. The receiver utilizes the OFDM signal structure and recovers $X(f)$ as follows:

After the received signal is sampled by the receiver ADC, the CP is removed and FFT is carried out to get the received signal $Y(n)$. Then the transmitted signal is obtained by doing *equalization* $Y(n)/\hat{H}(n)$, where $\hat{H}(n)$ is the estimation of channel frequency response. This method is effective because of the special design of the OFDM signal structure. Firstly, the influence of the previous symbol is restricted, which means that the remaining part is immune to the ISI from the previous symbol. Hence, $Y(f)$ is only contaminated by the frequency-selective fading channel and the additive noise. Secondly, the content in CP, is the copy of the last few pieces of data in the OFDM symbol, which makes it equivalent to circular convolution, whereas the effect of the channel is a linear convolution process. In other words, the circular convolution which corresponds to $Y(n)/\hat{H}(n)$ equals the linear convolution in operation $Y(f)/H(f)$, thus the signal can be recovered. More specifically, the CP can be regarded as the periodic extension of the OFDM symbol with a period of N. As maximum delay spread T_m is shorter than the CP length T_g, the linear convolution of CP is repeated at the last part of the OFDM symbol. As a result, the linear convolution in the channel contamination process becomes circular convolution and the transmitted signal

can be recovered. This equalization method provides a very simple way to recover the transmitted signal compared with the inverse convolution method.

Though OFDM brings these benefits, it is vulnerable to frequency offset. As the orthogonality is based on accurate superposition of subcarrier, any frequency offset will result in side lobes of the other subcarriers overlapping the interested subcarrier, which introduces ICI. This frequency offset could be caused by CFO, SFO or even Doppler frequency shift. Hence, the frequency offset estimation and compensation is important and will be discussed in the following chapters.

2.5 LTE PHY standards and eICIC

Throughout this dissertation, the enhancement technique is developed for LTE systems. However, the proposed algorithms are also suitable for other OFDM systems which operate in similar environments and platforms. LTE adopts several new techniques to improve data rate and signal qualities. This dissertation studies algorithms related to the following techniques:

- **OFDMA**

Orthogonal Frequency-Division Multiple Access (OFDMA) is adopted in LTE downlink, and Single-Carrier Frequency-Division Multiple Access (SC-FDMA) is used in uplink because of lower peak-to-average ratio (PAR). This dissertation will focus on the downlink transmission. For a more in depth study of the uplink transmission, the reader is referred to [56, 65]. OFDMA is an access scheme that is based on the OFDM principle to arrange the distribution of radio resources for multi users. In OFDMA, the radio resources can be allocated flexibly to a specific user at different time instances. Fig. 2.7 gives a brief illustration of OFMD and OFDMA principles. The OFDM symbols which carry data for different users are mapped to radio resources. The radio resources (subcarrier) distributes on the appropriate frequency and time grids. Unlike the pure OFDM technique, the radio resources in such an OFDM symbol can be allocated to different users according

to the channel conditions. This flexible access scheme improves the spectral efficient as the scheduler allocates the radio resources to the users in an optimized way. As a special access scheme of OFDM, OFDMA demonstrates the advantages of robustness against frequency-selective channels.

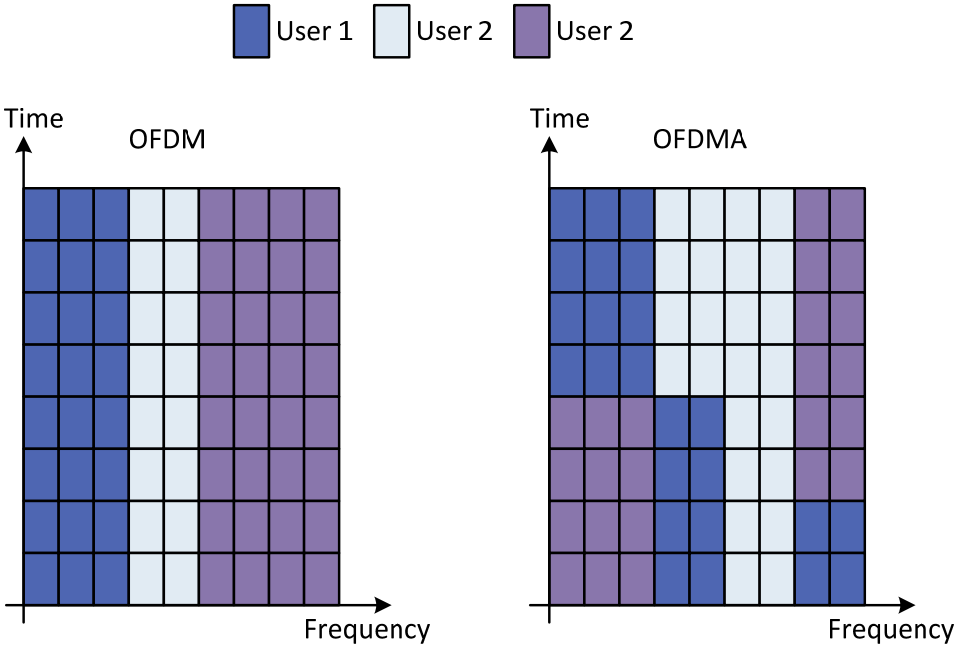

Figure 2.7 Brief Illustration of OFDM and OFDMA

- **Multiple-Input and Multiple-output (MIMO) Antenna**

LTE adopts the MIMO technique to improve the data rate and spectral efficiency. The eNodeB supports up to 4 transmit antenna ports and 4 receive antenna ports. Up to 2 receive antenna ports and 1 transmit antenna port can work simultaneously in UE. Fig. 2.8 shows three main MIMO techniques that can improve the signal quality and channel capacity:

1). **Beamforming**. This technique concentrates the radio beam to a specific spatial direction which improves power efficiency and reduces interference. This is achieved by the beam destructive and constructive interference of the precoded antennas.

2). **Spatial diversity**. In spatial diversity, the signals passing through different channels between antenna sets combine to compensate the frequency-selective channel. Several combining algorithms have been investigated for both transmit and receive antennas, such as Space-Time Block Coding, Maximal-Ratio Combining. Compared with a signal antenna system, this approach provides better signal quality and reliability.

3). **Spatial multiplexing**: For spatial multiplexing, the channels between different antennas are utilized to transmit separate and independent encoded data. The channel is reused to improve the channel capacity.

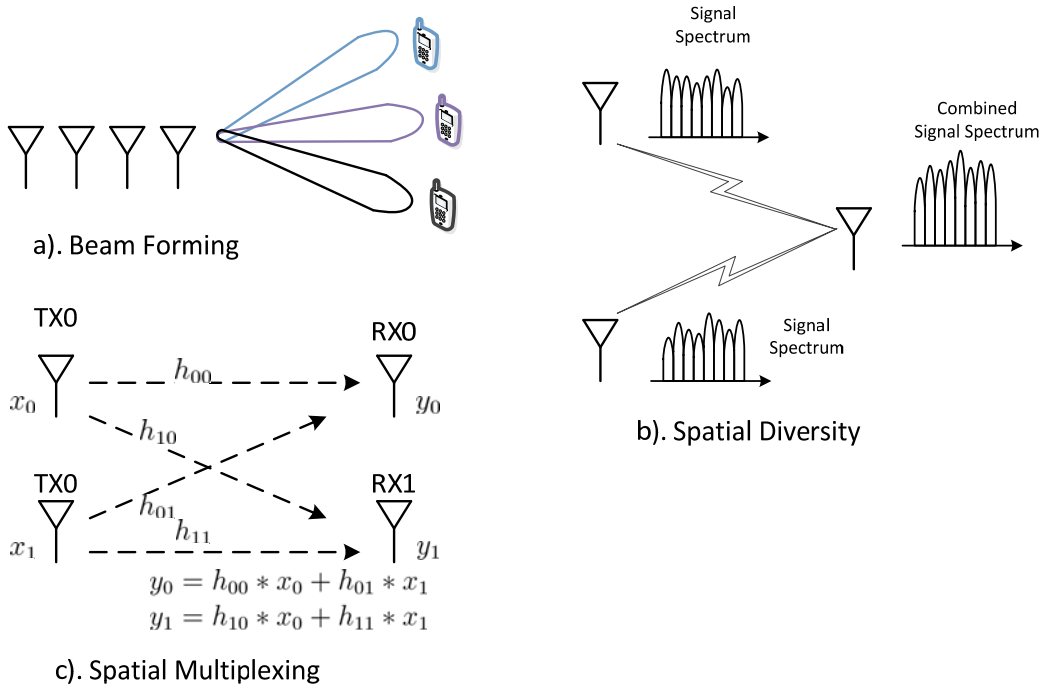

Figure 2.8 Three MIMO Techniques in LTE

These three MIMO techniques improve performance in terms of power efficiency, interference, signal quality, and channel capacity. Hence, the LTE link adaption scheme provides a precoding matrix for spatial diversity and multiplexing, which allows switching between different antenna techniques according to the Precoding Matrix Indicator (PMI) and Rank Indicator (RI) submitted by the user.

- **Adaptive Modulation and Coding Scheme (AMC)**

The radio signal for a specific user will experience different Signal-to-Interference plus Noise Ratio (SINR) in the time-variant channel. The 3GPP proposes several channel coding features to ensure signal quality and data rate in different channels. In order to achieve this goal, the channel coding rate and modulation scheme is adjusting adaptively based on channel conditions:

1). **Channel coding rate** determines how fast the data rate is by adding adjustable amount of redundancy in the Forward Error Correction (FEC) process. By adding, more redundancy, better signal robustness can be achieved with lower throughput.

2). **Modulation scheme**: LTE supports three modulation schemes: QPSK, 16QAM and 64QAM. They assemble 2, 4 and 6 bits for one modulated symbol respectively. QPSK provides the best performance in terms of robustness and 64QAM yields the highest data rate. The eNodeB adaptively changes the MCS for a user according to the Channel Quality Indicator (CQI) reported by the corresponding user equipment. The CQI ranges from 0 to 15 which specifies the transmission rate from 0.15 bits/resource elements to 5.55 bits/resource element [66, 67].

2.5.1 LTE downlink PHY data processing

After being processed by the PDCP, RLC and MAC layer, the user data sends signalling messages which are presented to PHY for transmission in the form of transport block (TB). Fig. 2.9 shows the data processing in the LTE PHY downlink. The TBs are firstly appended with a 24 bit checksum (CRC) and processed with turbo coder for Forward Error Correction (FEC). Then the coded data is added with a certain amount of redundancy according to the reported CQI. This step transfers the resulting code blocks to codewords. The codewords are scrambled by a sequence based on the user information and cell physical ID. The scrambled bit sequence is then converted into modulated data (QPSK, 16QAM or 64QAM) based on the reported CQI. After channel coding, the modulated data is processed by the layer mapper and precoder for multi-antennas transmission. Then the precoded data is mapped to the OFDMA resource elements.

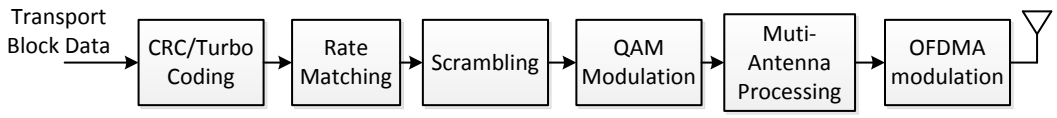

Figure 2.9 LTE Downlink PHY Data Processing

2.5.2 LTE downlink frame structure and radio resource

- **Frame structure**

The LTE downlink transmission is organized into radio frame, subframe, slot and symbol in time domain. The basic time unit for transmission is defined as $T_s = 1/(15000 \cdot 2048) = 32.55ns$. One radio frame has 10 ms duration. Each frame is divided into 10 subframes with equal length. [56] specifies two types of frame structures: Type 1 for Frequency-Division Duplexing (FDD) and Type 2 for Time-Division Duplexing (TDD). This dissertation focuses on FDD, and the readers are referred to [56] for detailed TDD specification. Fig. 2.10 illustrates the structure for Type 1 frames. For FDD, each subframe consists of 2 slots of equal size, where the duration is 0.5 ms. The 20 slots in one ratio frame are numbered from 0 to 19. The 1 ms duration of subframe is defined as an LTE Transmission Time Interval (TTI).

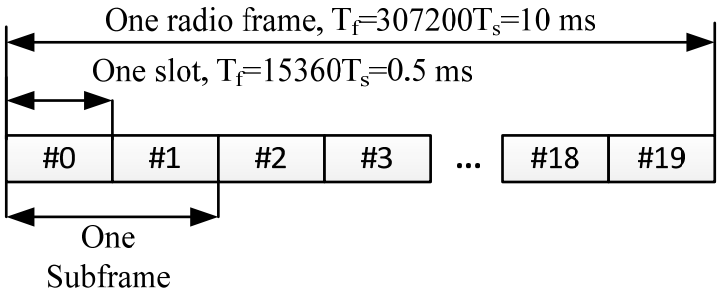

Figure 2.10 Structure for Type 1 Frames

- **Radio resources**

The radio resource of LTE is divided into several frequency-time grids. The smallest frequency-time unit in downlink and uplink is called a Resource Element (RE). An RE on a specific antenna port is specified as one subcarrier over one OFDM symbol. Hence, one RE corresponds to one modulated complex data. The mapping of LTE physical channels to resource elements is described by resource blocks (RBs). A physical resource block consists of 12 consecutive subcarriers in a frequency domain over one slot (0.5 ms) in time domain. The subcarrier spacing is specified as 15 or 7.5 KHz. Thus one RB occupies $180\,KHz \times 0.5\,ms$ radio resource in frequency and time domain respectively. The LTE provides 6 different transmission bandwidths by enabling a different amount of RB, which ranges from 6 to 100 RBs and corresponds to a bandwidth of 1.4 MHz to 20 MHz. All the available subcarriers in the full bandwidth over one slot consist of one resource grid. Fig. 2.11 shows the general structure of RB and the resource grid. The total number of RB within the available downlink bandwidth is denoted by N_{RB}^{DL}; the number of subcarriers and symbols in one resource block is denoted by N_{sc}^{RB} and N_{symb}^{DL} respectively.

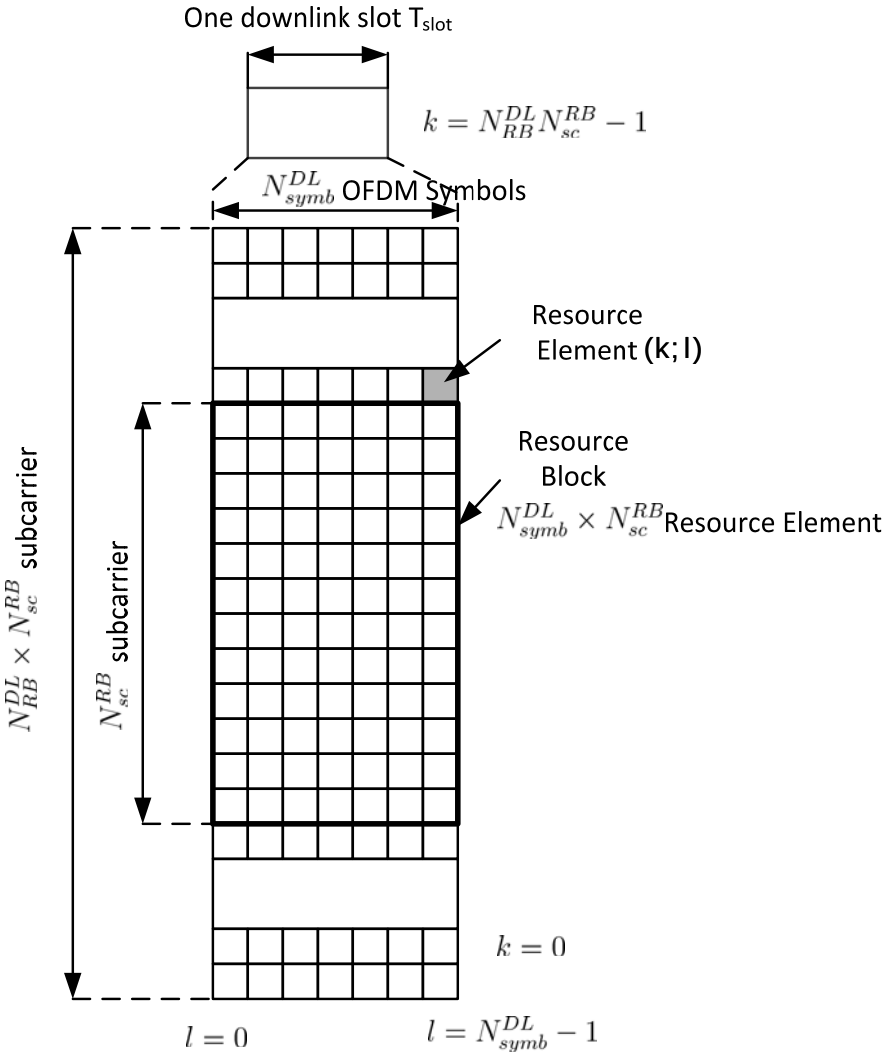

Figure 2.11 Structure of Resource Grid and Resource Block

2.5.3 Key LTE downlink physical signals

In downlink, several physical channels are defined to carry information blocks from upper layers. And the reference signals are generated and allocated to specific REs according to the cell configurations:

- **Physical Broadcast Channel** (PBCH) broadcasts essential information about the cell such as downlink bandwidth and system frame number. The PBCH is assigned to the 72 subcarriers in the centre of the full bandwidth of the second slot.

- **Primary and Secondary Synchronization Signal (PSS and SSS) are** located in the first subframe of the radio frame. These two signals enable the users to be synchronized on a subframe level and to obtain cell information.

- **Physical Downlink Shared Channel** (PDSCH) carries the user data which is dynamically assigned to the REs Multimedia Broadcast and Multicast Services.

- **Reference signal** is used for time-frequency synchronization and channel estimation. LTE defines three types of reference signal: cell specific, UE specific and broadcast specific RS. This dissertation focuses on the cell specific reference signal. The reference signal is generated from the Gold sequence based on the cell ID.

This dissertation investigates algorithms based on the above channels and reference signal. For other control and transport channels readers are referred to [56].

2.5.4 LTE eICIC scheme

In order to improve the spectral efficiency per unit area, LTE proposes Heterogeneous Networks (HetNet) topologies which consist of macro cells and smaller pico/femto cells as shown in Fig. 2.12. The macro cell provides wide area coverage and serves a larger amount of UEs. The pico/femto cells fulfil the network needs, and improve spectral efficiency and capacity. However, this multi-layer topology also encounters an interference problem. As Fig. 2.12 shows, the UEs will adhere to a pico/femto cell if it is within the coverage of these cells. However, these UEs can still receive a signal from macro cell when it is within the coverage of macro cell. The signal from macro cell causes interference to pico/femto-UEs. To mitigate this inter-cell interference, LTE Release 10 [67] proposes a time domain enhanced inter-cell interference cancellation (eICIC) scheme using almost blank subframes (ABS). During ABS, the macro cell is

scheduled to switch off PDSCH and only transmits essential signals such as CRS, PSS and SSS. Fig 2.17 shows a basic principle of ABS frame. The ABS frames, as shown in the while region of Fig. 2.13, do not carry PDSCH signal. This implies that the pico/femto-UEs will not be dominated by interference from macro cells. However, the remaining signals in the ABS still cause interference [54]. Further eICIC (FeICIC) will be proposed in the coming Release 12. Hence, this dissertation investigates algorithms that can suppress residual CRS interference for FeICIC.

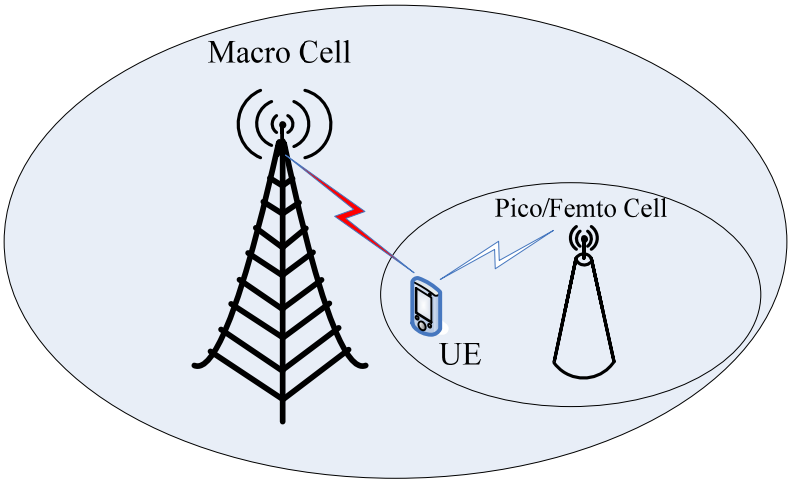

Figure 2.12 Heterogeneous Network

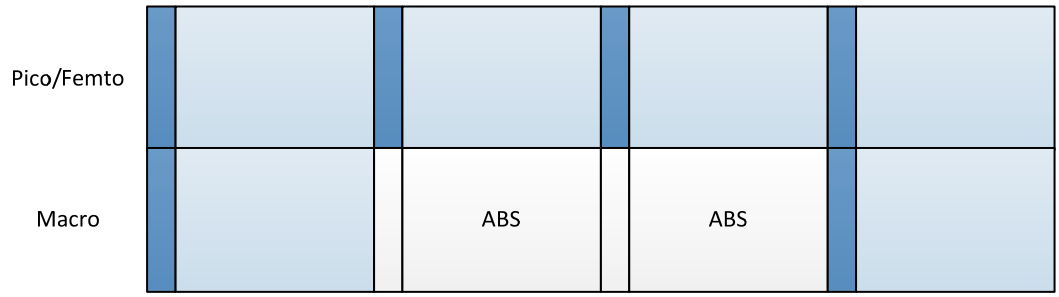

Figure 2.13 Basic Principle of ABS

3. Self-IQ-demodulation based FD I/Q Imbalance Compensation

A low cost FD (FD) I/Q imbalance self-compensation scheme is investigated in this chapter. Direct conversion transmitters are widely used in wireless systems. However, unwanted image-frequencies and distortions are inevitably introduced into direct conversion systems. This problem is even more severe in wideband systems. Therefore, accurate estimation and compensation of I/Q imbalance is crucial. The current compensation method is based on external instruments or an internal feedback path which introduces additional impairments and is expensive. This chapter proposes a low cost FD I/Q imbalance self-IQ-demodulation based compensation scheme without using external calibration instruments. First, the impairments of baseband and RF components are investigated. Further to this, an I/Q imbalance model is developed. Then, the proposed two-step self-IQ-demodulation based compensation scheme is investigated. In the first step of the scheme, the local oscillator (LO) related I/Q impairment parameters are estimated. Then in the second step, the overall FD I/Q imbalance parameters are estimated by utilizing the transmitter LO. To realize this self-IQ-demodulation algorithm, minor modifications are introduced to the current power detector circuit. Afterwards, the estimated parameters are applied to the baseband equivalent compensator. This sophisticated algorithm guarantees low computation complexity and low cost. The compensation performance is evaluated using laboratory measurement.

3.1 Introduction

Direct-conversion transmitters (DCT) are widely adopted in digital broadcasting systems such as digital audio broadcasting (DAB), digital video broadcasting (DVB), and digital terrestrial multimedia broadcasting (DTMB) because of the

advantages of low-cost, simplicity and flexibility. The ideal digital complex signal is represented by inphase and quadrature signal in the I and Q branch respectively. The baseband I and Q signal is then modulated by a quadrature modulator which makes DCT easy to implement. However, some practical problems arise from the implementation of direct-conversion transmitters. These problems are mainly caused by the non-idealities of the baseband and RF components, such as I/Q imbalance, clock jitter, power amplifier (PA) distortion and inter-modulation. The overall impact results in image-frequency interference, phase noise and high order frequency interference, which severely degrades the transmitter performance especially for wideband multicarrier systems. Generally, the main impact of I/Q imbalance is image-frequency interference and degradation of PA nonlinearity [18, 68-70]. In OFDM systems such as DVB, the image frequency component overlaps the desired signal on corresponding subcarriers, which decreases the SNR of the desired signal. Hence, image rejection ratio (IRR) is a critical criterion for DCT.

There are several works covered in the literature. The work in [71] addresses the combined effects of transmitter and receiver I/Q imbalance, whereas, the work in [18, 26, 72] focuses on transmitter I/Q imbalance and adopts a low intermediate frequency (IF) down-conversion structure, in which the corrupted signal is down-converted to a low IF and sample with an analog-to-digital converter (ADC), which requires a high speed ADC. I/Q demodulation and parameters estimation are computed by DSP. The advantage of this estimation structure is that I/Q demodulation is performed in the digital domain, which avoids the receiver I/Q imbalance. [22, 24, 29] also investigates the low-cost diode-based I/Q imbalance estimation technique, which makes use of the power detector of transmitters and realizes self-calibration. However, the estimation is confined to FD I/Q imbalance due to the bandwidth limit of the power detector. [18, 26, 72] studies FD I/Q imbalance, which is more realistic for wideband systems such as DVB and LTE. [18] proposes a second-order statistics-based approach and a widely linear least-squares (WL-LS) approach. These do not take LO leakage into account. [26] estimates I/Q imbalance parameters by cross-processing between I and Q signals.

[72] proposes a specially designed pilot sequence, which estimates I/Q imbalance and channel response jointly. Recently, [73] proposed a diode based IQ imbalance and nonlinearity method. A joint model of IQ imbalance and nonlinear is analytically derived. Special test signals are devised to isolate the effects of gain and phase imbalance, dc offsets. Based on this isolation, the imbalance and nonlinearity are calculated easily with a few mathematical operations. However, this method is only applied to frequency-independent scenarios.

In this dissertation, a self-IQ-demodulation based compensation scheme of FD I/Q imbalance is studied and presented, as shown in Fig. 3.1. In particular, the “time division” method and its corresponding circuit are implemented to realize self-IQ-demodulation. This compensation scheme consists of estimation and compensation stages. The estimation stage adopts a two-step self-IQ-demodulation algorithm. In the first step, the amplitude LO impairments, including DC offset, are estimated using the power detector. Two tone training signal is transmitted to measure these impairments. This special training signal is designed with low computation complexity. In the second step, the self-I/Q-demodulation is implemented to estimate the FD I/Q imbalance parameters. As the external I/Q demodulator has been omitted in this scheme, the transmitter LO is transmitted with the test signal using the “time division” method for self-I/Q-demodulation. The LO related impairments parameters, which are estimated in Step 1 are then used to compensate the self-I/Q-demodulation error caused by the inherent transmitter LO imbalance. Afterwards, the FD I/Q imbalance can be estimated. Furthermore, the estimation results are applied to the compensation stage. The circuit components in [22, 24, 29] are extended to wideband in this proposal to meet the requirement of self-I/Q-demodulation.

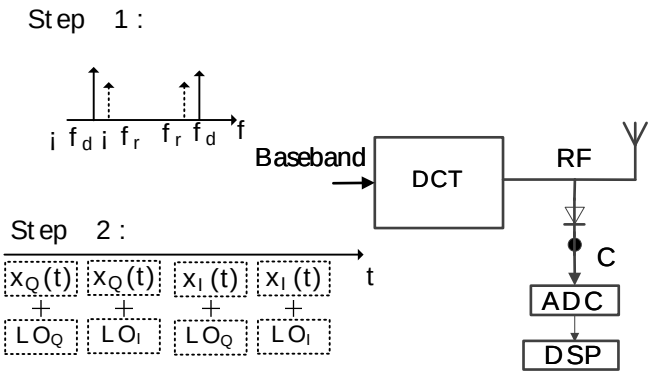

Figure 3.1Proposed Compensation Scheme

3.2 I/Q Imbalance model

LTE adopts complex signal to carry the user and control data. The complex signal can be presented with a single sideband spectrum in the frequency domain. This means the complex signal occupies only a single sideband in the range of [0, B] Hz or [-B, 0] where B is a value that specifies the signal bandwidth. In contrast, the real signal occupies a double sideband in [-B, B] Hz. Hence, a complex signal improves spectrum efficiency. However, the analog signal in the real word is real form. There are many methods to represent a complex signal using a real signal, such as Hilbert Transform, quadrature modulation and Polyphase filtering. This dissertation focuses on quadrature modulation.

3.2.1 Ideal quadrature modulation

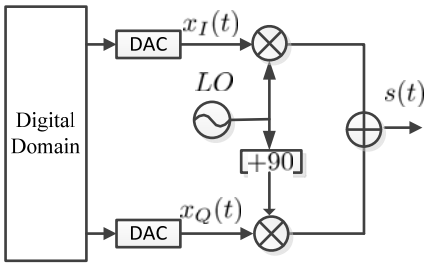

Figure 3.2 Ideal DCT Topology

Quadrature modulation, or direct conversion, is a technique used to construct a complex signal by mixing baseband signals with quadrature carriers as shown in Fig. 3.2. Consider a baseband complex signal $x(t)$:

$$x(t) = x_I(t) + j \cdot x_Q(t) \tag{3.1}$$

with inphase and quadrature components $x_I(t)$ and $x_Q(t)$ respectively. The corresponding spectrum is $X(f)$. In order to be transmitted, the signal needs to be transferred to RF passband:

$$X'_{rf}(f) = X(f - f_c) = X(f) \otimes \delta(f_c) \tag{3.2}$$

where $\delta(f)$ is Dirac's delta function. In the time domain, it can be expressed as:

$$\begin{aligned} x'_{rf}(t) &= x(t)e^{j2\pi f_c t} \\ &= x(t) \cdot (\cos(2\pi f_c t) + j \sin(2\pi f_c t)) \end{aligned} \tag{3.3}$$

where $x_c(t) = e^{2\pi f_c t}$ can be regarded as the modulating signal. However, only the real signal can be transmitted in the practical circuit [74]:

$$\begin{aligned} x_{rf}(t) &= \Re\left\{x'_{rf}(t)\right\} \\ &= \Re\left\{x(t)e^{j2\pi f_c t}\right\} \\ &= x_I(t) \cdot \cos(2\pi f_c t) - x_Q(t) \cdot \sin(2\pi f_c t) \end{aligned} \tag{3.4}$$

This equation reveals the principle of the direct conversion transmitter, as shown in Fig. 3.2. The analog inphase signal $x_I(t)$ and quadrature signal $x_Q(t)$ is reconstructed by DACs and LPFs. These two baseband analog signals are modulated by a pair of quadrature LOs. Then the RF signal is sent to the receiver via the wireless channel.

Further to this, Eq. (3.4) can be expanded as:

$$\begin{aligned} x_{rf}(t) &= x_I(t) \cdot \cos(2\pi f_c t) - x_Q(t) \cdot \sin(2\pi f_c t) \\ &= \frac{1}{4}\left(\left(x(t) + x^*(t)\right)\left(e^{j2\pi f_c t} + e^{-2\pi f_c t}+\right) + \right. \\ &\quad \left. \left(x(t) - x^*(t)\right)\left(e^{j2\pi f_c t} - je^{-2\pi f_c t}+\right) \right) \\ &= \frac{1}{2}\left(x(t)e^{j2\pi f_c t} + x^*(t)e^{-j2\pi f_c t}\right) \end{aligned} \tag{3.5}$$

where $x^*(t)$ is the conjugation of $x(t)$. In the frequency domain, it can be expressed as:

$$X_{rf}(f) = X(f - f_c) + X^*(-f - f_c) \tag{3.6}$$

As the above equation shows, the modulated signal can be regarded as the frequency shifting results of two signals: the shifting results at f_c of original signal $X(f)$forms the components in the upper band; the shifting results at $-f_c$ of image signal $X^*(-f)$ forms the components in the lower band. Hence, the original signal and its image are located at different frequency bands and there is no overlap between these two components in an ideal DCT, as shown in Fig. 3.3.

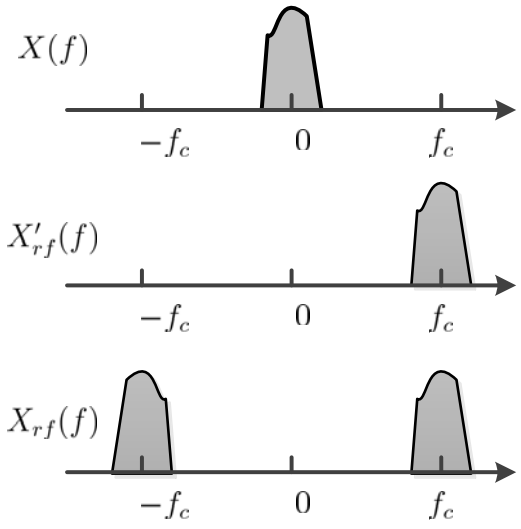

Figure 3.3 Ideal DCT Spectrum Transfer

3.2.2 Quadrature modulation with IQ imbalance

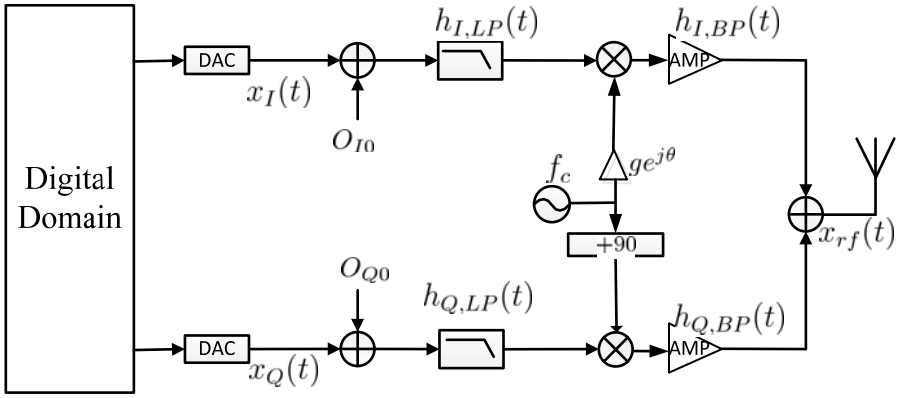

Figure 3.4 Practical DCT Architecture with I/Q Imbalance Imperfections

The ideal quadrature modulation provides infinite image suppression. However, this ideal separation of original signal and its image will be destroyed due to the mismatches between the inphase and quadrature branch in a real circuit. The image components overlap the desired components, which degrades the signal quality. Therefore, DCT requires good image rejection performance. For many systems, the I/Q imbalance is regarded as FI, which means that all the frequency components on one branch experience the same gain and phase response compared with the other branch [13, 15, 22, 75, 76]. This model is based on the assumption that the mismatch is only caused by the difference between two local oscillator signals. However, it has been observed that I/Q imbalance exhibits an FD property. In [25, 75, 77, 78], I/Q imbalance caused by the imbalance of LPFs in the basedband stage is compensated.

For wideband DCT, I/Q imbalance could arise from the ADCs, LPF, mixers, RF bandpass filters and RF amplifiers. In addition, the difference of signal path will also contribute to I/Q imbalance [79]. This section will model baseband equivalent I/Q imbalance, which takes into account the above impairments. Furthermore, these impairments will be treated separately and the corresponding FD I/Q imbalance estimation algorithm will be studied.

Fig. 3.4 illustrates the practical DCT architecture. For the sake of simplicity, the non-linear effects, including DAC distortion [80], and amplifier intermodulation, are omitted from this dissertation. Regarding the baseband in this architecture, the

digital signals of inphase and quadrature branches are converted to analog signal by DACs. In order to limit the signal bandwidth and prevent aliasing, the signals pass through a pair of reconstruction filters, which have low pass properties. At this initial data conversion stage, the signal could be influenced by the following impairments:

1). Amplitude and phase mismatch between two DACs. Due to the voltage reference difference and clock delay, the output of each DAC is not strictly matched.

2). Amplitude and phase mismatch between reconstruction filters.

3). DC offset. Due to the voltage reference drift, the output signal contains DC offset components. Assuming that the reconstruction filter can limit the signal band to $[-B, B]Hz$, then the analog signals of the two branches can be reconstructed with amplitude and phase imbalance. Hence, the mismatch of DAC along with a low pass reconstruction filter is modelled on the reconstruction filter. Denoting $h_{I,LP}(t)$ and $h_{Q,LP}(t)$ as the equivalent impulse response of the reconstruction filters on the inphase and quadrature branch respectively, the baseband signals in Eq. (3.1) become:

$$x'_I(t) = (x_I(t) + O_{I0}) * h_{I,LP}(t) \tag{3.7}$$

$$x'_Q(t) = (x_Q(t) + O_{Q0}) * h_{Q,LP}(t) \tag{3.8}$$

where, O_{I0} and O_{Q0} are the DC offset of inphase and quadrature branch respectively. As the corrupted signal is still real-valued, the spectrum will be Hermitian symmetrical about the zero frequency. This means that the amplitudes for the positive and negative frequency are equal, whereas the phases for the positive and negative frequency are inverse.

The baseband analog signals will be upconverted to RF frequency band by a pair of quadrature local oscillators (LO). In practice, the two oscillators contribute

significantly to I/Q imbalance. This is not only caused by the mismatch of gain and phase, but also the difference of conversion gain at different frequencies. The latter exhibits an FD property, which is similar to the FD frequency response of RF amplifiers. Hence, the effect of the FD conversion gain of the oscillators will be modelled together with RF amplifier response. Aside from this, the modulators also suffer from carrier leakage, where the typical value is -60~-40 dB lower than the IF input. This carrier leakage effect can be equivalently considered to becaused by the DC bias of baseband components. Hence, the carrier leakage is modelled together with baseband DC offset. Denoting the gain and phase difference of LO as g and θ, the LO signal can be expressed as:

$$x_{I,lo}(t) = g\cos(2\pi f_c t + \theta) \tag{3.9}$$

$$x_{Q,lo}(t) = -\sin(2\pi f_c t) \tag{3.10}$$

Therefore, the modulated signals are:

$$x_{I,m}(t) = g \cdot (x_I(t) + O_{I0}) * h_{I,LP}(t) \cdot \cos(2\pi f_c t + \theta) \tag{3.11}$$

$$x_{Q,m}(t) = -(x_Q(t) + O_{Q0}) * h_{Q,LP}(t) \cdot \sin(2\pi f_c t) \tag{3.12}$$

It is worth noting that the output signals of modulator $X_{I,m}(f)$ and $X_{Q,m}(f)$ are still real-value which means the spectrum is Hermitian symmetrical about the zero frequency. The modulator transfers baseband spectrum to RF passband. The RF signal will suffer from I/Q imbalance from RF amplifiers and signal paths. Along with the previously mentioned FD conversion gain, the overall effect of the RF part can be modelled as RF bandpass filters $h_{I,LP}(t)$ and $h_{Q,LP}(t)$ where positive passband is $[f_c - f_B,\ f_c + f_B]Hz$. As these filters are real-valued, the corresponding spectrum is also Hermitian symmetrical about the zero frequency. Accordingly, the real filters can be regarded as a combination of a complex filter and its Hermitian symmetrical filter. Take the bandpass filter on the inphase branch as an example:

$$h_{I,BP}(t) = \hat{h}_{I,BP}(t) + \hat{h}^*_{I,BP}(t) \tag{3.13}$$

Furthermore, it is easy to construct a complex filter $\hat{h}_{I,BP}(t)$ where the non-zero frequency band is only restricted to $[f_c - f_B,\ f_c + f_B]Hz$ with a passband of $\hat{h}^*_{I,BP}(t)$ is $[-f_c - f_B,\ -f_c + f_B]Hz$. Equivalently, Eq. (3.13) can be rewritten as:

$$\begin{aligned} h_{I,BP}(t) &= \hat{h}_{I,BP}(t) + \hat{h}^*_{I,BP}(t) \\ &= \bar{h}_{I,BP}(t)e^{j2\pi f_c t} + \bar{h}^*_{I,BP}(t)e^{-j2\pi f_c t} \end{aligned} \tag{3.14}$$

According to Eq. (3.14), the bandpass filters at the RF passband can be considered as the frequency shift result of baseband complex filters $\bar{h}_{I,BP}(t)$ and $\bar{h}^*_{I,BP}(t)$ where the corresponding frequency band is constrained to $[-f_B, f_B]Hz$. As $\bar{h}_{I,BP}(t)$ exhibits the same frequency responsewith $h_{I,BP}(t)$ within the passband, this dissertation defines $\bar{h}_{I,BP}(t)$ as the baseband equivalent of $h_{I,BP}(t)$. Similarly, $\bar{h}_{Q,BP}(t)$ is defined as the baseband equivalent of $h_{Q,BP}(t)$:

$$h_{Q,BP}(t) = \bar{h}_{Q,BP}(t)e^{j2\pi f_c t} + \bar{h}^*_{Q,BP}(t)e^{-j2\pi f_c t} \tag{3.15}$$

Consequently, the output corrupted RF signal on inphase and quadrature branch can be written as:

$$x_{I,rf}(t) = x_{I,m}(t) * h_{I,BP}(t) \tag{3.16}$$

$$x_{Q,rf}(t) = x_{Q,m}(t) * h_{Q,BP}(t) \tag{3.17}$$

The final RF signal is the addition of signals from the inphase and quadrature branches:

$$\begin{aligned} x_{rf}(t) &= x_{I,m} * h_{I,BP}(t) + x_{Q,m} * h_{Q,BP}(t) \\ &= \frac{g}{2} \cdot [\ (x_I(t) + O_{I0}) * h_{I,LP}(t) * \bar{h}_{I,BP}(t) \cdot e^{j2\pi f_c t + \theta} \\ &\quad + (x_I(t) + O_{I0}) * h_{I,LP}(t) * \bar{h}^*_{I,BP}(t) \cdot e^{-j2\pi f_c t - \theta}\ ] \\ &\quad - \frac{1}{2j}[\ (x_Q(t) + O_{Q0}) * h_{Q,LP}(t) * \bar{h}_{Q,BP}(t) \cdot e^{j2\pi f_c t} \\ &\quad - (x_Q(t) + O_{Q0}) * h_{Q,LP}(t) * \bar{h}^*_{Q,BP}(t) e^{-j2\pi f_c t}\ ] \end{aligned} \tag{3.18}$$

After some mathematic substitutions, the above equation can be rewritten as [81]:

$$\begin{aligned} &X_{rf}(f) \\ &= \underbrace{\{\ X(f-f_c)\,[\ H_{I,LP}(f-f_c) \cdot \bar{H}_{I,BP}(f-f_c) g e^{j\theta} + H_{Q,LP}(f-f_c) \cdot \bar{H}_{Q,BP}(f-f_c)\ ]}_{(a)} \\ &+ \underbrace{X^*(-f+f_c)\,[\ H_{I,LP}(f-f_c) \cdot \bar{H}_{I,BP}(f-f_c) g e^{j\theta} - H_{Q,LP}(f-f_c) \cdot \bar{H}_{Q,BP}(f-f_c)\ ]}_{(b)} \\ &+ \underbrace{X^*(-f-f_c)\,[\ H_{I,LP}(f+f_c) \cdot \bar{H}^*_{I,BP}(-f-f_c) g e^{-j\theta} + H_{Q,LP}(f+f_c) \cdot \bar{H}^*_{Q,BP}(-f-f_c)\ ]}_{(c)} \\ &+ \underbrace{X(f+f_c)\,[\ H_{I,LP}(f+f_c) \cdot \bar{H}^*_{I,BP}(f-f_c) g e^{-j\theta} - H_{Q,LP}(f+f_c) \cdot \bar{H}^*_{Q,BP}(-f-f_c)\ ]}_{(d)} \\ &+ O_{I0} \cdot H_{I,LP}(f_c) \bar{H}_{I,BP}(f_c) e^{j\theta} + O_{I0} \cdot H_{I,LP}(-f_c) \bar{H}^*_{I,BP}(-f_c) e^{-j\theta} \\ &+ jO_{Q0} \cdot H_{Q,LP}(f_c) \bar{H}_{Q,BP}(f_c) - jO_{Q0} \cdot H_{Q,LP}(-f_c) \bar{H}^*_{Q,BP}(-f_c)\ \} \end{aligned} \tag{3.19}$$

The coefficients in term (a) and (b) are defined as:

$$G_1(f) = g e^{j\theta} H_I(f) + H_Q(f) \tag{3.20}$$

$$G_2(f) = g e^{j\theta} H_I(f) - H_Q(f) \tag{3.21}$$

where

$$H_I(f) = H_{I,LP}(f) \cdot \bar{H}_{I,BP}(f) \tag{3.22}$$

$$H_Q(f) = H_{Q,LP}(f) \cdot \bar{H}_{Q,BP}(f) \tag{3.23}$$

Consequently, Eq. (3.19) can be rewritten as:

$$\begin{aligned} X_{rf}(f) = & X(f-f_c)G_1(f-f_c) + X^*(-f+f_c)G_2(f-f_c) \\ & + X^*(-f-f_c)G_1^*(-f-f_c) + X(f+f_c)G_2^*(-f-f_c) \\ & + O_{dc} \end{aligned} \tag{3.24}$$

where O_{dc} is the dc terms caused by dc offset in relation to baseband and carrier leakage.

The above equation gives an overview of the corrupted signal spectrum. Comparing Eq. (3.19) with the signal spectrum of ideal DCT in Eq. (3.6) , terms (a) and (c) represent the desired components around f_c and $-f_c$. It is easy to know that the coefficients for $X(f-f_c)$ and $X^*(-f-f_c)$ are Hermitian symmetrical in term (a) and (c). Thus, the effect of I/Q imbalance on the desired components can be regarded as channel processing. This means that, given term (a) and (c), the original signal can be recovered by channel estimation. However, the term (a) and (c) cannot be explicitly obtained from Eq. (3.24). This is because the image terms (b) and (d) overlap the desired components around f_c and $-f_c$. These image components cause interference with the original signals, as shown in Fig. 3.5. Therefore, the capability of image suppression is a key performance criterion for DCTs and it is characterized by image rejection ratio (IRR). The IRR is defined to be to the logarithm power ratio between the image and desired components:

$$IRR_{dB}(f) = 10\log_{10}\left(\left|\frac{G_1(f)}{G_2(f)}\right|^2\right) \tag{3.25}$$

The typical IRR for general DCT without compensation is around 25~40 dB [18]. As the image components interfere with the desired component, it is essential to reduce the DCT IRR using the compensation filter. The next two sections will discuss algorithms for the estimation and the compensation of the above parameters.

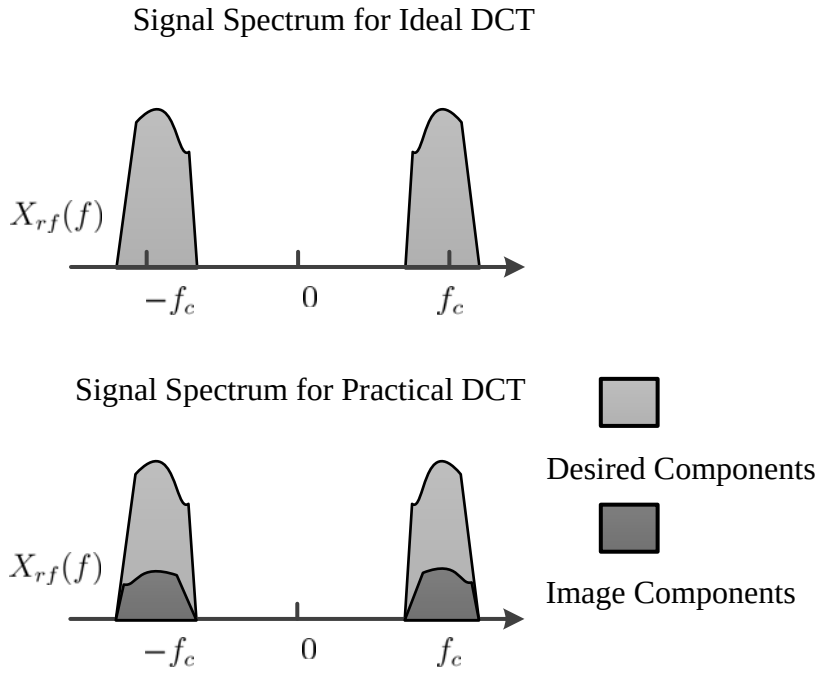

Figure 3.5 Signal Spectrum for Ideal and Practical DCT

3.3 Conventional I/Q imbalance estimation methods

It is crucial to estimate the previously mentioned parameters before the I/Q imbalance is compensated. To achieve this, the signal feedback path that down-converts the transmitted signal and digitizes the signal will be used. From the point of view of feedback architecture, categorization can effectively be divided into two classes [17, 18, 26, 28, 76, 79]:

1). Diode based architecture.

2). Low-IF receiver architecture. This section will present a brief overview of these two architectures. Based on these two architectures, this dissertation proposes a low cost, low computational complexity estimation method.

3.3.1 Diode based estimation methods

This architecture makes use of the diode in the transmitter power detector as shown in Fig. 3.6. The feedback path consists of diode, ADC and DSP. The diode exhibits square law characteristic:

$$x_{diode}(t) = k \cdot x_{rf}^2(t) \tag{3.26}$$

Because of the square law characteristic, the output of the diode contains baseband components which will be digitized by the ADC. The DSP estimates I/Q imbalance parameters. There exist many diode based estimation methods in the relevant the literature [22, 24, 29]. This subsection presents an overview of two common methods and shows how a diode could contribute to the proposed estimation algorithm.

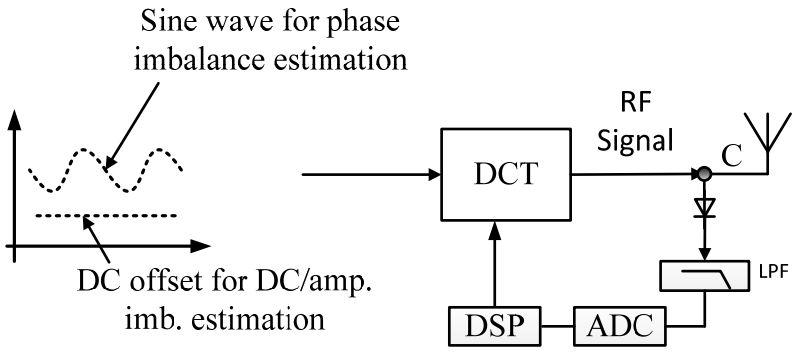

Figure 3.6 Transmitter with Diode-based Feedback path

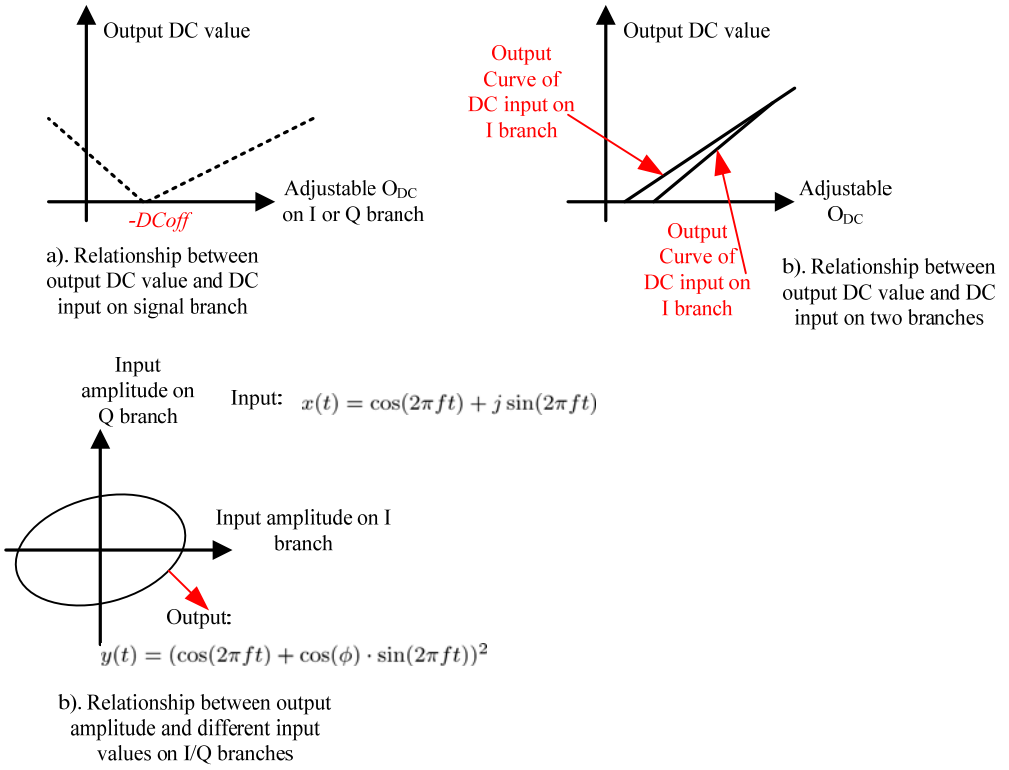

Figure 3.7 IQ Imbalance Estimation in Literature [22]

In [22], the author proposes iteratively employing an adjustment algorithm to estimate the I/Q imbalance. This method assumes the DCT only from LO imbalance and LO leakage. The LO leakage is estimated by zeroing the input signal ($x(t) = 0$) and then adjusting the DC offset. As shown in Fig. 3.6, DC offset and sine wave are injected into the DCT. The relationship between input DC value and output DC value can be easily understood in Fig. 3.7. The optimum estimate of DC offset is obtained when the output of the diode contains a minimum of DC components. Similarly, the gain imbalance g can be estimated by transmit adjustable the DC components on I and Q branch: $x(t) = O_i + j0$ and $x(t) = 0 + jO_q$, respectively. Then g is obtained when the value of O_i and O_q has the same amplitude. As shown in Fig. 3.7. After amplitude and DC offset the constant amplitude signal $x(t) = \cos(2\pi ft) + j\sin(2\pi ft)$ is injected into DCT. Due to the phase error, the amplitude can is an eclipse function with respect of input amplitude of I and Q branch. And the phase can be obtained by solve the output amplitude function $y(t) = (\cos(2\pi ft) + \cos(\phi) \cdot \sin(2\pi ft))^2$ and input function $x(t) = \cos(2\pi ft) + j\sin(2\pi ft)$. This method explicitly utilizes Eq.

(3.26). The RF signal is converted to the baseband by the intermodulation of carrier and test signal $x(t)$.Then, the imbalance parameters of LO can be directly estimated using the above methods.

In [29], the author estimates the I/Q imbalance by transmitting a two-tone signal $x(t) = A\cos(2\pi f_1 t + \phi_1) + jA\sin(2\pi f_2 t + \phi_2)$ and calculating the imbalance parameters by applying a series of matrix operations to the received signal. The principle behind this method is that the RF signal carrying I/Q imbalance information is down-converted to the baseband by the intermodulation between the modulated two tones and carrier. As a result, the tones locate at frequency f_1, f_2, $2f_1$, $2f_2$ and $f_1 + f_2$ of the diode output signal will carry I/Q imbalance information and form solvable equations.

The diode based method provides a low cost estimation solution, which does not require external calibration instruments and modifications of transmitter internal circuits. However, these methods mainly assume the DCT only suffers from LO imbalance and leakage. For wideband systems, it also suffers FD factors such as imbalanced filters and amplifiers. Therefore low cost diode-based FD I/Q imbalance estimation algorithms is necessary to be further developed.

3.3.2 LOW-IF based estimation methods

Though quadrature feedback architecture can theoretically estimate I/Q imbalance, it is rarely used because it actually creates extra I/Q imbalance. A more popular method is to use a low IF feedback path as shown in Fig. 3.8 [18, 26, 28, 82, 83]. This feedback path can employ external instruments such as a spectrum analyzer or internal modules.

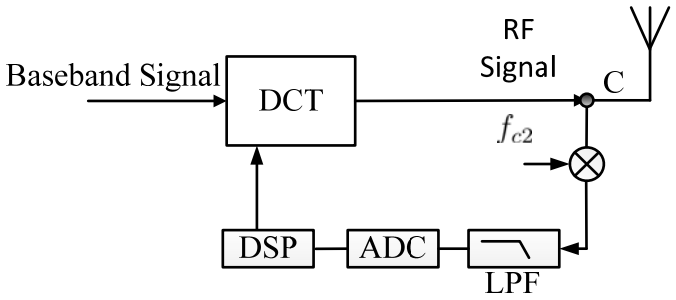

Figure 3.8 Transmitter with Low-IF Receiver Feedback Path

As shown in Fig. 3.8, the single-branch receiver consists of a low IF down-converter, lowpass filter, ADC and DSP. The transmitted signal is firstly down-converted to a low IF frequency $\pm f_I$ from the LO frequency $\pm f_c'$ by the converter. Aside from the components around f_I, this step will also produce components around $\pm(f_c + f_I)$. These high frequency components are then filtered out to prevent aliasing. Afterwards, the IF signal is digitized by the ADC. Then the single-branch digital signal is I/Q-demodulated in the digital domain. As this demodulation in the digital domain is strictly orthogonal, it does not introduce extra I/Q imbalance. The information of the transmitter inphase and quadrature branch can be calculated in the DSP using an estimation algorithms.

Though the additional I/Q imbalance is avoided by the digital domain I/Q demodulation, this architecture still faces some challenges, including receiver LO leakage and synchronization error. The receiver LO leakage component will explicitly locate at $\pm f_I$. Hence, the mean of LO leakage can be calculated before estimating the transmitter I/Q imbalance. Then the receiver LO leakage can be mitigated by adding proper DC terms at the transmitter [23, 24, 26]. Regarding the synchronization problem, this includes frequency synchronization and timing-synchronization. The frequency synchronization can be achieved using the same reference frequency source with the transmitter. Some data aided algorithms in the relevant literature can be used to obtain the timing synchronization, such as the Maximum Likelihood (ML) method in [84].

The transmitter I/Q imbalance parameters can be estimated based on the demodulated I/Q data. There are a great number of I/Q-demodulation based estimation algorithms, such as the second-order statistics-based approach and the wide linear least square (WL-LS) approach [18]. This subsection will give a brief overview of WL-LS and explain the principle of the I/Q-demodulation based estimation methods. The LO leakage estimation details will be found in [29] for further study.

Eq. (3.24) presents a complete expression for the I/Q imbalanced signal. Omitting the DC terms, the baseband equivalent model of the imbalanced RF signal is [79]:

$$X_{eq}(f) = X(f)G_1(f) + X^*(-f)G_2(f) \tag{3.27}$$

And the corresponding time domain expression is:

$$x_{eq}(t) = x(t) * g_1(t) + x^*(t) * g_2(t) \tag{3.28}$$

After being digitized, the observed demodulated signal will take the following form:

$$y(n) = x(n) * g_1(n) + x^*(n) * g_2(n) \tag{3.29}$$

Assuming that the imbalanced filter $g_1(n)$ and $g_2(n)$ have a finite impulse response and the length of response is N_g, for a segment of observed signal $\mathbf{y}(n)$, it can be expressed in the form of a convolution matrix:

$$\mathbf{y}(n) = \mathbf{X}(n)\tilde{\mathbf{g}}_1 + \mathbf{X}^*(n)\tilde{\mathbf{g}}_2 \tag{3.30}$$

where $\mathbf{y}(n) = [y(n), y(n-1), \cdots, y(n-N+1)]^T$, N is the number of observed data; and $\tilde{\mathbf{g}}_i = [\tilde{g}_{i,1}, \tilde{g}_{i,2}, \cdots, \tilde{g}_{i,N_g}]^T$, $i = 1, 2$ represents the impulse response of the imbalanced filters; the convolution matrix $\mathbf{X}(n)$ has the following form:

$$\mathbf{X}(n) = \begin{bmatrix} x(1) & 0 & 0 & 0 \\ x(2) & x(1) & 0 & 0 \\ \vdots & \vdots & \vdots & \vdots \\ x(N_g-1) & x(N_g-2) & \cdots & 0 \\ x(N_g) & x(N_g-1) & \cdots & x(1) \\ \vdots & \vdots & \ddots & \vdots \\ \vdots & \vdots & x(L) & x(L-1) \\ 0 & 0 & 0 & x(L) \end{bmatrix}_{N\times L} \tag{3.31}$$

Eq. (3.30) can then be rewritten as:

$$\mathbf{y}(n) = \left[\mathbf{X}(n) \mid \mathbf{X}^*(n)\right] \begin{bmatrix} \tilde{\mathbf{g}}_1 \\ \tilde{\mathbf{g}}_2 \end{bmatrix} = \mathbf{X}_b(n) \begin{bmatrix} \tilde{\mathbf{g}}_1 \\ \tilde{\mathbf{g}}_2 \end{bmatrix} \tag{3.32}$$

The impulse response of the imbalanced filters can be estimated based on least square (LS):

$$\begin{bmatrix} \hat{\mathbf{g}}_1 \\ \hat{\mathbf{g}}_2 \end{bmatrix} = \mathbf{X}_b^+(n)\mathbf{y}(n) \tag{3.33}$$

where $\mathbf{X}_b^+(n)$ is the pseudo-inverse of $\mathbf{X}_b(n)$. If $\mathbf{X}_b^H(n)\mathbf{X}_b(n)$ is invertible, the pseudo-inverse can be calculated as: $\mathbf{X}_b^+(n) = \left(\mathbf{X}_b^H(n)\mathbf{X}_b(n)\right)^{-1}\mathbf{X}_b^H(n)$ [85].

Theoretically, this estimation method is applicable for any form of signal. But for some narrowband signals, the matrix $\mathbf{X}_b^H(n)\mathbf{X}_b(n)$ could be ill conditioned. This can be mitigated by adding low-level white circular noise to $x(n)$. It is worth noting that the estimated imbalance filters include common gain from both transmitter and receiver. These parameters can be directly applied to the pre-distortion filter and the distortion caused by common gain will be cancelled out, which will be explained in detail in further sections.

The WL-LS method relies on the received data $\mathbf{y}(n)$ and matrix $\mathbf{X}_b^+(n)$. For $\mathbf{y}(n)$, it requires strictly I/Q-demodulation. For $\mathbf{X}_b^+(n)$, it requires matrix inversion operation which is computational complex. There exist many other estimation

methods [18, 26, 72]. These algorithms are based on low-IF single-branch receivers, as shown in Fig. 3.8. Generally, these architectures are expensive and heavy in computational complexity.

3.4 Proposed I/Q imbalance estimation method

The previously mentioned estimation methods are constrained by the following factors: the diode based method is low cost but only applicable for narrowband DCTs; the low-IF receiver method can deal with FD I/Q imbalance for wideband DCTs, but is cost ineffective and consumes a lot of computational resources. This dissertation combines the advantages of these two methods and proposes a self-I/Q-demodulation compensation scheme which omits the external I/Q demodulator to reduce the cost.

The self-compensation algorithms in [18, 29, 84] make use of a diode in the power detector for I/Q imbalance parameter estimation. In these schemes, the RF signal is self-demodulated by the square law of the diode. However, the estimation is constrained to FI I/Q imbalance because the diode and ADC can only cope with narrowband signal. Enlightened by these estimation methods, the chapter proposes a wideband diode or even a multiplier to be used for FD I/Q imbalance estimation, as shown in Fig. 3.9. Based on this hardware architecture, a specific algorithm is required to realize the FD I/Q imbalance estimation.

The reason that the low-IF receiver architecture can cope with the FD I/Q imbalance is that it utilizes I/Q demodulation and the wideband complex signal can be recovered accordingly. Whereas in conventional diode based architecture, the diode only outputs the instantaneous power of the signal, which results in the loss of the complex information. Therefore, in order to estimate the FD I/Q imbalance parameters, the proposed wideband diode-based architecture should be able to realize I/Q demodulation for the transmitted signal. However, the constraint of this architecture is that this architecture lacks an external intermediate frequency source for down-conversion. Thus self-I/Q-demodulation

can only be realized using an LO transmitter or the transmitted signal itself under the condition that the external demodulator is omitted.

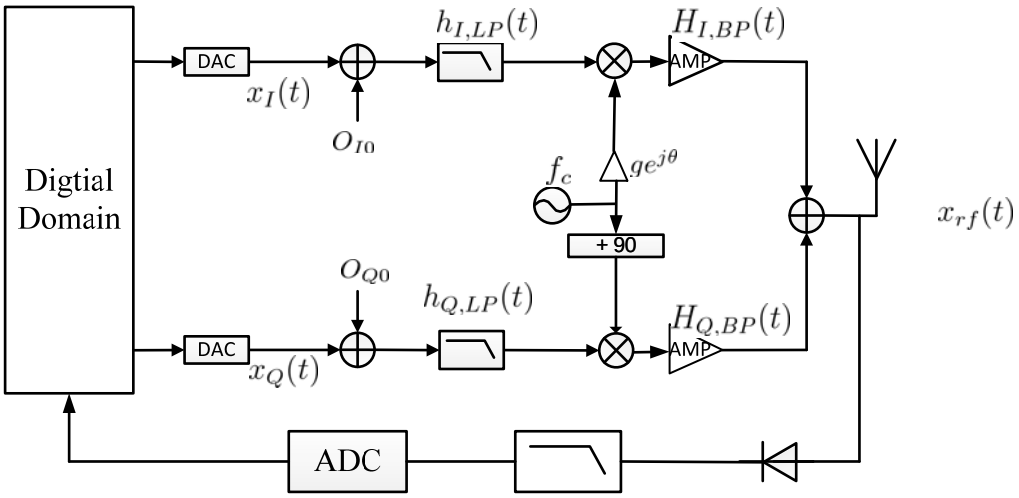

Figure 3.9 Proposed Estimation Architecture

Hence, the proposed algorithm utilizes two critical factors: LO transmitter and wideband diode. Based on this, the algorithm is designed so that the signal can be self-demodulated by the non-ideal transmitter quadrature LO pair through the wideband diode. However, the constraints are as follows:

1). The wideband diode only allows single-branch demodulation even though the quadrature LO transmitter is available for I/Q de-modulation.

2). The pair of quadrature transmitter LOs are corrupted by its inherent impairments: g, θ, O_{I0} and O_{Q0}.

Recalling the I/Q demodulation in the previous section, the principle of perfect I/Q demodulation is that the demodulator realizes this by mixing the transmitted RF signal with a pair of quadrature carriers on the inphase and quadrature branches simultaneously, as shown in Fig. 3.10 (a). For this proposed architecture, the interference arises if the inphase and quadrature LO are transmitted simultaneously. Hence, if the single I or Q branch signal $x_{rf}(t)$, along with the inphase or quadrature LO, is transmitted at a different time, the self-I/Q-

demodulation of single I or Q branch signal can be achieved with the help of the square law of the diode. With reference to this, this dissertation realizes I/Q demodulation by dividing the classical demodulation into two steps: inphase demodulation and quadrature demodulation, as shown in Fig. 3.10 (b). In the first step, the inphase carrier and training signal is transmitted. Due to the intermodulation of the diode, the inphase demodulation can be realized. The quadrature demodulation is realized in a similar way in which the quadrature carrier and training signal is transmitted. This method can be viewed as "time division" realization of I/Q demodulation. The phase delay caused by the "time division" is cancelled out by the intermodulation and the training signal which will be shown with further mathematical derivation.

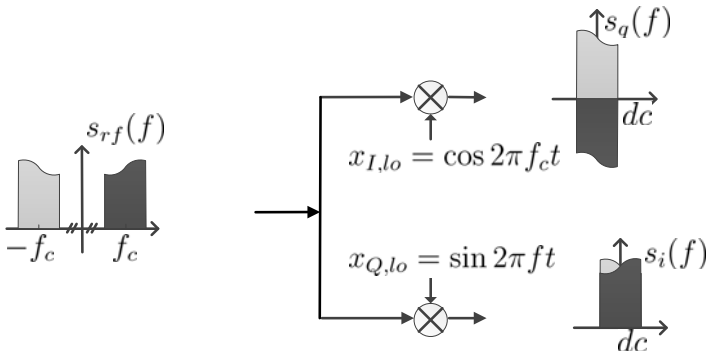

a). Quadrature Demodulator Method

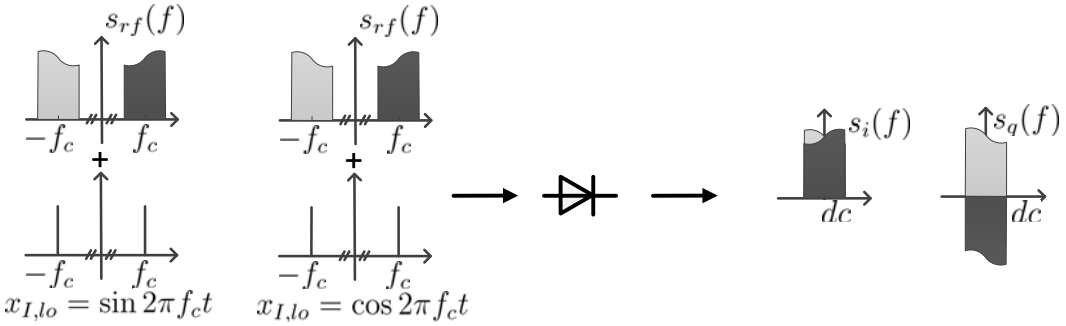

b). Diode Method

Figure 3.10 I/Q demodulation

Though the "time division" method provides a solution for I/Q demodulation by using a diode, the constraint of the imbalanced LO will corrupt the demodulated

signal and introduce additional error. Thus, an accurate estimation of the LO imbalance$g$, θ, O_{I0} and O_{Q0} is essential to compensate for this error. Accordingly, the proposed estimation will firstly estimate the LO imbalance. Then the overall FD I/Q imbalance will be estimated. The estimation process is depicted in Fig. 3.11. As Fig. 3.11 shows, the estimation process will be consisted of 7 steps. In each step, specific train signal will be transmitted to get the corresponding measurements. In step 1 and 2, $x_1(t)$ and $x_5(t)$ will be transmitted to estimate the LO gain imbalance g, θ and DC offset $O_{I0}O_{Q0}$. Then, the imperfection of LO will be compensated using these estimated values. Afterwards, the LO can be regarded as ideal and there still exists frequency-dependent imbalance on RF branch. In steps 4~7, signal $x_6(t) \sim x_7(t)$ will be transmitted to estimate the frequency imbalance. At last, the overall I/Q imbalance can be obtained.

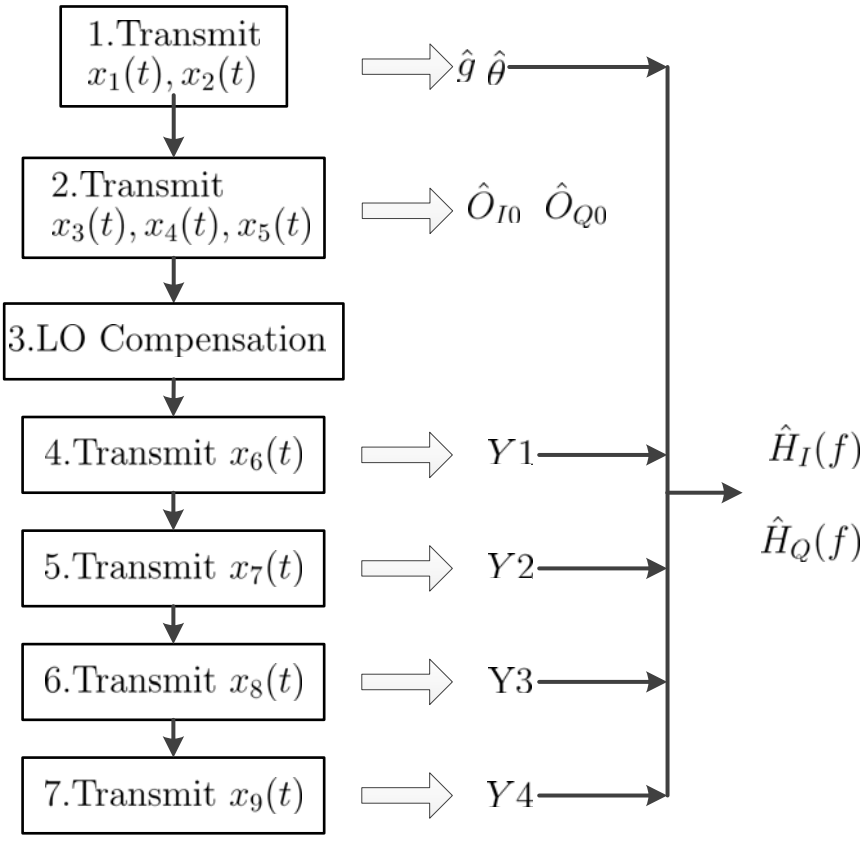

Figure 3.11Frequency-dependent I/Q Imbalance Estimation Procedure

3.4.1 LO impairments and DC offset estimation

There exist many diode based LO imbalance estimation methods in the referenced literature [18, 29, 84]. Apart from the previously mentioned methods, [84] proposes a measurement approach, which makes use of a diode in the envelope detector. However it is only suitable for QPSK and Continuous Phase Modulation (CPM) systems. [18] and [29] proposes estimation methods in generic situations. In these methods, I/Q imbalance information is obtained from the intermodulation results between the carriers and test tones. Nonetheless, the computational complexity is relatively high because of the matrix inversion operation when a large number of samples are involved.

In this thesis, the LO impairments g, θ, O_I and O_Q will be estimated at low complexity with the help of a specially designed test signal. Consider two tones that have frequencies f_d and f_r close to each other and are passed through a diode, as shown in Fig. 3.12 (a) and (b). Due to the square law of the diode, these two tones intermodulate with each other and this results in tones which are located at $\pm(f_d + f_r)$ and $\pm(f_d - f_r)$ respectively. Actually, these tones contain the LO impairments information. If the frequencies f_d and f_r are low enough, the signal is narrowband and the imbalance parameter can be viewed as FI, which means g, θ, O_{I0} and O_{Q0} can be obtained from the intermodulation products located at $\pm(f_d + f_r)$. In order to achieve this, the test tones are designed so that the tones that carry the LO impairment information of the inphase and quadrature branches can be down-converted to baseband, as described in the following steps:

a. Transmit signal $x_1(t) = x_{I1}(t) + j \cdot x_{Q1}(t)$ where $x_{I1}(t) = \cos(2\pi f_d t) + \cos(2\pi f_r t)$ and $x_{Q1}(t) = -\sin(2\pi f_r t)$ in I and Q branch. The signal spectrum is shown in Fig. 3.12 (a). Omitting the FD effect, the output signal of the diode can be rewritten as:

$$x_{diode}(t) = k x_{rf}^2(t) \tag{3.34}$$

where k is complex gain and

$$\begin{aligned} x_{rf}(t) =& \Re\Big\{ (O_{I0} + jO_{Q0}) e^{j2\pi f_c t} \\ &+ \frac{1}{2}\left(g e^{j\theta} + 1\right) e^{j2\pi(f_c+f_r)t} + \frac{1}{2}\left(g e^{j\theta} - 1\right) e^{j2\pi(f_c-f_r)t} \\ &+ \frac{1}{2} g e^{j\theta} (e^{j2\pi(f_c+f_d)t} + e^{j2\pi(f_c-f_d)t}) \Big\} * h \end{aligned} \tag{3.35}$$

Apply FFT to $x_{diode1}(t)$, and the complex gain of the tone at frequency $f_i = f_d - f_r$ is:

$$V_{f_i 1} = \left[g^2 + jg\sin\theta\right] \cdot K e^{j\varphi} \tag{3.36}$$

where $K^{j\varphi}$ is the overall gain of the transmitter and diode.

b. Similarly, transmit the signal $x_2(t) = x_{I2}(t) + j \cdot x_{Q2}(t)$ where $x_{I2}(t) = \cos(2\pi f_r t)$ and $x_{Q2}(t) = -(\sin(2\pi f_d t) + \sin(2\pi f_r t))$. The signal spectrum is shown in Fig. 3.12 (b) and the complex gain of the output signal at frequency $f_i = f_d - f_r$ is

$$V_{f_i 2} = [1 - jg\sin\theta] \cdot K e^{j\varphi} \tag{3.37}$$

c. Solving Eq. (3.36) and (3.37), we can get:

$$\hat{g} = \sqrt{\frac{\frac{\Im\{V_{f_i 1}\}}{rr} + \frac{\Re\{V_{f_i 1}\}}{ii}}{\frac{\Re\{V_{f_i 2}\}}{ii} + \frac{\Im\{V_{f_i 2}\}}{rr}}} \tag{3.38}$$

$$\hat{\theta} = \arcsin\left(\frac{\frac{\Im\{V_{f_i 1}\}}{\Im\{V_{f_i 2}\}} - \frac{\Re\{V_{f_i 1}\}}{\Re\{V_{f_i 2}\}}}{\frac{rr}{\Im\{V_{f_i 2}\}} + \frac{ii}{\Re\{V_{f_i 2}\}}} \cdot \frac{1}{\hat{g}} \right) \tag{3.39}$$

where $rr = \Re\{V_{f_i 1}\} + \Re\{V_{f_i 2}\}$ and $ii = \Im\{V_{f_i 1}\} + \Im\{V_{f_i 2}\}$

d. Estimation of DC offset. The DC offset can also be estimated by using the

Transmit signals $x_3(t) = x_{I3}(t) + j \cdot x_{Q3}(t)$ where $x_{I3}(t) = cos(2\pi f_d t)$, $x_{Q3} = 0$; $x_4(t) = x_{I4}(t) + j \cdot x_{Q4}(t)$ where $x_{I4} = 0$, $x_{Q4} = sin(2\pi f_d t)$ and $x_5(t) = x_{I5}(t) + j \cdot x_{Q5}(t)$ where $x_{I5} = 0$, $x_{Q5} = sin(2\pi f_d t) + O_{q5}$ and O_{q5} is the DC offset which goes with the sine wave. It should be note that as this method uses square law model, hence small signal will be applied. Large signal amplitude of sine wave and DC offset will introduce distortions, which results worse measurements. Assuming that the I and Q branch have been compensated, then the complex gain of signal 3, 4 and 5 at frequency f_d can be expressed as:

$$V_{f_d 3} = \left(g^2 O_{I0} + g \sin\theta O_{Q0}\right) \cdot G \tag{3.40}$$

$$V_{f_d 4} = -j \left(g \sin\theta O_{I0} + O_{Q0}\right) \cdot G \tag{3.41}$$

$$V_{f_d 5} = -j \left(g \sin\theta O_{I0} + O_{Q0} + O_{Q5}\right) \cdot G \tag{3.42}$$

where

$$\hat{O}_{I0} = \frac{V_{f_d 3} - \hat{g} \sin(\hat{\theta}) V_{f_d 4}}{\hat{g}^2 (1 - \sin^2(\hat{\theta})) \hat{G}} \tag{3.43}$$

$$\hat{O}_{Q0} = \frac{\hat{g} V_{fd4} - \sin\hat{\theta} V_{fd3}}{\hat{g}(1 - \sin^2(\hat{\theta}))\hat{G}} \tag{3.44}$$

$$\hat{G} = \frac{j(V_{f_d 5} - V_{f_d 4})}{O_{Q5}} \tag{3.45}$$

G is the path gain.

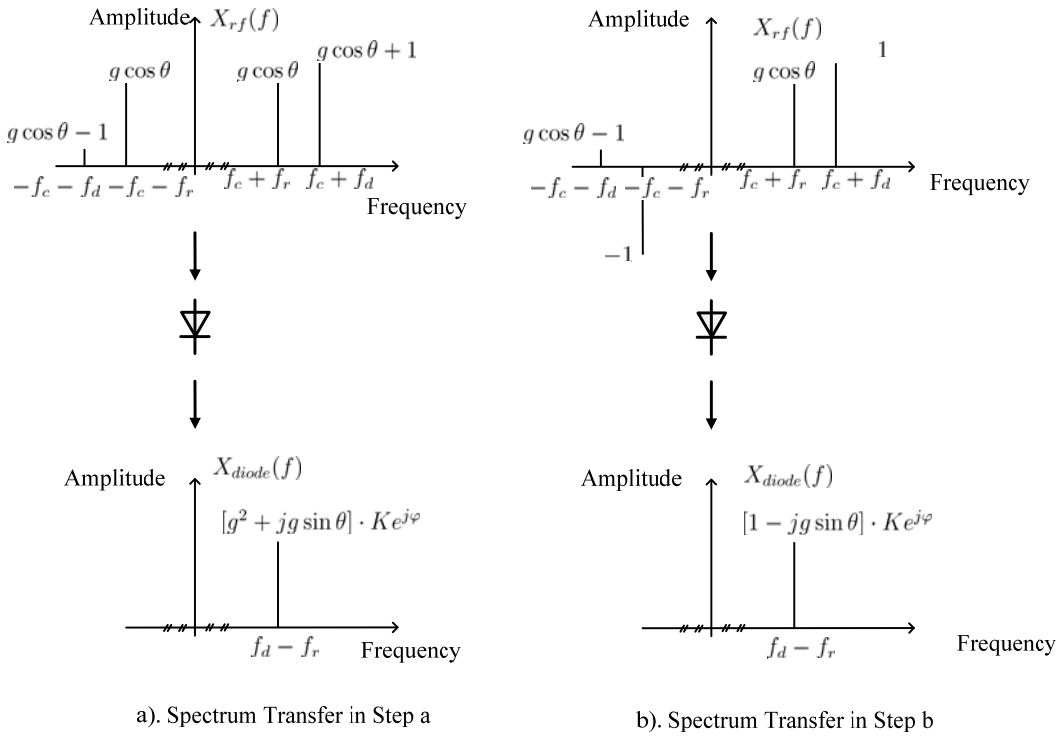

a). Spectrum Transfer in Step a

b). Spectrum Transfer in Step b

Figure 3.12 Signal Spectrum Transfer for Step a and b

The derivation of Eq. (3.36) and (3.37) could be verified by matlab simulation. In the simulation, the signal will be corrupted by LO related I/Q imbalance factors, namely, g and θ. Then the corrupted signal will pass through ideal diode model, as shown in Eq. (3.34).The amplitude of V_{fi1} and V_{fi2} at interested frequency point f_d are calculated from the spectrum of diode outpout, which are presented as red curve as shown in Fig. 3.13. Meanwhile, the amplitude of V_{fi1} and V_{fi2} at interested frequency point f_d are calculated from Eq. (3.46) and (3.47), as the blue curves shown in Fig. 3.13. The impairment factors g varies from 0.9 to 1.1 and θ is set to 0.1. The generated signal is added noise with SNR 30 dB. As Fig. 3.13 shows, we can find the amplitude of V_{fi1} and V_{fi2} calculated by derivation and simulation are very closed, which verifies the correctness of the derivation of Eq. (3.36) and (3.37).

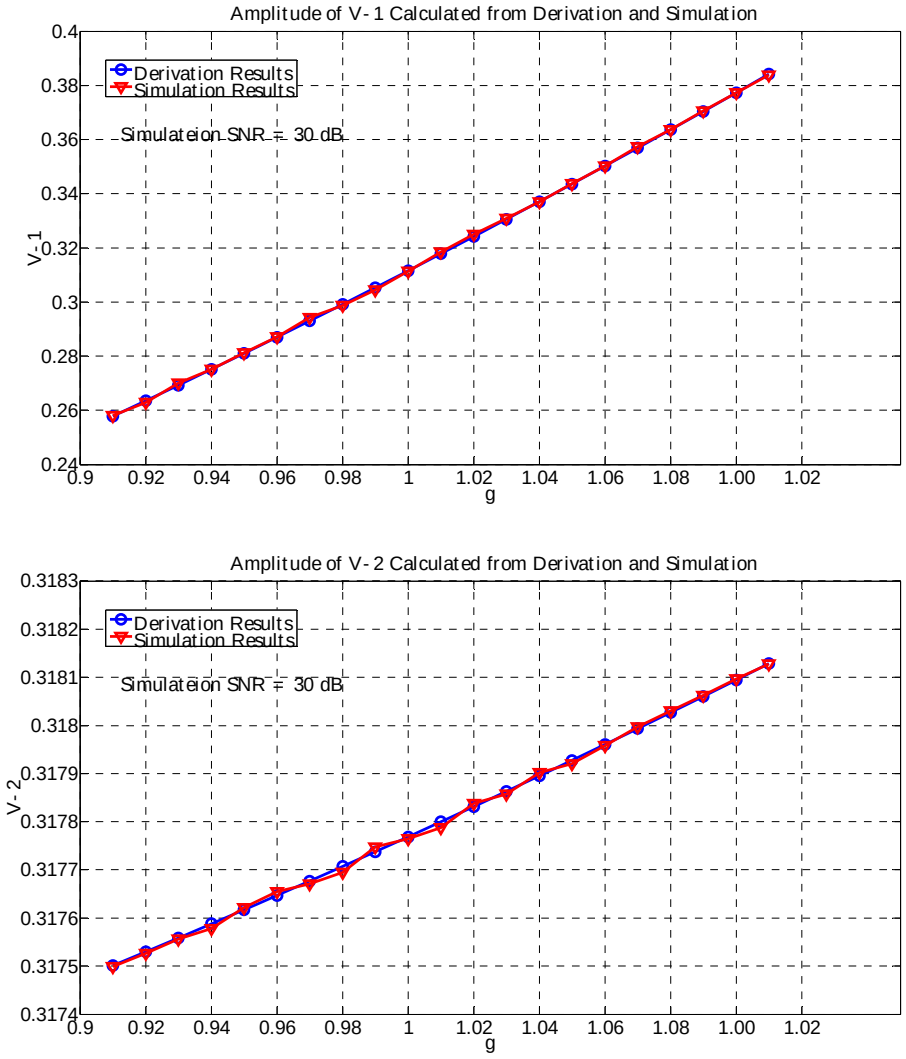

Figure 3.13 Amplitude of V_{fi1} and V_{fi2} Calculated from Derivation and Simulations

3.4.2 FD related I/Q impairment parameters estimation

After estimating the LO impairments, this section can estimate the overall I/Q imbalance filter $G_1(f)$ and $G_2(f)$ in Eq. (3.20) and (3.21). As presented earlier, the FD I/Q imbalance parameters can be estimated by using low-IF receiver architecture. The down-converted signal is digitized by high speed ADC. Then, in the digital domain, I/Q demodulation is realized with the help of a quadrature LO pair which are strictly orthogonal. The complex training signal is used in these methods. The imbalanced parameter carried by the modulated complex signal is obtained by a self-IQ-demodulation process. Theoretically, the complex training signal can be applied in the proposed “time division” I/Q demodulation scheme.

However, the complex signal is not essential to the whole process. Effectively, only the desired branch will transmit a training signal when the imbalanced filter of this branch is being estimated and another branch is "switched off". In other words, a real-valued signal instead of a complex-valued training signal will be used in this method. Though the conventional complex training signal can also be used, the real training signal outperforms the complex training signal, which will be shown in the simulation.

In addition, the conventional wideband training signal causes interference with itself when passing through the diode. Thus, the proposed estimation will adopt a single tone signal as a training signal. The wideband I/Q imbalance can be estimated at each frequency point within the band of interest. Effectively, the wideband training signal will severely degrade the estimation performance. This will be shown later in the laboratory experiment results. As the demodulation is "time division" and a real-valued training signal is only used, the "time division" I/Q demodulation can be divided into four steps, as shown in Table 3.1.

Table 3.1 "time division" I/Q Demodulation Process

"Time Division" Process	Corresponding Transmitted Signal
1. Inphase demodulation for inphase branch signal	$x_I(t) + LO_I$
2. Quadrature demodulation for inphase branch signal	$x_I(t) + LO_Q$
3. Inphase demodulation for quadrature branch signal	$x_Q(t) + LO_I$
4. Quadrature demodulation for quadrature branch signal	$x_Q + LO_Q$

As the carrier leakage can be easily compensated using the estimation results from Section 3.4.1, this section will assume that the carrier leakage is already compensated and it omits the carrier leakage term in the mathematic derivation. The period of training signal in each step is equally set to T. The detailed "time division" I/Q demodulation estimation process is presented as follows:

3.4.3 Inphase demodulation for inphase branch signal

In order to estimate the imbalanced filter on the inphase branch at an frequency of

interest f_d, the test tones will be transmitted on the inphase branch while the inphase and quadrature LO will also be transmitted by setting a DC offset as depicted in Section 3.4.3 and 3.4.4.

In this step, the test tones and LO will be transmitted on the inphase branch. Set the test tone as: $x_6(t) = x_{I6}(t) + j \cdot x_{Q6}(t)$ where $x_{I6}(t) = \cos(2\pi f_d t) + O_{I6}$ and $x_{Q6}(t) = 0$ in the first signal period $t \subseteq (0, T]$. Eq. (3.18) can be rewritten as:

$$x_{rf6}(t) = (\cos(2\pi f_d t) + O_{I6}) * h_{I,LP}(t) \cdot g\cos(2\pi f_c t + \theta) * h_{I,BP}(t) \tag{3.48}$$

In the frequency domain, Eq. (3.48) can be written as:

$$\begin{aligned} X_{rf6}(f) \approx g \cdot [& (\delta(f - f_c - f_d) + \delta(f - f_c + f_d)) \cdot H_{I,LP}(f - f_c) \cdot \bar{H}_{I,BP}(f - f_c) g e^{j\theta} \\ & + (\delta(f + f_c - f_d) + \delta(f + f_c + f_d)) \cdot H_{I,LP}(f + f_c) \cdot \bar{H}^*_{I,BP}(-f - f_c) g e^{-j\theta} \ ] \\ & + g \cdot O_{I6} \cdot \left(\delta(f - f_c) e^{j\theta} + (\delta(f + f_c) e^{-j\theta}\right) \\ = g \cdot [& \ (\delta(f - f_c - f_d) + \delta(f - f_c + f_d)) \cdot H_I(f - f_c) \cdot g e^{j\theta} \\ & + (\delta(f + f_c - f_d) + \delta(f + f_c + f_d)) \cdot H^*_I(-f - f_c) \cdot g e^{-j\theta} \ ] \\ & + g \cdot O_{I6} \cdot \left(\delta(f - f_c) e^{j\theta} + (\delta(f + f_c) e^{-j\theta}\right) \end{aligned} \tag{3.49}$$

where $H_I(f) = H_{I,LP}(f) \cdot \bar{H}_{I,BP}(f)$ is the baseband equivalent imbalanced filter on the inphase branch.

According to Eq. (3.49), the output signal of the diode in the frequency domain will be:

$$\begin{aligned} Y_{diode6}(f) = & \ FFT\left\{k x^2_{rf6}(t)\right\} \\ = & \ K \cdot X_{rf6}(f) * X_{rf6}(f) \\ = & \ K \cdot O^2_{I6} \cdot [\ \delta(f + f_d) \cdot g^2 \cdot (H_I(f) + H^*_I(-f)) \\ & + \delta(f - f_d) \cdot g^2 \cdot (H_I(f) + H^*_I(-f)) \ ] \\ & + I_s(f) + I_{DC}(f) \end{aligned} \tag{3.50}$$

where K is the overall complex gain; $I_s(f)$is the higher order intermodulation results; and $I_{DC}(f)$ is the intermodulation results at DC.

As shown in Eq. (3.50), the first two terms are located at $\pm f_d$, which indicates that the RF frequency response of I branch is shifted to baseband by the LO from the inphase branch. The last two components are clearly separated from the tones of interest. Hence, it is straight forward to calculate the value of $H_I(f) + H_I^*(-f)$ by applying FFT to the diode signal. The value of $H_I(f) + H_I^*(-f)$ at the interested frequency f_d is:

$$H_I(f_d) + H_I^*(-f_d) = \frac{Y_{diode6}(f_d)}{O_{I6}^2 \cdot g^2 \cdot K} = Y1 \tag{3.51}$$

The overall complex gain K is unknown in this equation. However, it is unnecessary to estimate K, and it will be shown later that this common complex gain will be cancelled out by the compensator.

3.4.4 Quadrature demodulation for inphase branch signal

In order to estimate $H_I(f)$, the LO will also be transmitted separately on the quadrature branch. Transmit signal $x_7(t) = x_{I7}(t) + j \cdot x_{Q7}(t)$ where $x_{I7}(t) = \cos(2\pi f_d t)$ and $x_{Q7}(t) = O_{Q7}$ in the second signal period $t \subseteq (T, 2T]$. Eq. (3.18) can be rewritten as:

$$\begin{aligned} x_{rf7}(t) = &\cos(2\pi f_d t) * h_{I,LP}(t) \cdot g\cos(2\pi f_c t + \theta) * h_{I,BP}(t) \\ &- O_{Q7} * h_{Q,LP}(t) \cdot \sin(2\pi f_c t) * H_{Q,BP} \end{aligned} \tag{3.52}$$

In the frequency domain, Eq. (3.52) can be written as:

$$
\begin{aligned}
X_{rf7}(f) \approx & [(\delta(f-f_c-f_d)+\delta(f-f_c+f_d))\cdot H_{I,LP}(f-f_c)\cdot \bar{H}_{I,BP}(f-f_c)ge^{j\theta} \\
& +(\delta(f+f_c-f_d)+\delta(f+f_c+f_d))\cdot H_{I,LP}(f+f_c)\cdot \bar{H}^*_{I,BP}(-f-f_c)ge^{-j\theta}\ ] \\
& +j\cdot O_{Q7}\cdot(\delta(f-f_c)-(\delta(f+f_c)) \\
\\
= & g\cdot[\ (\delta(f-f_c-f_d)+\delta(f-f_c+f_d))\cdot H_I(f-f_c)\cdot ge^{j\theta} \\
& +(\delta(f+f_c-f_d)+\delta(f+f_c+f_d))\cdot H^*_I(-f-f_c)\cdot ge^{-j\theta}\ ] \\
& +j\cdot O_{Q7}\cdot(\delta(f-f_c)-(\delta(f+f_c))
\end{aligned}
\tag{3.53}
$$

According to Eq. (3.53), the output signal of the diode in the frequency domain will be:

$$
\begin{aligned}
Y_{diode7}(f) = & \ FFT\left\{kx^2_{rf7}(t)\right\} \\
= & \ K\cdot X_{rf7}(f) * X_{rf7}(f) \\
= & \ K\cdot O^2_{Q7}\cdot[\ \delta(f+f_d)\cdot\left(ge^{-j\theta}H^*_I(-f)-ge^{j\theta}H_I(f)\right) \\
& -\delta(f-f_d)\cdot\left(g^{j\theta}H_I(f)-ge^{-j\theta}H^*_I(-f)\right)\ ] \\
& +I_s(f)+I_{DC}
\end{aligned}
\tag{3.54}
$$

where K is the overall complex gain; $I_s(f)$is the higher order intermodulation results; and $I_{DC}(t)$ is the intermodulation results at DC.

As shown in Eq. (3.54), the first two terms are located at $\pm f_d$, which indicates that the RF frequency response of I branch is shifted to baseband by the LO from the inphase branch. The last components are clearly separated from the interested tones. Hence, it is straightforward to calculate the value of $ge^{-j\theta}H^*_I(-f)-ge^{j\theta}H_I(f)$ by applying FFT to the diode signal. The value of $ge^{-j\theta}H^*_I(-f)-ge^{j\theta}H_I(f)$ at the interested frequency f_d is:

$$
ge^{-j\theta}H^*_I(-f_d)-ge^{j\theta}H_I(f_d)=\frac{Y_{diode7}(f_d)}{jO^2_7\cdot K}=Y2 \tag{3.55}
$$

Section 3.4.3 and 3.4.4 provides the method with which to estimate the

imbalanced filter on the inphase branch; the next sections will present the method to estimate the imbalanced filter $H_Q(t)$ on the quadrature branch.

3.4.5 Inphase demodulation for quadrature branch signal

In order to estimate $H_Q(f)$, the LO will also be transmitted separately on the inphase branch first. Transmit signal $x_8(t) = x_{I8}(t) + j \cdot x_{Q8}(t)$ where $x_{I8}(t) = O_{I8}$ and $x_{Q8}(t) = \sin(2\pi f_d t)$ in the second signal period $t \subseteq (2T, 3T]$. Eq. (3.28) can be rewritten as:

$$\begin{aligned} x_{rf8}(t) =& O_{I8} * h_{I,LP}(t) \cdot g\cos(2\pi f_c t + \theta) * h_{I,BP}(t) \\ & - \sin(2\pi f_d t) * h_{Q,LP}(t) \cdot \sin(2\pi f_c t) * H_{Q,BP} \end{aligned} \tag{3.56}$$

In the frequency domain, Eq. (3.56) can be written as:

$$\begin{aligned} X_{rf8}(f) \approx & [(\delta(f - f_c - f_d) - \delta(f - f_c + f_d)) \cdot H_{Q,LP}(f - f_c) \cdot \bar{H}_{Q,BP}(f - f_c) \\ & + (\delta(f + f_c - f_d) - \delta(f + f_c + f_d)) \cdot H_{Q,LP}(f + f_c) \cdot \bar{H}^*_{Q,BP}(-f - f_c)\ ] \\ & + \cdot O_{I8} \cdot \left(\delta(f - f_c) g e^{j\theta} + (\delta(f + f_c) g e^{-j\theta}\right) \\ \\ = & [\ (\delta(f - f_c - f_d) - \delta(f - f_c + f_d)) \cdot H_Q(f - f_c) \\ & - (\delta(f + f_c - f_d) - \delta(f + f_c + f_d)) \cdot H^*_Q(-f - f_c)\ ] \\ & + \cdot O_{I8} \cdot \left(\delta(f - f_c) g e^{j\theta} + (\delta(f + f_c) g e^{-j\theta}\right) \end{aligned} \tag{3.57}$$

According to Eq. (3.57), the output signal of the diode in the frequency domain will be:

$$\begin{aligned} Y_{diode8}(f) =& \ FFT\left\{k x^2_{rf8}(t)\right\} \\ =& \ K \cdot X_{rf8}(f) * X_{rf8}(f) \\ =& K \cdot O^2_{I8} \cdot [\ \delta(f + f_d) \cdot \left(g e^{j\theta} H^*_Q(-f) - g e^{-j\theta} H_Q(f)\right) \\ & - \delta(f - f_d) \cdot \left(g^{-j\theta} H_Q(f) - g e^{j\theta} H^*_Q(-f)\right)\ ] \\ & + I_s(f) + I_{DC} \end{aligned} \tag{3.58}$$

where K is the overall complex gain; $I_s(f)$is the higher order intermodulation results; and $I_{DC}(t)$ is the intermodulation results at DC.

As shown in Eq. (3.58), the first two terms locates at $\pm f_d$, which indicates that the RF frequency response of I branch is shifted to baseband by the LO from inphase branch. The last components are clearly separated with the interested tones. Hence, it is straight forward to calculate the value of $ge^{j\theta}H_Q^*(-f) - ge^{-j\theta}H_Q(f)$ by applying FFT to the diode signal. The value of $ge^{j\theta}H_Q^*(-f) - ge^{-j\theta}H_Q(f)$ at the interested frequency f_d is:

$$ge^{j\theta}H_Q^*(-f) - ge^{-j\theta}H_Q(f) = \frac{Y_{diode8}(f_d)}{O_{I8}^2 \cdot K} = Y3 \tag{3.59}$$

3.4.6 Quadrature demodulation of signal from Q branch

In order to estimate $H_I(f)$, the LO will also be transmitted separately on the quadrature branch. Transmit signal $x_9(t) = x_{I9}(t) + j \cdot x_{Q9}(t)$ where $x_{I9}(t) = 0$ and $x_{Q9}(t) = \sin(2\pi f_d t) + O_{Q9}$ in the second signal period $t \subseteq (3T, 4T]$. Eq. (3.18) can be rewritten as:

$$x_{rf9}(t) = -\left(O_{Q9} + \sin(2\pi f_d t)\right) * h_{Q,LP}(t) \cdot \sin(2\pi f_c t) * H_{Q,BP} \tag{3.60}$$

In the frequency domain, Eq. (3.60) can be written as:

$$\begin{aligned} X_{rf9}(f) \approx & [(\delta(f - f_c - f_d) - \delta(f - f_c + f_d)) \cdot H_{Q,LP}(f - f_c) \cdot \bar{H}_{Q,BP}(f - f_c) \\ & -(\delta(f + f_c - f_d) - \delta(f + f_c + f_d)) \cdot H_{Q,LP}(f + f_c) \cdot \bar{H}_{Q,BP}^*(-f - f_c)\,] \\ & +j \cdot O_{Q9} \cdot (\delta(f - f_c) - (\delta(f + f_c)) \\ \\ = & [\,(\delta(f - f_c - f_d) - \delta(f - f_c + f_d)) \cdot H_Q(f - f_c) \\ & -(\delta(f + f_c - f_d) - \delta(f + f_c + f_d)) \cdot H_Q^*(-f - f_c)\,] \\ & +j \cdot O_{Q9} \cdot (\delta(f - f_c) - (\delta(f + f_c)) \end{aligned} \tag{3.61}$$

According to Eq. (3.61), the output signal of the diode in the frequency domain will be:

$$\begin{aligned} Y_{diode9}(f) = &\ FFT\left\{kx_{rf9}^2(t)\right\} \\ = &\ K \cdot X_{rf9}(f) * X_{rf9}(f) \\ = &\ j \cdot K \cdot O_{Q9}^2 \cdot [\ \delta(f+f_d) \cdot \left(H_Q^*(-f) + H_Q(f)\right) \\ &- \delta(f-f_d) \cdot \left(H_Q(f) + H_Q^*(-f)\right)\ ] \\ &+ I_s(f) + I_{DC} \end{aligned} \tag{3.62}$$

where K is the overall complex gain; $I_s(f)$is the higher order intermodulation results; and $I_{DC}(t)$ is the intermodulation results at DC.

As shown in Eq. (3.62), the first two terms locate at $\pm f_d$, which indicates that the RF frequency response of I branch is shifted to baseband by the LO from the inphase branch. The last components are clearly separated from the interested tones. Hence, it is straightforward to calculate the value of $H_Q^*(-f) + H_Q(f)$ by applying FFT to the diode signal. The summation of $H_Q^*(-f) + H_Q(f)$ at the interested frequency f_d is:

$$H_Q^*(-f) + H_Q(f) = \frac{Y_{diode9}(f_d)}{jO_9^2 \cdot K} = Y4 \tag{3.63}$$

Solve Eq. (3.51), (3.55), (3.59) and (3.63) by using the previously estimated $\hat{g}$ and θ in Eq. (3.38) and (3.39). The frequency response of $H_I(f)$ and $H_Q(f)$ at $\pm f_d$ can be calculated as follows:

$$\hat{H}_I(f_d) = \frac{Y1 - Y2/\hat{g}e^{-j\hat{\theta}}}{1 + \hat{g}e^{j2\hat{\theta}}} \tag{3.64}$$

$$\hat{H}_I(-f_d) = \left(\frac{Y1 + Y2/\hat{g}e^{j\hat{\theta}}}{1 + e^{-j2\hat{\theta}}}\right)^* \tag{3.65}$$

$$\hat{H}_Q(f_d) = \frac{Y4 - Y3/\hat{g}e^{j\hat{\theta}}}{1 + e^{-j2\hat{\theta}}} \tag{3.66}$$

$$\hat{H}_Q(-f_d) = \left(\frac{Y4 + Y3/e^{-j\hat{\theta}}}{1 + e^{j2\hat{\theta}}}\right)^* \tag{3.67}$$

where $Y1 = Y_{diode6}(f_d)/\left(O_{I6}^2 \cdot g^2 \cdot K\right)$; $Y2 = Y_{diode7}(f_d)/\left(jO_7^2 \cdot K\right)$; $Y3 = Y_{diode8}(f_d)/\left(O_8^2 \cdot K\right)$; $Y4 = Y_{diode9}(f_d)/\left(jO_9^2 \cdot K\right)$

The coefficient in Eq. (3.20) and (3.21) is estimated as:

$$\hat{G}_1(f) = \hat{g}e^{j\hat{\theta}}\hat{H}_I(f) + \hat{H}_Q(f) \tag{3.68}$$

$$\hat{G}_2(f) = \hat{g}e^{j\hat{\theta}}\hat{H}_I(f) - \hat{H}_Q(f) \tag{3.69}$$

The "time division" method realizes self-IQ-demodulation and achieves imbalanced information from the I and the Q branch. According to the above equations, the overall complex gain K is still unknown. However, it is not necessarily required if the compensator is carefully designed. The design details are presented later. Recalling Eq. (3.26) the proposed method is based on the assumption that the square law device is working in ideal conditions. In the real world scenario, the 3rd and other higher order intermodulation terms produce interference. This higher order intermodulation produces rich components. It results in interference with the LO and the signal of interest, which actually jeopardizes the overall estimation performance. Hence, the simplified training signal $x(t)$ with only one tone produces the least interference and yields the most accurate estimation results. The performance of one tone and multi-tones are verified in simulation and laboratory experimental results.

The summary of the whole self-I/Q-demodulation based estimation process is shown below:

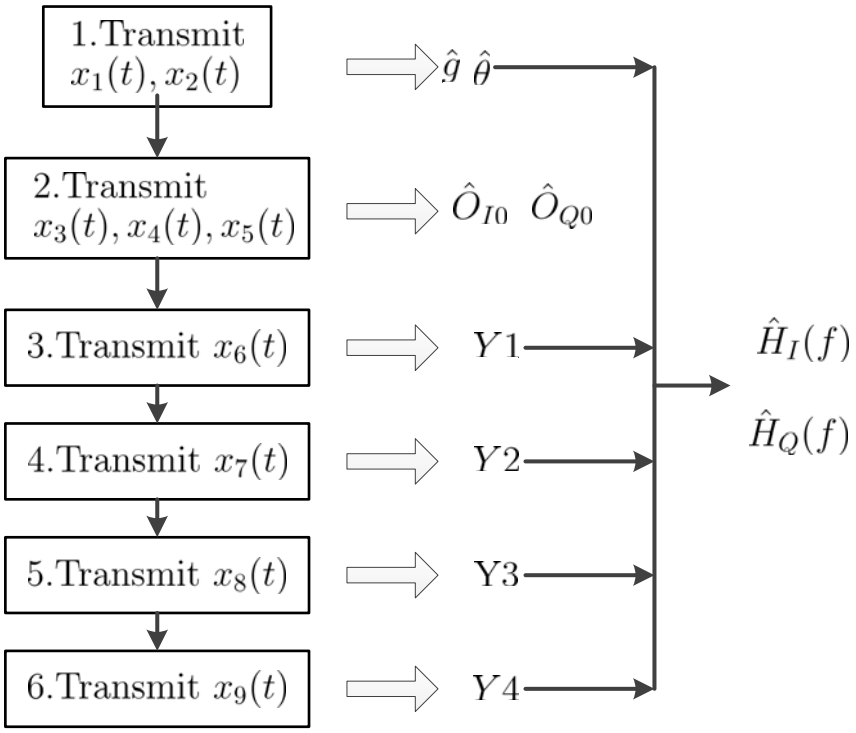

Figure 3.14 Self-I/Q-demodulation based Estimation Process

3.5 Frequency I/Q imbalance pre-distortion technique

In this section, the baseband pre-distorter will be derived. Eq. (3.27) in Section 3.3.2 gives the baseband equivalent output of the quadrature modulator:

$$X_{eq}(f) = X(f)G_1(f) + X^*(-f)G_2(f) \tag{3.70}$$

where $G_1(f)$ and $G_2(f)$ are the coefficients defined in Eq. (3.20) and (3.21). In this equation, the image term $X^*(-f)$ is caused by I/Q imbalance and is undesired which means the pre-distorter should be able to minimize the coefficients of $X^*(-f)$. Take the pre-distorter form in [86]:

$$X_p(f) = X(f) + X^*(-f) \cdot W(f) \tag{3.71}$$

where $W(f)$ denotes the pre-distorter frequency distorter. Feed this pre-distorted signal into the DCT, and the output becomes:

$$\begin{aligned} X_{eq}(f) &= X_p(f)G_1(f) + X_p^*(f)G_2(f) \\ &= X(f)\left[G_1(f) + W^*(-f)\cdot G_2(f)\right] \\ &+ X^*(-f)\left[G_1(f)\cdot W(f) + G_2(f)\right] \end{aligned} \tag{3.72}$$

In order to eliminate the image term $X^*(-f)$, the coefficients should meet the following requirement: $G_1(f)\cdot W(f) + G_2(f) = 0,\ \forall f$. Thus, the optimum pre-distorter is given by:

$$W_{opt}(f) = -\frac{G_2(f)}{G_1(f)} \tag{3.73}$$

Eq. (3.73) gives the expression of frequency domain representation of the pre-distorter. It is worth noting that the pre-distorter is the ratio between $G_2(f)$ and $G_1(f)$. Recalling the estimate of imbalanced filter in Eq. (3.64)~(3.67), the overall complex gain K will be cancelled out. Therefore, it is unnecessary to obtain the complex gain K. The pre-distorter can be directly applied to the baseband signal using the estimated $\hat{G}_1(f)$ and $\hat{G}_2(f)$, as shown in Fig. 3.15.

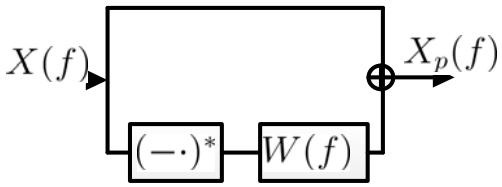

Figure 3.15 Transmitter I/Q imbalance Pre-distorter

3.6 Simulation and laboratory experiment results

3.6.1 Simulation and laboratory experiment settings

In this section, the I/Q imbalance compensation performance is investigated through computer simulation and laboratory measurements. A laboratory test platform is set up to evaluate the achievable performance, as shown in Fig. 3.16. The target compensation DCT is the Aeroflex PXI 3320/3050 arbitrary waveform

generator. Its bandwidth can be 80 MHz with a typical IRR of about -40~-35 dB. And there is an internal diode for power control, as shown in Fig. 3.16. In this experiment, this diode is used to measure the LO imbalance. As the passband of the target DCT diode is 0-2Mhz, the estimation process for the wideband I/Q imbalance parameters is emulated using the digitized RF output of PXI 3320/3050: The output RF signal is directly digitized by a Tektronix oscilloscope 6804B with 8 bit resolution at a sampling rate of 10 GSPS. The digitized RF signal is then uploaded to a PC. The PC simulates the diode process and estimates the FD I/Q imbalance using the proposed algorithm. The Aeroflex spectrum analyser is used to observe the IRR performance. Note that the LO impairments g, θ and DC offset O_{I0}, O_{Q0} is estimated using the internal diode as it meets the narrow band estimation requirements.

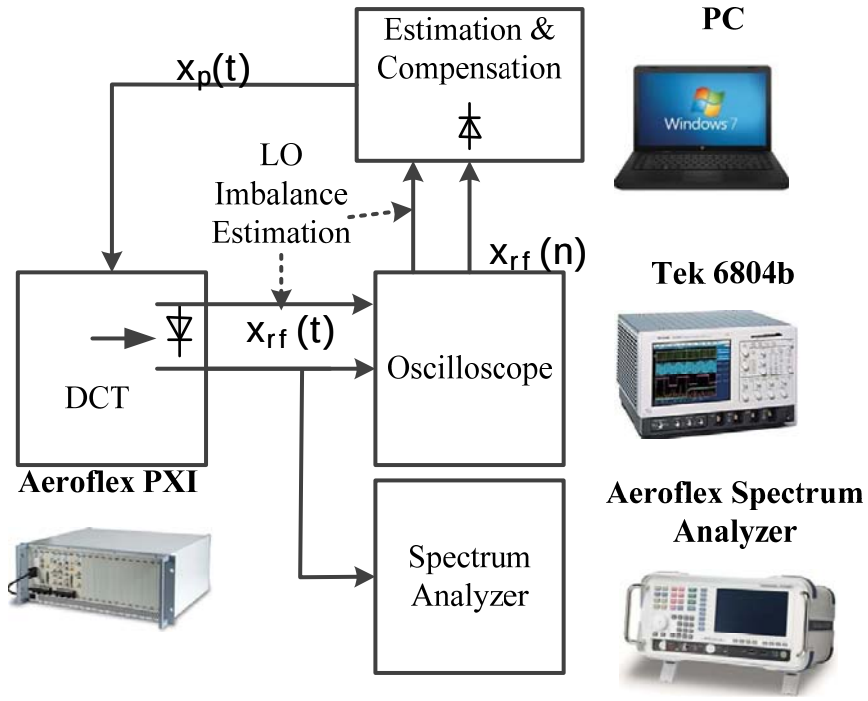

Figure 3.16 Laboratory Experiment Configuration

3.6.2 Estimation of LO impairments

The estimation performance in Section 3.4.1 is presented in Fig. 3.17 (a), (b) and Table 3.2. This step aims to estimate LO impairments g, θ and DC offset O_{I0}, O_{Q0}. Since these parameters are FI, the narrowband test tones $f_d = 20KHz$ and

$f_r = 19KHz$ are used to verify the estimation performance in Section 3.4.1. According to Fig. 3.17 (a), (b), the estimation algorithm yields nearly 80 dB IRR which proves the effectiveness of the proposed LO impairments estimation algorithm.

Table 3.2 also lists the achievable performance for different bandwidths. Carrier frequency of 2 and 4 GHz is transmitted to verify the effectiveness at different frequency band. Also, test tones with different offset frequency are transmitted to verify estimation performance at different signal bandwidth. The signal bandwidth varies from 500 to 5000 KHz, which represented that the signal varies from relatively narrow band to wideband. According to the table, the IRR decreases as the bandwidth increases from 500 to 5000 KHz, which indicates that the FD factor has a large impact as bandwidth increasesg. It also shows that achievable performance decreases as bandwidth increases, which indicates that FD impairments play a more important role in wider band scenarios. In addition, the IRR performance with the same signal bandwidth at different carrier frequency is similar, which indicates that this method is suitable for verities of carries frequency.

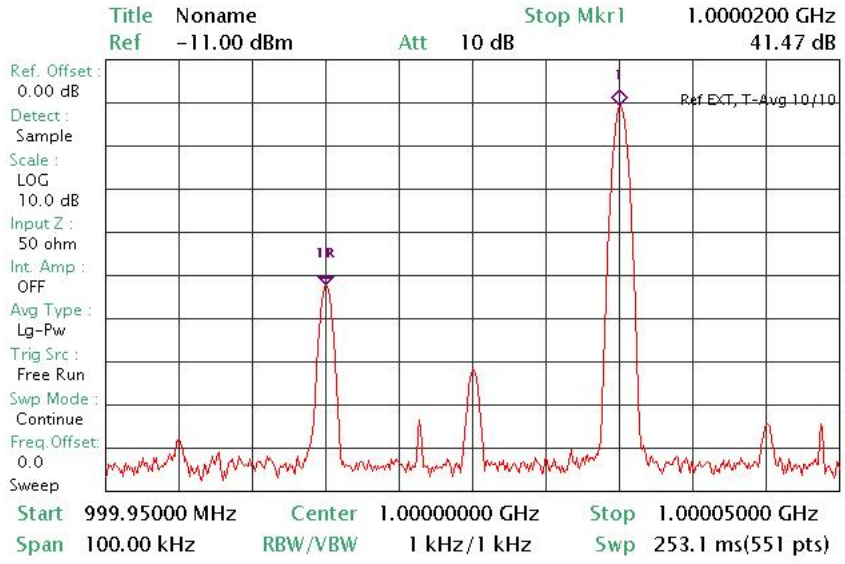

(a) 20 KHz upper band signal before FI I/Q imbalance compensation

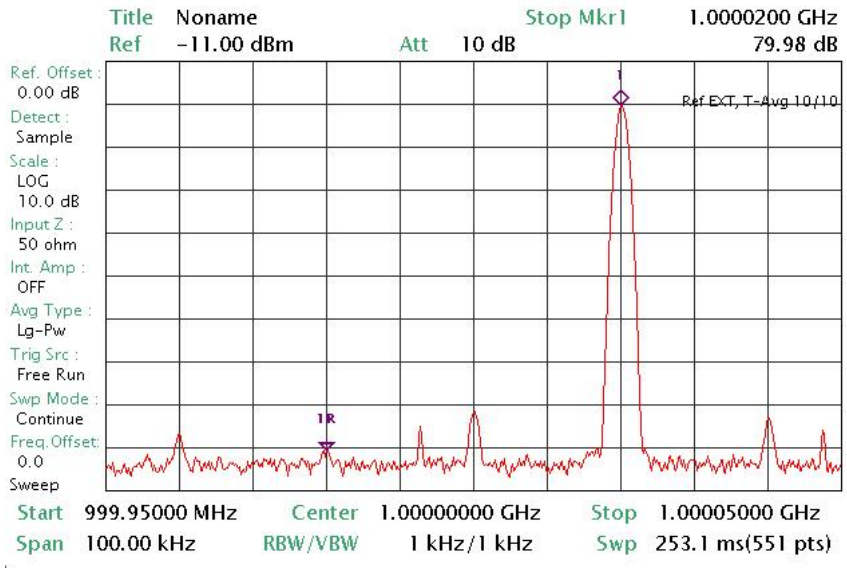

(b) 20 KHz upper band signal after FI I/Q imbalance compensation

Figure 3.17 LO Imbalance Calibration Performance

Table 3.2 Measured IRR Before and After Compensation for Different f_d and $_{LO}$ in $_{dB}$

LO(GHz) / f_d(KHz)	2		4	
	Before	After	Before	After
500	34.12	70.42	38.15	69.59
1000	33.47	64.79	38.32	67.75
5000	34.78	50.12	38.58	52.27

3.6.3 Estimation of overall I/Q imbalance

The wideband FD I/Q imbalance compensation performance is evaluated in Fig. 3.18. In order to estimate the frequency-selective effect, the location of the test tone is set to the frequency of interest $f_d = 75MHz$, which corresponds to a bandwidth of $BW = 150MHz$ for imbalanced filters.

Fig. 3.18 shows the IRR performance of the proposed method at f_d. In this experiment, the estimation results of Section 3.6.2 are utilized to compensate the demodulation errors caused by LO impairments. The directly digitized RF signal is utilized for FD parameter estimation. After the parameters are estimated, both the upper and lower band signals $x(t) = e^{j2\pi f_d t}$ and $x(t) = e^{-j2\pi f_d t}$ are generated to verify the wideband estimation and compensation performance. For upper band signal, the IRR before and after compensation are 40.91 and 54.22 dB as shown in a) and b). And the IRR before and after compensation are 43.62 and 50.38 as

shown in c) and d). It is shown that the proposed estimation algorithm gives more than 50 dB IRR on both sidebands, which indicates the overall FD I/Q imbalance in wideband is compensated well

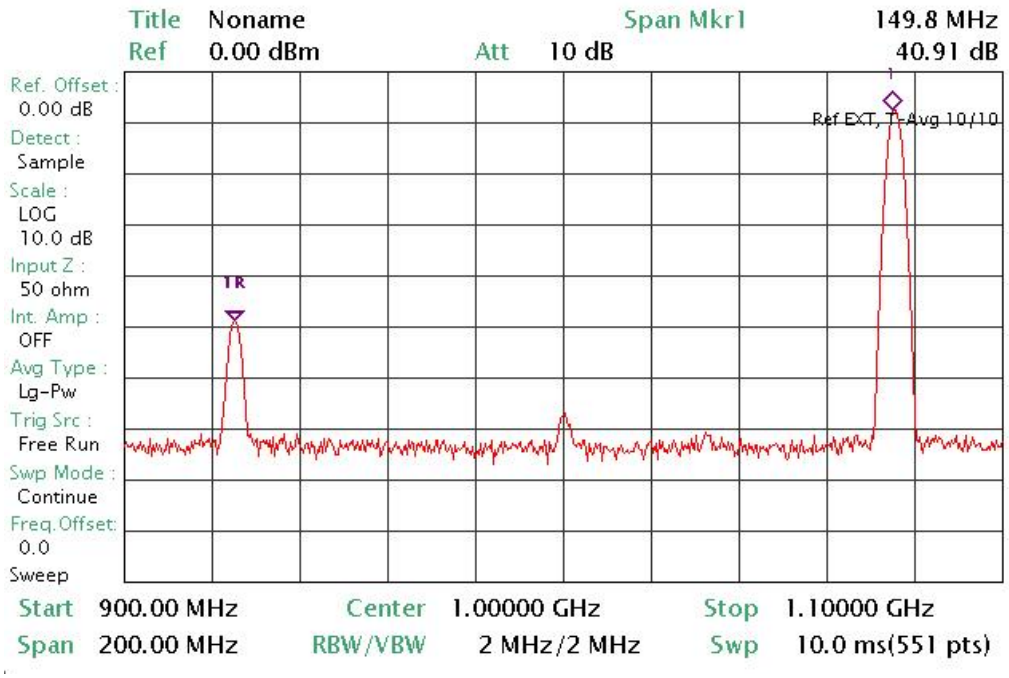

(a) Upper band signal before compensation

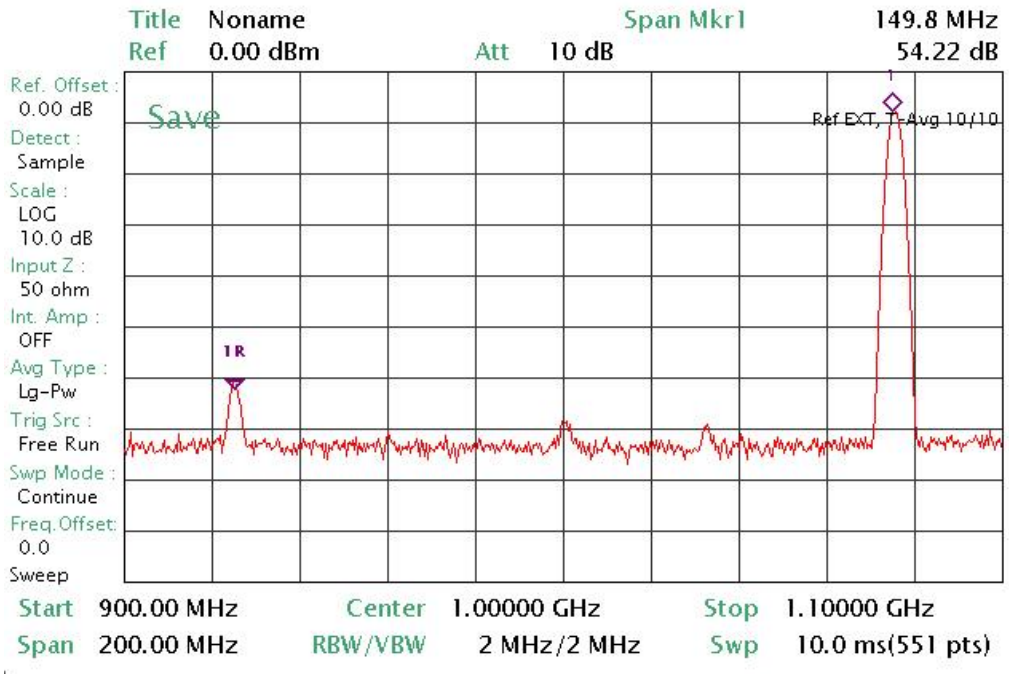

(b) Upper band signal after compensation

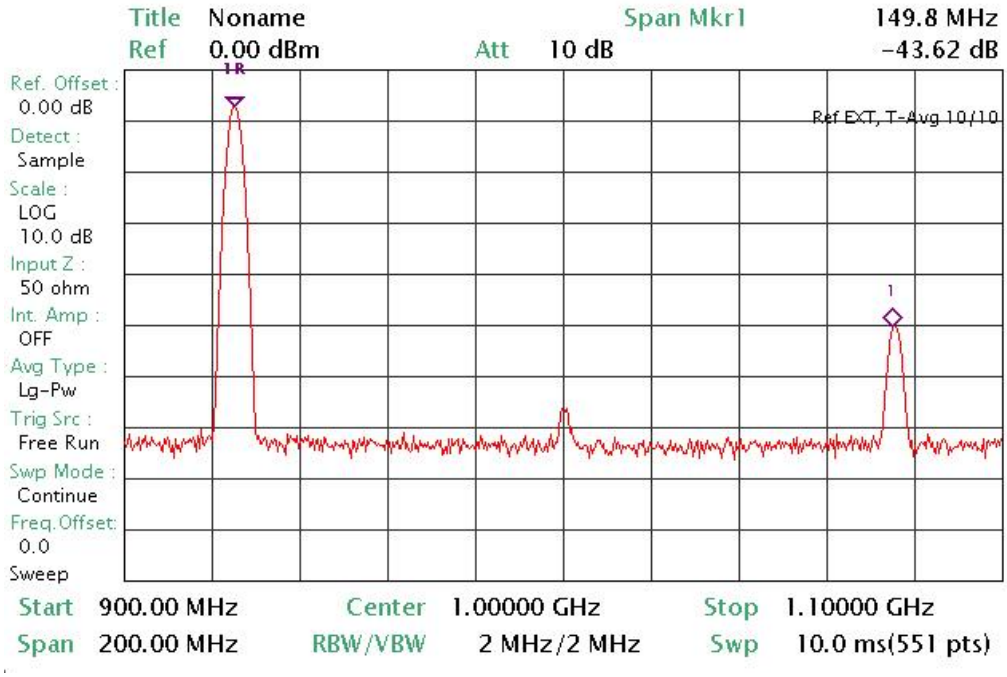

(c) Lower band signal before compensation

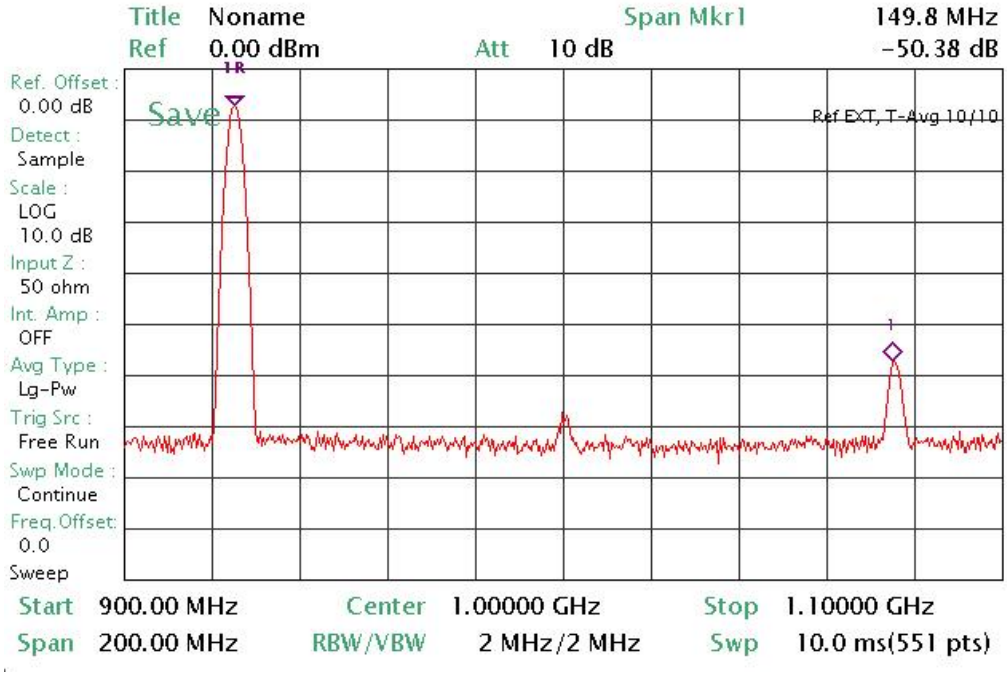

(d) Lower band signal after compensation

Figure 3.18 Calibration performance at $f_d = 75MHz$

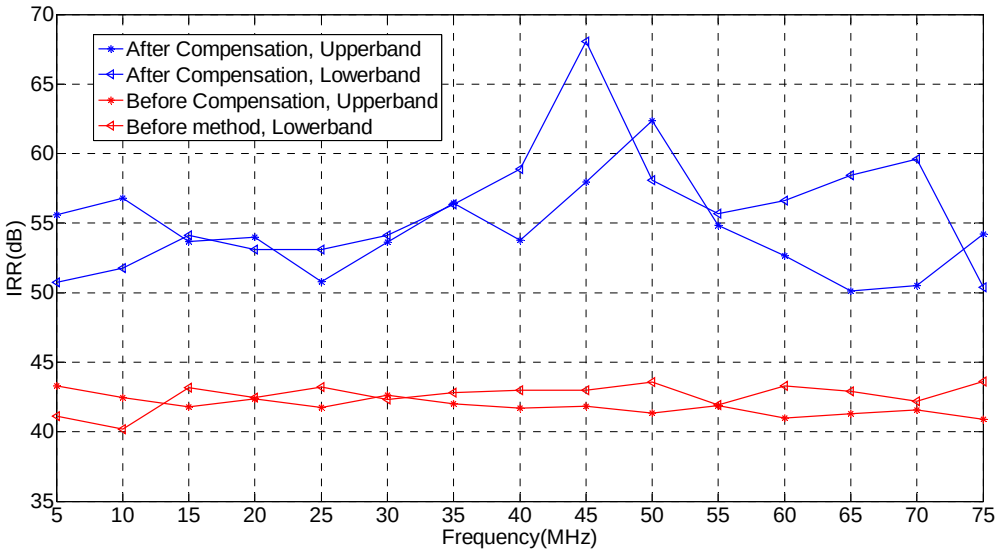

Figure 3.19 Compensation performance with f_d varies from 5 to 75 MHz

Fig. 3.19 shows the IRR performance of the proposed method within the whole signal bandwidth. In this experiment, the estimation results in Section 3.4.2 are used. In this experiment, a single tone signal $x(t) = e^{-j2\pi f_d t}$ is utilized for estimation. According to this figure, the compensation scheme gives around 10 dB IRR enhancement within $[0, 75]MHz$ bandwidth.

3.6.4 Effect of higher order intermodulation and multi-tone

The previous derivation only considers the square law of the diode, whereas there exists higher order intermodulation, especially for high transmitting power scenarios. In this section, the higher order intermodulation of the diode is also simulated. The actual signal model of the diode in [87] is adopted in this experiment:

$$\begin{aligned} s_{diode}(t) =& K_1 s_{rf}(t) + K_2 s_{rf}^2(t) \\ &+ K_3 s_{rf}^3(t) + K_4 s_{rf}^4(t) + K_5 s_{rf}^5(t) \end{aligned} \tag{3.74}$$

where the coefficients K_i is given in the Appendix A of [88]. The signal amplitude is set to 500 mV. The simulation results for square model and actual signal model are shown in Fig. 3.20. The effect of $I_s(f)$ in Eq. (3.50), (3.54), (3.58)and (3.62) is

also investigated by adding different numbers of tones at different frequency points randomly. The interested frequency is fixed to 72 MHz which is more potentially affected by the intermodulation product of lower frequency components. According to Fig. 3.20, diode higher order intermodulation brings performance degradation. In addition, the numbers of tones also severely affect performance because more tones cause larger interference. The curves vary as SNR changes, which indicates SNR is a minor influence, whereas the diode performance and intermodulation between tones can severely degrade performance.

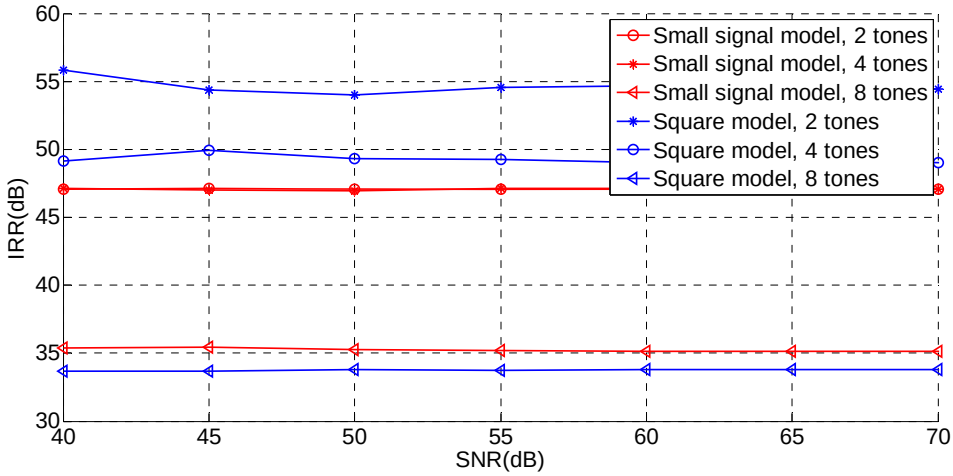

Figure 3.20 Effect of Diode Higher Order intermodulation and Different Numbers of Tones

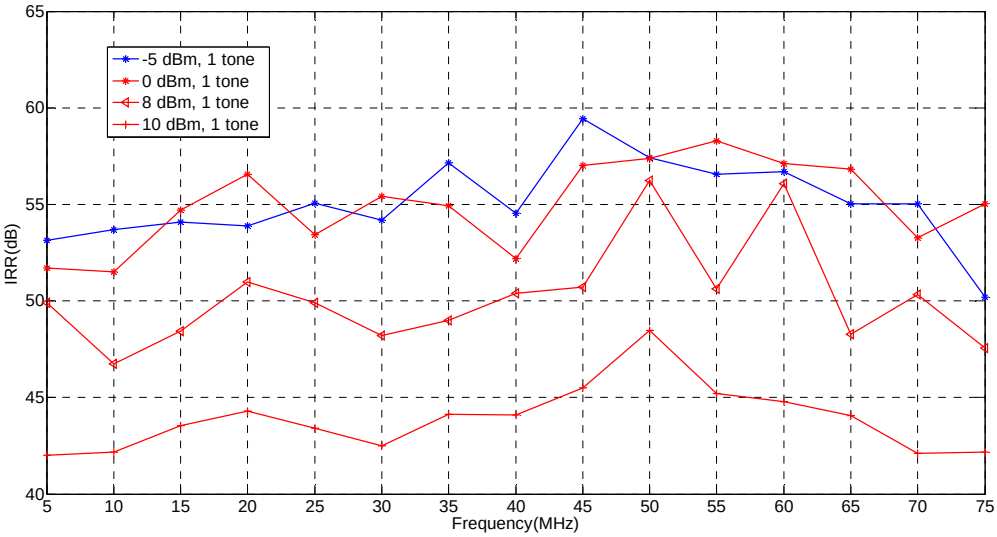

Figure 3.21 Effect of Different Transmission power

This effect of higher order intermodulation for single tone signal is also verified by laboratory measurement, as shown in Fig. 3.21. In this measurement, single tones with different frequency are transmitted. The figure shows the IRR performance when the tones are transmitted with different power. It can be shown that the IRR decreases as the transmit power increases. This is because that the amplifier produces more higher order harmonics as transmitting power increases. These harmonics overlap the tones of interest, which degrades the corresponding signal-to-noise ratio (SNR). However, the most adverse impact is that the nonlinearity produces a mass of DC components which mixes with the transmitted DC signal. And the non-linear series model for amplifier could be expressed as:

$$s_{rf,out}(t) = a_1 \cdot s_{rf}(t) + a_3 \cdot s_{rf}^3(t) + a_5 \cdot s_{rf}^5(t) + a_7 \cdot s_{rf}^7(t)$$

where $s_{rf}(t)$ is the input to amplifier; $s_{rf,out}(t)$ is the amplitude output and a_1, a_3, a_7 are non-linear coefficient, as defined in [81].

As shown in Fig. 3.21, the estimation performance suffers severe degradation when transmit power is 10 dBm, which is the maximum transmit power of the PXI 3050, and the amplifier operates in a nonlinear region.The above results is based on single tone. And multi-tone scenario is not conducted. Obviously, in multi-tone wideband scenario, the measurement could be much severe. This is because that multi-tones introduces more intermodulation products, as shown in Fig. 3.20. Hence, the proposed algorithm is more sensitive to nonlinearity of amplifier than the conventional method and requires that transmitters operate in the linear region.

According to Eq. (3.64)~(3.67), the computation complexity of the proposed algorithm is relatively low, which requires 6 FFT operations and a few multiplication and addition operations, as compared to the computation complexity of the conventional low-IF algorithm in Section 3.3.2, which requires matrix inverse operations and is $O(n^3)$. As to the cost, this proposed algorithm only requires a wideband diode and ADC, which is more cost effective than the

conventional method, which uses an external/internal modulator or even external instruments.

3.7 Conclusions

This chapter proposes a self-I/Q-demodulation based compensation scheme of FD I/Q imbalance without using external estimation instruments. Based on the existing diode-based narrow band compensation scheme, minor modification will need to be made on the internal power detection circuit to estimate FD I/Q imbalance parameters. The LO impairments g, θ and DC offset O_{I0}, O_{Q0} are estimated first. Based on these results, the estimator makes use of the LO transmitter and realizes self-I/Q- demodulation using a “time division” method. Afterwards, the FD parameters are estimated. The corresponding compensator is also presented. The performance is verified by laboratory measurements, which reveal the effectiveness of the compensation scheme. The computation complexity is relatively low and the implementation cost is low as only a wideband diode and ADC are required compared with the conventional scheme that requires an external demodulator and high speed ADCs. It should be note that this scheme is only suit for signel tone measurement. There will be limitations for multi-tones measurements due to the intermodulation and non-linear effects.

4. MMSE-DFE based OFDM Receiver Algorithm

This chapter introduces a hybrid receiver algorithm that utilizes a pilot-aided channel estimation method with a decision feedback equalizer (DFE) for OFDM systems. This receiver algorithm consists of two parts: coarse frequency offset and channel estimation, and fine frequency estimation. For the coarse estimation, a joint classical estimation algorithm including carrier frequency offset (CFO) and channel frequency response (CFR) estimation are used. With the CP of the OFDM signal and pilot tones in the frequency domain, the dominant CFO, channel effect is alleviated. The channel estimation in a mobile environment is achieved by using channel interpolation. Fine estimation presents a pilot-aided residual frequency offset estimation algorithm, which takes into account the imperfect channel estimation and Doppler effect. A DFE based on minimum mean squared error (MMSE) criteria is proposed to cope with the residual ICI and this reduces the computational burden compared with conventional MMSE-DFE. Further to this, a FPGA based co-simulation platform is developed. Simulation results indicate that the proposed hybrid receiver algorithm gives good performance.

4.1 Introduction

As a mature and well-established wireless communication technology, the Orthogonal Frequency Division Multiplex (OFDM) scheme has been adopted by LTE downlink chain. The major advantage of an OFDM system is that it makes efficient use of the spectrum by allowing overlap and is more resistant to frequency selective fading than single carrier systems. The disadvantage is that it is more sensitive to carrier frequency offset and drift. The received OFDM signal is sensitive to synchronization errors: Symbol timing offset (STO), CFO, Sample frequency offset (SFO) and Doppler shifts [39]. The STO results in phase rotation on each subcarrier, which can be tolerated to some extent with the help of CP [89].

The frequency offset destroys the orthogonality in the subcarrier which results in ICI. For example, frequency offsets of more than 4% of the subcarrier spacing can result in signal-to-interference ratio (SIR) degradation of 20 dB [90]. And this is even more severe for systems which have a large number of subcarriers, such as LTE, DVB. As described in Chapter 2, the double selective channel deteriorates the signal. The cross influences of these above factors make it difficult to estimate and compensate purely for a single factor.

Therefore, it is necessary to develop a hybrid synchronization and channel estimation algorithm to improve the error performance and channel capacity in the OFDM system. A large amount of investigations have been conducted regarding OFDM systems. CFO compensation has been studied in the works of [37, 91, 92], all of which propose both frequency and time domain estimation algorithms. The channel estimation algorithm [93, 94] introduces blind estimation approaches which form a relatively complex structure, while [95, 96] investigate data-aided channel estimation methods which exhibit good performance. Most of the algorithms on SFO estimation are based on pilot-aid methods or training sequence [97, 98]. The least mean-square (LMS) error adaptive equalization scheme is presented in [99]. Two main structures are developed: linear equalizer and nonlinear equalizer. In [63, 100], zero forcing (ZF) and MMSE criteria are introduced. In [39, 40], the author systematically analyzes the relevant nonideal transmission conditions, e.g., STO, CFO, SFO, and doubly selective channel. An equivalent signal model which contains these nonideal effects is formulated. This model shows the importance of time and frequency synchronization and acts as a good reference point for OFDM system design. In [36], a joint estimation and tracking algorithm for channel response, sampling and carrier frequency offset is proposed. The channel and frequency offset is estimated jointly and recursively by optimizing the cost function, which is computationally heavy. It is expected that a hybrid channel estimation algorithm with DFE structure will enhance error vector magnitude (EVM) performance.

The objective of this chapter is to develop synchronization and a hybrid pilot-

aided channel estimation algorithm with a decision feedback equalizer, which is easily implemented in OFDM systems. To achieve high performance, the receiver adopts a similar scheme as that proposed by [101]. To reduce the computational complexity, this algorithm makes full use of some classical algorithms and combines these algorithms with a modified DFE. Compared with the receiver in [36], this algorithm consumes less computational resource.

This receiver scheme consists of coarse and fine estimation domain. Firstly, in coarse estimation, the hybrid algorithm makes use of cyclic prefix (CP). The correlation property between CP and OFDM signal is exploited to find STO and major CFO. This process can suppress dominant ICI effects introduced by CFO and eliminate timing offset. Then, a pilot-aided channel estimation which uses channel interpolation [102] is adopted. With the existence of the Doppler effect and residual frequency offset, a modified MMSE-DFE is proposed to compensate the previously estimated parameters. This modified MMSE-DFE takes into account the residual frequency offset and imperfect channel estimation and provides comparable performance with the conventional MMSE-DFE, with a lower computational complexity [43]. With the previous classical hybrid methods, the estimation results demonstrate a relatively good performance, whilst still retaining a little rotation on the constellation. Therefore, to recover the transmitted constellation, fine estimation is essential to overcome the residual CFO, SFO and channel effect. Afterwards, a frequency domain estimation based on received signal, containing pilot tones, is carried out to suppress the SFO and residual carrier frequency offset.

In algorithm development procedure, the receiver prototype algorithm, which was developed in MATLAB does not take the reliability and hardware consumption into account. It is necessary to verify the robustness and performance in both software and hardware environments, which is known as co-simulation. There exist a number of techniques for hardware-software co-simulation. Factors including performance, timing accuracy and speed affect the choice of different co-simulation structures [103-105]. Simulation, which is created from a combined

virtual hardware environment, combined with the software, provides the fastest development process and the fastest interface between the hardware and software. However, because the software operation latency could be several μs, this could result in inaccurate timing in algorithm[103]. Hence, a co-simulation platform containing high performance FPGAs and an interface communication mechanism between the software and hardware, which can verify various wireless communication algorithms, is developed. It should be note that the aim of FPGA based co-simulation is to develop an generic platform. Hence, the main work of FPGA development will be data interface and module wrapper development The receiver algorithm implementation on FPGA will beyond the scope of this chapter.

The rest of the chapter is organized as follows: The impact of STO, CFO and SFO is described in Section 4.2. In Section 4.3, the coarse estimation algorithm is introduced. Fine estimation with DFE scheme is described in Section 4.4. Section 4.5 presents the FPGA-based co-simulation platform. Section 4.6 presents the simulation results for the hybrid channel estimation with DFE.

4.2 Impact of impairments

This section discusses the impact of STO, CFO, SFO and imperfect channels. The corresponding model will be introduced.

4.2.1 Impact of STO

The receiver is not initially aware of the starting piont of the OFDM signal. The offset of the received symbol timing leads to a biased FFT window from the original position. The FFT window could start too early or too late which corresponds with negative and positive timing error respectively, as shown in Fig. 4.1.

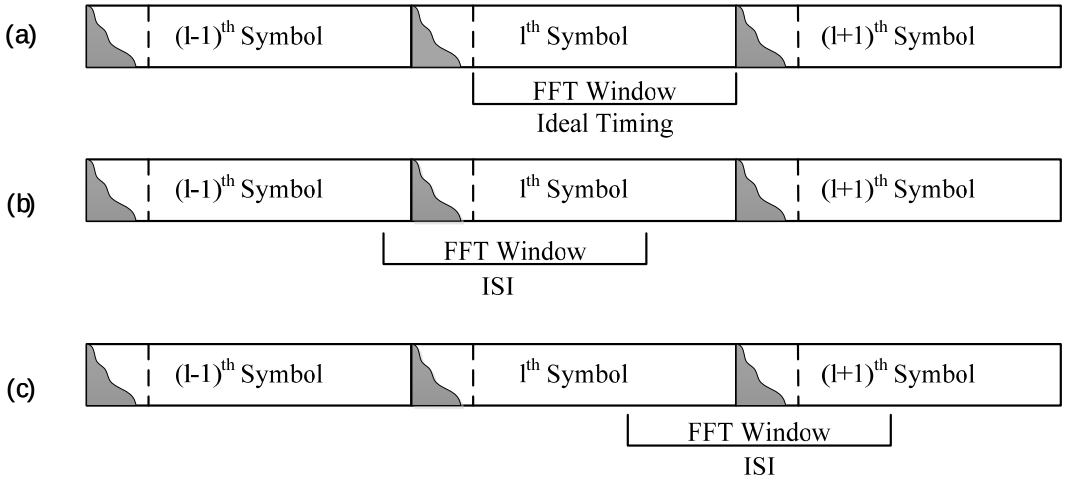

Figure 4.1 STO Impact on FFT Window

Denoting the timing error as ε, which corresponds with $n_\varepsilon = \varepsilon f_s$ sample points. The signal with timing error is described as [39]:

$$
\begin{aligned}
Y_{l,k} =& \frac{N-n_\varepsilon}{N} H_{l,k} X_{l,k} e^{j2\pi n_\varepsilon k/N} \\
&+ \underbrace{\frac{1}{N} \sum_{n=0}^{N-1-n_\varepsilon} \sum_{i=-K/2; i\neq k}^{K/2-1} H_{l,i} X_{l,i} e^{j2\pi i(n+n_\varepsilon)/N} \cdot e^{-j2\pi nk/N}}_{\text{ICI}} \\
&+ \underbrace{\frac{1}{N} \sum_{n=N-n_\varepsilon}^{N-1} \sum_{i=-K/2}^{K/2} H_{l+1,i} X_{l+1,i} e^{j2\pi i(n-N+n_\varepsilon)/N} \cdot e^{-j2\pi nk/N}}_{\text{ISI}} + n_{l,k} \\
=& \frac{N-n_\varepsilon}{N} H_{l,k} X_{l,k} e^{j2\pi n_\varepsilon k/N} + n_{\varepsilon;l,k} + n_{l,k}
\end{aligned}
\tag{4.1}
$$

where N is the FFT size; K is the number of data in one OFDM symbol; $X_{l,k}$ is the frequency domain data; $H_{l,i}$ is the channel frequency response and $n_{l,k}$ is the additive noise with power σ_n^2. According to the above equation, the timing error not only causes phase rotation in relation to the desired data symbol and ICI from other data symbols, it also results in ISI when the FFT window shifts to an extent that it incorporates the data from adjacent OFDM symbols. The ICI and ISI terms can be modelled as Gaussian noise with power [106]:

$$\sigma_{\varepsilon}^2 = \sum_i |h_i(t)|^2 \left(2\frac{\Delta\varepsilon_i}{N} - \left(\frac{\Delta\varepsilon_i}{N}\right)^2 \right) \tag{4.2}$$

where

$$\Delta\varepsilon_i = \begin{cases} n_\varepsilon - \frac{\tau_i}{T}, & n_\varepsilon T > \tau_i \\ \frac{\tau_i - T_g}{T} - n_\varepsilon, & 0 < n_\varepsilon T < -(T_g - \tau_i) \\ 0, & \text{else.} \end{cases}$$

The SNR loss caused by timing error can be expressed as [107]:

$$\gamma(n_\varepsilon) = \frac{N^2}{(N - n_\varepsilon)^2} \left[1 + \frac{\sigma_\varepsilon^2}{\sigma_n^2} \right] \tag{4.3}$$

4.2.2 Impact of CFO

The CFO problem is common in wireless communication systems, arising from the frequency difference of LO between the transmitter and receiver. Denoting the LO frequency at the receiver side is $f_c + f_\psi$, where f_ψ is the frequency offset of the carrier between transmitter and receiver LO. This shift in frequency domain results in a loss of orthogonality amongst subcarriers. The corrupted OFDM signal can be expressed as [21]:

$$Y_{l,k} = H_{l,k} X_{l,k} \frac{\sin(\pi\psi)}{N \sin(\pi\psi/N)} e^{j2\pi\psi l(N+N_g)/N} + \Psi_{l,k} + n_{l,k} \tag{4.4}$$

where $\psi = T_s \cdot f_\psi$ is the normalized carrier frequency offset by the subcarrier spacing; $\Psi_{l,k}$ is the ICI term caused by the CFO. From the above equation, the CFO mainly causes the following: phase rotation $e^{j2\pi\psi l(N+N_g)/N}$ and amplitude scaling $\frac{\sin(\pi\psi)}{N\sin(\pi\psi/N)}$ on the desired signal, and an ICI term $\Psi_{l,k}$ due to the loss of orthogonality. The phase rotation and amplitude is constant for all subcarriers. The ICI term $\Psi_{l,k}$ can be regarded as noise for the desired signal. Assuming that the signal does not suffer from deep fading, i.e $|H_{l,k}|^2 \approx 1$, and there is no sampling clock offset, the SNR loss caused by ICI can be approximeted by [107]:

$$\gamma(\psi) \approx 1 + \frac{1}{3}\mathrm{SNR} \cdot (\pi\psi)^2 \tag{4.5}$$

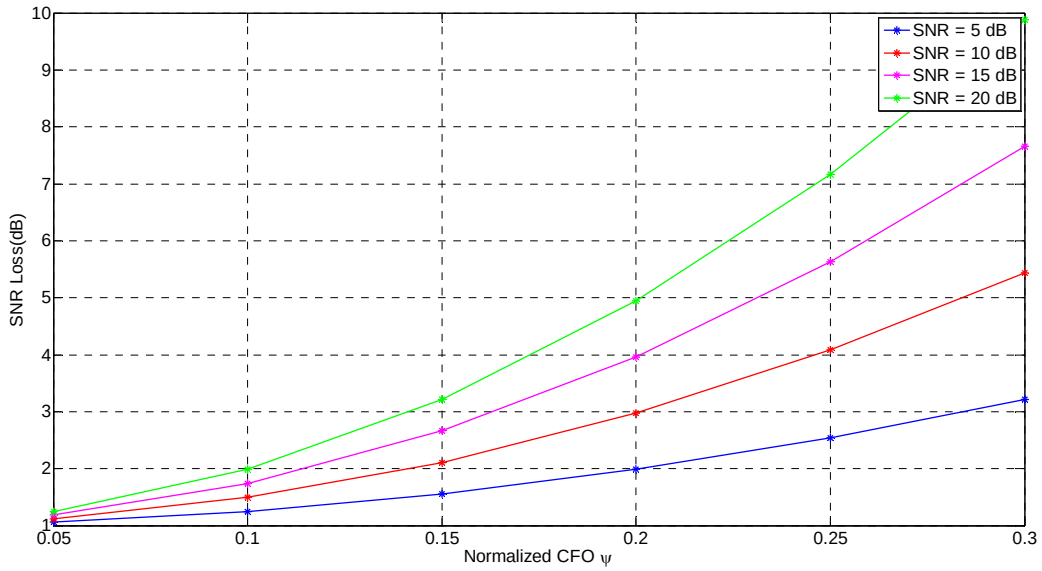

Figure 4.2 CFO Induced SNR Loss

The SNR loss caused by the CFO is depicted in Fig. 4.2. According to the figure, CFO has a significant impact on signal SNR. The SNR loss can be neglected when CFO is less than 5% of the subcarrier spacing.

4.2.3 Impact of SFO

Apart from CFO, SFO is another common impairment in a wireless communication system that results from the difference of sampling rate between transmitter and receiver. The typical SFO in wireless systems ranges from 10 to 100 ppm. Denote the sampling offset as $\zeta = (T_s' - T_s)/T_s$, where T_s and T_s' are the sampling period of transmitter and receiver respectively. The offset of the sampling period in each sample will accumulate and results in an shifted FFT window from the original postion, as shown in Fig. 4.3.

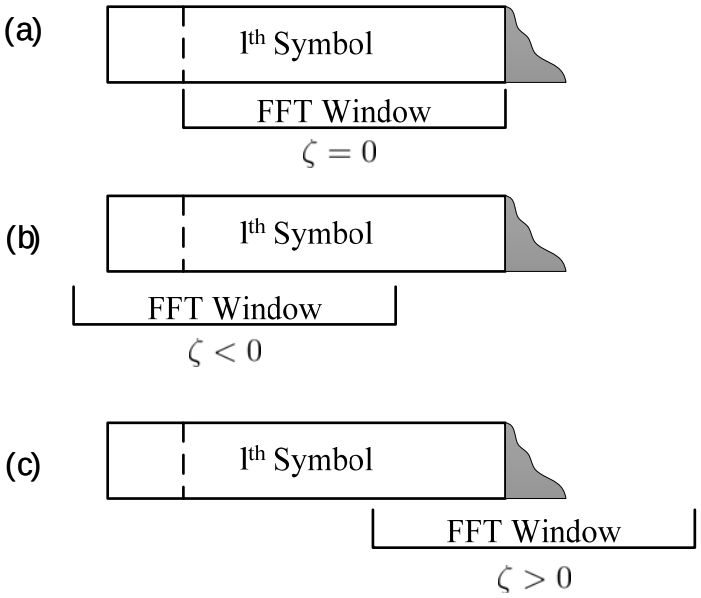

Figure 4.3 Shifted FFT Window

The received samples range within the FFT window is: $[lN_s - \zeta lN_s, (l+1)(N_s - \zeta N_s)]$, whereas the ideal FFT window is $[lN_s, (l+1)N_s]$. Hence for an LTE OFDM system with an FFT size of 2048, an SFO of up to $\pm$100 pm leads to $\pm$2 samples drift. In the frequency domain, the frequency domain data at receiver side can be expressed as:

$$\begin{aligned} Y_{l,k} =& e^{j2\pi((lN_s+N_g)/N+1/2)\cdot\zeta\cdot k}\cdot\alpha(\zeta k)H_{l,k}X_{l,k} \\ &+ \underbrace{\sum_{i;i\neq k} e^{j2\pi((lN_s+N_g)/N+1/2)\cdot((1+\zeta)i-k)}\alpha(((1+\zeta)i-k))H_{l,k}X_{l,i}}_{ICI} \\ &+ n_{l,k} \\ =& e^{j2\pi((lN_s+N_g)/N+1/2)\cdot\zeta\cdot k}\cdot\alpha(\zeta k)H_{l,k}X_{l,k} + \underbrace{n_{\zeta;l,k}}_{ICI} + n_{l,k} \end{aligned}$$

(4.6)

where $\alpha(\cdot)$ is attenuation factor. According to the above equation, the SFO will bring the following three effects: a). phase rotation $e^{j2\pi((lN_s+N_g)/N+1/2)\cdot\zeta\cdot k}$. Due to the mimatched sampling position, the position offest will bring phase rotation. b). Amplitude scaling $\alpha(\zeta k)$. Because the sampling position has an offset, the sampled amplited will be scaled. c). ICI $n_{\zeta;l,k}$. Due to the phase rotation of each carrier, ICI term will be generated.. The phase rotation exhibits a linear

relationship with the subcarriers, as shown in Fig. 4.4. Theoretically, the subcarrier symbol rotations are too small to be detected by the channel estimator [39]. Hence, a dedicated SFO tracker is required.

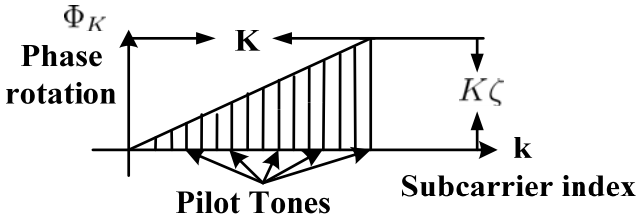

Figure 4.4 The Phase Rotation caused by SFO

4.3 Receiver algorithm

In Eq. (4.4) and (4.6), the ICI term caused by interfering data from other subcarriers can be omitted, compared with the phase rotation and attenuation on the interested subcarrier [101]. The existence of phase rotation and attenuation affects the accuracy of channel estimation [108]. Hence, coarse frequency error compensation is implemented before channel estimation. After the dominant frequency error is corrected, the channel effect will be compensated. The receiver scheme is depicted in Figure 4.5

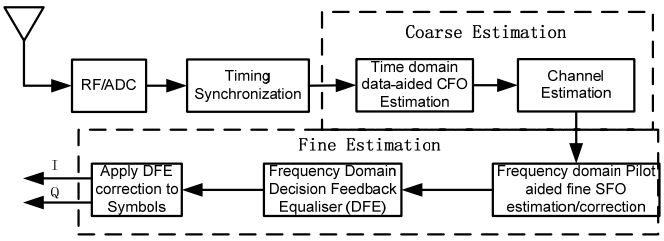

Figure 4.5 System Diagram for Hybrid Pilot-aided channel Estimation

4.3.1 Timing synchronization and coarse estimation

This section introduces timing synchronization and coarse estimation, which can preliminarily remove the time offset and frequency offset. Firstly, the timing synchronization, which is based on the synchronization signal, is carried out. Secondly, the classical hybrid estimation of CFO, SFO and CIR, based on the

continuous training sequence, is proposed in the time domain. The synchronization and coarse estimation algorithm is designed to reduce the whole complexity of the joint algorithm.

4.3.1.1. Timing synchronization and coarse CFO estimation

The estimation window must be aligned correctly with the received signal, which indicates that time offset should be estimated accurately. Relatively speaking, the delay and correlation algorithm [48] exhibit high performance and low computational complexity which is easily realized. In this algorithm, sliding windows are constructed, the cross-correlation between the received signal and a delayed version of the received signal [21].

$$\gamma(n) = |c_n|^2 = \sum_{k=n}^{n+K-1} y(k)y^*(k+D) \tag{4.7}$$

This algorithm assumes that there exists a segment of signal and a replica, with D samples delayed. The cross-correlation term c_n sharply rises when the signal is received thereby causing a quick jump of $\gamma(n)$. This indicates the start of the OFDM packet. In effect, the CP and its replica can be applied in the above equation. Coarse timing synchronization can thus be achieved. However, the above estimation algorithm yields biased output due to the existence of frequency offset. Taking the frequency offset into consideration, the estimate of timing offset is [109]:

$$\hat{n}_\varepsilon = \arg\max_n \{\gamma(n) - \rho\varepsilon(n)\} \tag{4.8}$$

where ρ is the SNR and

$$\varepsilon(n) = \sum_{k=n}^{n+K-1} |r(k)|^2 + |r(k+D)|^2$$

The coarse estimation of CFO is:

$$\hat{f}_{\psi} = -\frac{1}{2\pi}\angle\gamma(\hat{n}_{\varepsilon}) \tag{4.9}$$

In practice, the CP length is not long enough to provide a robust estimation in a low SNR scenario. Several OFDM symbols are used to achieve a more robust estimation.

4.3.1.2. Channel estimation

Because of the frequency selective and time variant property of the channel, the CIR estimation is important. In general, channel estimation can be classified into two categories: blind estimation which is carried out without knowing the channel statistics, and data-aided estimation, which makes use of some transmission signal such as the pilot or a training sequence. This data-aided estimation is more accurate. LS and MMSE algorithms are two major CIR estimation methods. The MMSE algorithm exhibits a better performance while the computational complexity is high. The LS algorithm has a much lower computational complexity and can achieve a similar level of performance with high SNR conditions [110]. In this scheme an LS method is adopted to consider complexity. Let $X_{l,k}$ represent the data on the k^{th} pilot subcarrier of the OFDM symbol in the frequency domain. After the FFT processing, the received training data can be expressed as:

$$Y_{l,k} = H_{l,k}X_{l,k} + N'_{l,k} \tag{4.10}$$

where $H_{l,k}$ is the frequency response of channel and $N'_{l,k}$ is additive noise. It is worth noting that this model incorporates the aforementioned SFO and CFO effect: the phase rotation and amplitude attenuation is modeled in $H_{l,k}$ and ICI term is modeled in $N'_{l,k}$. The aim of LS is to minimize the square error of channel estimation:

$$(Y - \hat{H}X)^H (Y - \hat{H}X) \tag{4.11}$$

which leads to the estimation of channel:

$$\hat{H}_{l,k} = \frac{Y_{l,k}}{X_{l,k}} \tag{4.12}$$

where the amplitude of training data is normalized. The noise samples are assumed to be statistically independent. According to Eq. (4.12), the channel estimation is the correlation of received signals $X_{l,k}$ and reference signal X_k^* in frequency domain, therefore the amount of computation is quite small. This CIR estimation method is also easy to implement on the FPGA or DSP hardware.

Based on the conclusion in [111], second order polynomial fitting is adopted to calculate the channel frequency response on data subcarriers in fast varying channel. Because the LS algorithm does not take into account the correlation between the channel statistics and the noise, the estimation performance will become worse with low SNR. The accurate compensation is then carried out using fine estimation.

4.3.2 Fine estimation

Though the timing synchronization and coarse estimation eliminate most of the CFO and the corruption of the channel, there may still be SFO and residual CFO, which severely affects the performance of systems.

4.3.2.1. SFO estimation

With the CFO and CIR compensated, the received signal is corrupted by the SFO. The SFO can cause a rotation on the constellation. As the SFO can cause a time deviation on every sampling point in the time domain and a phase rotation on

every sampling point in the frequency domain, some pilot tones are inserted to correct these phase rotations. A significant amount of SFO estimation algorithm is presented in [89, 112]. This pilot aided fine estimation consists of algorithms to estimate the SFO at pilot frequencies and to linearly interpolate the none-pilot tones. Moreover, with the estimated pilot phase rotations, we can calculate out the phase rotation on the data subcarriers by interpolation. According to Eq. (4.4) and (4.6):

$$Y_{l,k} = e^{j2\pi((l(N+N_g)+N_g)/N+1/2)\phi_k} \cdot \alpha(\phi_{l,k}) X_{l,k} H_{l,k} + \mathrm{ICI} + n_{l,k} \quad (4.13)$$

where $\phi_k = NTf_\varepsilon + k \cdot \zeta$.

Assuming the pilot locates on the k^{th} subcarrier; the correlation of two adjacent OFDM symbols yields the phase rotation:

$$\begin{aligned} R_{l,k} &= Y_{l,k} Y^*_{l-1,k} \\ &= e^{2\pi(N+N_g)(NTf_\varepsilon + k\cdot\zeta)} \cdot K + n'_k \\ &= e^{2\pi(N+N_g)(NTf_\varepsilon + k\cdot\zeta)+\varphi} \cdot |K| + n'_k \end{aligned} \quad (4.14)$$

where K is the component that results from the channel effect and attenuation factor. For time-invariant channel, K is a real valued number and $\varphi = 0$. For time-variant channel K can be regarded as a random complex valued number and $\mathbb{E}(\varphi) = 0$. Hence, the SFO ζ and residual CFO f_ε can be accurately calculated by averaging estimation results. According to the above equation, the phase rotation on the k^{th} subcarrier between two adjacent OFDM symbols is:

$$\begin{aligned} \theta_{l,k} &= (N+N_g)(NTf_\varepsilon + k\cdot\zeta) + \varphi \\ &= \frac{1}{2\pi}\angle R_{l,k} = \frac{1}{2\pi}\angle Y_{l,k} Y^*_{l-1,k} \end{aligned} \quad (4.15)$$

Based on this, the residual CFO is estimated by using the following algorithm on the pilot tones:

$$\hat{f}_{\varepsilon} = \sum_{k=-K}^{K} \sum_{l=0}^{L-1} \frac{R_{l,k}}{2\pi(N+N_g)\cdot NT\cdot L\cdot(2K+1)} \tag{4.16}$$

And the SFO is estimated by using the correlation on pilot tones:

$$\hat{\zeta} = \frac{1}{4K\pi} \sum_{k=-K}^{K-1} (\angle R_{l,k+1} - \angle R_{l,k}) \tag{4.17}$$

The phase rotation of the pilot tones can be estimated using the above algorithm, while the phase rotation of the data tones is achieved via interpolation. Several approaches including polynomial interpolation (linear, second and cubic) have been studied [113]. The linear interpolation has the least computational complexity among the above interpolation methods. It is worth noting that the above estimation relies on the assumption that the channel effect is a complex random process with zero mean. The computer simulation verifies this assumption. The channel effect acts as noise for the SFO and residual CFO. Furthermore, the estimation accuracy can be improved significantly by averaging more data symbols if the variation of this frequency offset is small enough in the averaging period.

4.3.2.2. MMSE-DFE

This decision feedback equalizer is developed to eliminate residual impairments. With the preceding compensation, the error performance of the received signal can be largely improved. However, there are some rotations on the constellation mainly due to the Doppler spread and residual frequency offset. These tiny rotations can be alleviated with this proposed DFE.

Two main schemes are developed for error adaptive equalization: linear equalizer and nonlinear equalizer. The linear equalizer aims to minimize mean-square error for time-dispersive additive Gaussian noise channels. However, linear equalizer performance falls over highly dispersive channels due to the limitations of

matched filter performance bound [114]. The decision feedback equalizer (DFE) which belongs to nonlinear equalization outperforms linear equalizers. Due to its reduction in implementation complexity, the DFE receiver structure has drawn considerable attention from many researchers. According to these filters' optimization criteria [44], DFE is classified into Zero Forcing (ZF) and MMSE structure. The ZF equalizer has a simpler structure which supposes the channel SNR be infinite. However, when the channel is severely frequency selective, this simplification may cause the equalizer not to show the expected functionality. In addition, the ZF criterion neglects the effect of noise, thus it is not so robust in relation to the low SNR scenario. The MMSE-DFE structure presented in this chapter adopts a new approach to minimize the mean square error (MSE) for the OFDM system channel estimation. It takes the noise into account and can enhance the performance of OFDM systems, especially when SNR is low.

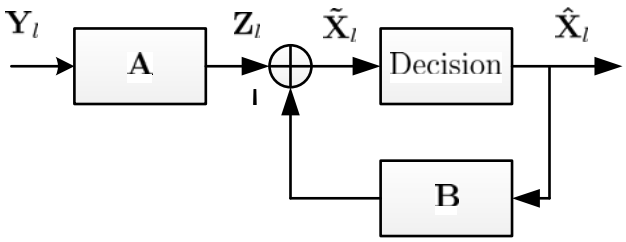

Figure 4.6 DFE Diagram

- **Conventional MMSE-DFE structure**

Plenty of research has been conducted on DFE. Serial DFE exhibits good BER performance but does not fully exploit the symbol structure [42, 44]. The MMSE-DFE [43] achieves good performance by whitening the noise and reducing the ISI. It calculates feedforward and feedback filters based on Cholesky decomposition, which is computational heavy. Other MMSE-DFEs are derived based on this research [115, 116]. This section will briefly introduce this MMSE-DFE. Based on this, a reduced complexity MMSE-DFE will be presented.

As shown in Fig. 4.6, the DFE consists of feedforward filter $\mathbf{A}$ and feedback filter $\mathbf{B}$. Define $\mathbf{Y}_l$ as the l^{th} received OFDM symbol; $\hat{\mathbf{X}}_l$ as the equalized OFDM

symbol; $\mathbf{Z}_l$ as the output symbol of feedforward filter. According to Fig. 4.6, the relationship between the above parameters is:

$$\mathbf{Z}_l = \mathbf{A}\mathbf{Y}_l = \mathbf{A}\mathbf{H}_l\mathbf{X}_l + \mathbf{A}\mathbf{N}_l \tag{4.18}$$

$$\tilde{\mathbf{X}}_l = \mathbf{Z}_l - \mathbf{B}\hat{\mathbf{X}}_l \tag{4.19}$$

$$\hat{\mathbf{X}}_l = D(\tilde{\mathbf{X}}_l) \tag{4.20}$$

where $\mathbf{N}_l$ is the noise and $D(\cdot)$ is the decision operation. Based on the above three equations, the decision error is:

$$\begin{aligned} \mathbf{e}_l &= \hat{\mathbf{X}}_l - \mathbf{X}_l \\ &= \mathbf{A}\mathbf{Y}_l - \mathbf{B}\hat{\mathbf{X}}_l - \mathbf{X}_l \end{aligned} \tag{4.21}$$

Assume the past decision is correct, or $\hat{\mathbf{X}}_l = \mathbf{X}_l$, the error can be rewritten as:

$$\mathbf{e}_l = \mathbf{A}\mathbf{Y}_l - (\mathbf{B} + \mathbf{I})\,\mathbf{X}_l \tag{4.22}$$

The MMSE-DFE should be designed so that the mean square error (MSE) $\mathbb{E}\left(|\mathbf{e}_l|^2\right)$ is minimized. Hence, the problem is to find the feedforward filter $\mathbf{A}$ and feedback filter $\mathbf{B}$ that meet the above requirement. Assuming that $\mathbf{B}$ is fixed, $\mathbf{A}$ can be obtained by minimizing $\mathbb{E}\left(|\mathbf{e}_l|^2\right)$. With the help of the orthogonality principle, it is easy to prove the error vector $\mathbf{e}_l$ should be orthogonal to $\mathbf{Y}_l$:

$$\begin{aligned} \mathbb{E}\left(\mathbf{e}_l\mathbf{Y}_l^H\right) &= \mathbf{A}\cdot\mathbb{E}\left(\mathbf{Y}_l\mathbf{Y}_l^H\right) \\ &= \mathbf{0} \end{aligned} \tag{4.23}$$

Solving this equation leads to:

$$\mathbf{A} = (\mathbf{B} + \mathbf{I})\,\mathbf{R}_{XY}\mathbf{R}_{YY}^{-1} \tag{4.24}$$

where $\mathbf{R}_{XY}$ and $\mathbf{R}_{YY}^{-1}$ is defined as:

$$\mathbf{R}_{XY} = \mathbb{E}\left(\mathbf{X}_l\mathbf{Y}_l^H\right) \tag{4.25}$$

$$\mathbf{R}_{YY} = \mathbb{E}\left(\mathbf{Y}_l \mathbf{Y}_l^H\right) \tag{4.26}$$

Based on Eq. (4.24), the feedback filter can be obtained by minimizing:

$$\begin{aligned} \mathbf{B} &= \arg\min_{B} \mathbb{E}\left(|\mathbf{e}_l|^2\right) \\ &= \arg\min_{B} tr\left\{\mathbf{R}_{ee}\right\} \\ &= \arg\min_{B} tr\left\{\mathbb{E}\left(\mathbf{e}_l \mathbf{e}_l^H\right)\right\} \\ &= \mathbf{U} - \mathbf{I} \end{aligned} \tag{4.27}$$

$\mathbf{U}$ is an upper triangular matrix with a unit diagonal which is calculated by Cholesky decomposition from the following matrix:

$$\mathbf{U}^H \mathbf{D} \mathbf{U} = \mathbf{R}_{XX}^{-1} + \mathbf{H}^H \mathbf{R}_{NN}^{-1} \mathbf{H} \tag{4.28}$$

where $\mathbf{R}_{XX}$ and $\mathbf{R}_{NN}$ is the autocorrelation matrix of transmitted signal and noise vector respectively. According to Eq. (4.27) and (4.28), this method requires matrix inversion operation and Cholesky decomposition, which is computationally heavy. For wideband systems such as LTE, the dimensions of the autocorrelation matrix could be 1024×1024. The computational burden could be extremely high and this makes implementation impossible regarding real time platforms, such as FPGA and DSPs. This dissertation aims to provide a low computational complexity MMSE-DFE solution with comparable performance.

- **Proposed MMSE-DFE**

The aforementioned method calculates $\mathbf{B}$ in a computationally inefficient way. It minimizes $tr\left\{\mathbf{R}_{ee}\right\}$ by $\mathbf{L}\mathbf{D}\mathbf{L}^H$ decomposition. Instead, the proposed MMSE-DFE obtains the smallest $tr\left\{\mathbf{R}_{ee}\right\}$ by optimizing the corresponding objective function. Recalling the MSE:

$$\begin{aligned}\mathbf{J}_{MSE} &= \mathbb{E}\left\{|\mathbf{e}_l|^2\right\} \\ &= \sum_{k=0}^{N-1} \mathbb{E}\left\{|\mathbf{e}_{l,k}|^2\right\}\end{aligned} \tag{4.29}$$

where k represents k^{th} subcarrier. The following derivation will split the aforementioned "block" calculation into subcarriers. It will show the proposed MMSE-DFE achieves a lower computational complexity. Using Eq. (4.22), Eq. (4.29) can be rewritten as:

$$\begin{aligned}\mathbf{J}_{MSE}(B_{l,k}) &= \sum_{k=0}^{N-1} \mathbb{E}\left\{|\mathbf{e}_{l,k}|^2\right\} \\ &= \sum_{k=0}^{N-1} \mathbb{E}\left\{\ |A_{l,k}Y_{l,k} - (B_{l,k}+1)\,X_{l,k}|^2\ \right\}\end{aligned} \tag{4.30}$$

Taking the expectation with respect to the data and the noise signals, the MSE is given by:

$$\begin{aligned}\mathbf{J}_{MSE}(B_{l,k}) = \sum_{k=0}^{N-1} \{\ &|A_{l,k}|^2\sigma_n^2 + |A_{l,k}H_{l,k} - 1|^2\,\sigma_x^2 \\ &+ |B_{l,k}|^2\sigma_x^2 + 2\Re\left[B_{l,k}^*\,(A_{l,k}H_{l,k} - 1)\,\sigma_x^2\right]\ \}\end{aligned} \tag{4.31}$$

where σ_n^2 and σ_x^2 represent the power of noise and transmitted signal respectively. In order to improve the performance at low SNR, the noise should be whitened at the input of the decision device [43]. Hence, some constraints will be imposed whereby the feedforward and feedback filter can whiten the noise, i.e.,

$$\sum_{k=0}^{N-1} B_{l,k} = 0 \tag{4.32}$$

The problem is to find the optimized $\mathbf{J}_{MSE}(B_{l,k})$ subject to the constraint in Eq. (4.32). This can be solved using the Lagrange multiplier method: Firstly, construct the object function:

$$
\begin{aligned}
f\left(A_{l,k}, B_{l,k}, \lambda\right) = \sum_{k=0}^{N-1} \{\ & |A_{l,k}|^2 \sigma_n^2 + \left|A_{l,k} H_{l,k} - 1\right|^2 \sigma_x^2 \\
& + |B_{l,k}|^2 \sigma_x^2 + 2\Re\left[B_{l,k}^* \left(A_{l,k} H_{l,k} - 1\right) \sigma_x^2\right] \ \} \\
& + \lambda \sum_{k=0}^{N-1} B_{l,k}
\end{aligned}
\tag{4.33}
$$

where the λ is the Lagrange multiplier. The optimized $A_{l,k}$, $B_{l,k}$, λ is obtained by setting to zero the gradient of Eq. (4.31) with respect to $A_{l,k}$, $B_{l,k}$ and λ:

$$
\begin{aligned}
\frac{\partial f\left(A_{l,k}, B_{l,k}, \lambda\right)}{\partial A_{l,k}} &= 2A_{l,k}\sigma_n^2 + 2\left(A_{l,k} H_{l,k} + 2B_{l,k} - 1\right) H_{l,k}^* \sigma_x^2 \\
&= 0
\end{aligned}
\tag{4.34}
$$

$$
\begin{aligned}
\frac{\partial f\left(A_{l,k}, B_{l,k}, \lambda\right)}{\partial B_{l,k}} &= 2B_{l,k}\sigma_x^2 + 2(A_{l,k} H_{l,k} - 1)\sigma_x^2 + \lambda \\
&= 0
\end{aligned}
\tag{4.35}
$$

$$
\frac{\partial f\left(A_{l,k}, B_{l,k}, \lambda\right)}{\partial \lambda} = \sum_{k=0}^{N-1} B_{l,k} = 0 \tag{4.36}
$$

Solving the above three equations, we obtain:

$$
A_{l,k} = \frac{H_{l,k}^* \sigma_x^2}{\sigma_n^2 + \sigma_x^2 |H_{l,k}|^2} \tag{4.37}
$$

$$
B_{l,k} = -\left(A_{l,k} H_{l,k} - \beta\right) \tag{4.38}
$$

$$
\beta = \frac{1}{N} \sum_{k=0}^{N-1} A_{l,k} H_{l,k} \tag{4.39}
$$

According to Eq. (4.37)~(4.39), the calculation of $A_{l,k}$, $B_{l,k}$, λ for one symbol requires $5N$ multiplication operations and $3N$ addition operations. Compared to the conventional MMSE-DFE, both the FF and FB filters do not require matrix inversion operation, which is easily implemented in FPGA or DSP hardware. The above equations require estimation of channel and noise. The previous section estimates channel symbol by symbol which could be used in this MMSE-DFE. Additionally, the noise power should be estimated. This dissertation proposes

another approach on noise estimation for time-variant channels and this will be presented in Chapter 5.

4.4 Co-simulation platform

After the definition of requirements of the communication system, the prototype algorithm is developed in higher level programming language, such as MATLAB. Then, the fixed-point performance and resource consumption of the developed algorithm should be verified before implemented in a real circuit. The float-pointed MATLAB code and data type will be transformed into a fixed-point hardware code, i.e. HDL, Verilog HDL etc.. Further to this, in the fixed pointed algorithm and data type will be implemented on FPGA for verification. Fig. 4.7 depicts the general design process of this co-simulation platform. As a part of receiver algorithm development procedure, the aim of this co-simulation platform is to verify the algorithm and speed up the development process.

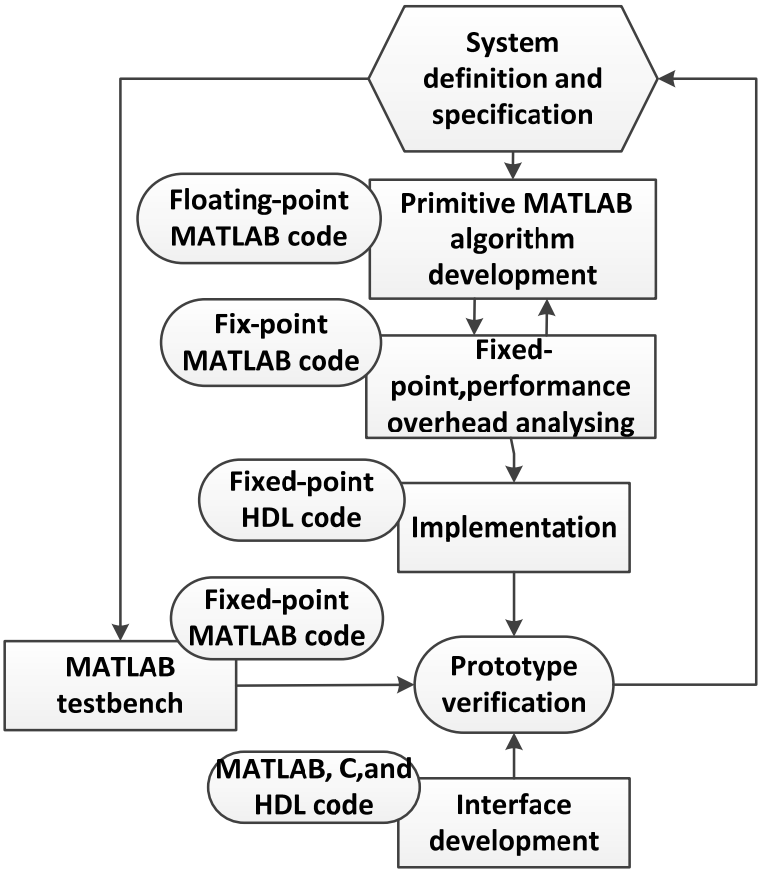

Figure 4.7 Algorithm Verification Flow

Co-simulation platforms such as WARP and OPENAIRINTERFACE [105], allow individual algorithm components to simultaneously run and exchanging information on FPGAs or DSPs and MATLAB, in a collaborative manner. With the fixed-point simulation platform, this kind of simulation process can verify feasibility and evaluate the complexity and performance of a dedicated algorithm. The existing co-simulation platforms take a considerable amount of time to convert MATLAB code to HDL code. Besides this, the hardware-software interface is another important part of the co-simulation system. Because algorithm modification may require a re-doing of the data interface, which may result in data interface development being the most time-consuming step during the whole process system algorithm verification, it is essential to reduce the workload of interface development. Considering that there already exist some tools which can automatically transform MATLAB code to HDL code, besides the implementation of a prototype algorithm, the hardware-software interface is another important part of the co-simulation system. Considering all the

substructures of the hybrid estimation algorithm, such as coarse estimation module, FFT module, CIR estimation module or the DFE module, may be verified separately, this means different types of data formats will be transmitted via the interface between the hardware and software. Thus a universal interface that is capable of various throughput and data widths is required. Therefore, the design requirements also include high speed, data transmission stability and compatibility with different data formats for the requirements of different algorithms.

To meet these requirements, a gigabit Ethernet platform is chosen as the interface between MATLAB and FPGA with the maximum data throughput of 1000 M bits/sec. Also, in order to achieve maximize throughput, the extended User Datagram Protocol (UDP) communication protocol is adopted. As described in Fig. 4.8, the pipeline UDP packet consists of two parts: the payload and header. The header contains an essential check code for the UDP packet and the payload part holds the data which is specified in the header.

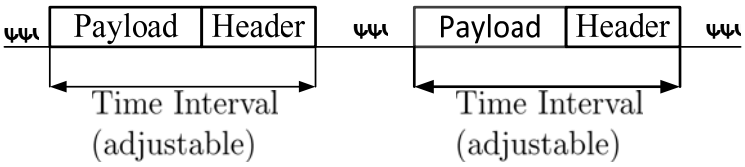

Figure 4.8 UDP Packets Transmission

The hardware part is the crucial part for the verification. It handles not only the UDP communication between FPGA and PC but also data processing. The hardware is implemented on a Xilinx ML605 board with Xilinx Virtex6 FPGA. This co-simulation platform takes advantage of the abundant on-chip resources of FPGA. The high speed and high performance Digital Clock Management, dedicated MAC Ethernet IP core, LUTs and embedded high speed DSP 48E1 Slice module work collaboratively provide a high speed universal high speed data interface and high performance algorithm realization platform. Fig. 4.9 shows the system diagram of the proposed co-simulation platform. Table 4.1 presents the entire hardware consumption, which includes consumption of universal data interface, DFE module, as well as the LTE Turbo decoder. Appendix A and B

present some other simulation results.

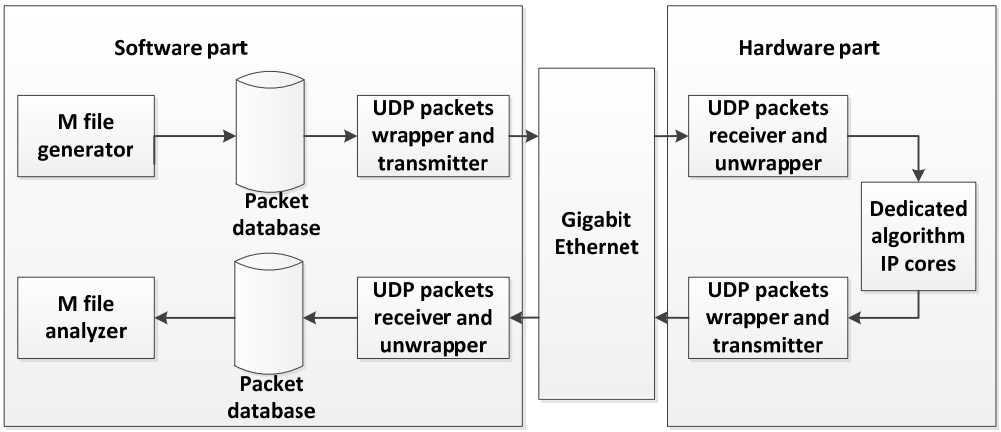

Figure 4.9 System Diagram of Co-simulation Platform

Table 4.1 Hardware Consumption of Some Important FGPA Modules

	DSP48	Slice LUTs	Block RAM
Hardware Interface	0	959	12
Resampler	30	2274	6
Turbo Decoder	16	29877	69
Overall Hardware resource	769	150720	416

The main contribution of this co-simulation is to propose a universal interface between MATLAB and FPGA and to provide a flexible verification platform. It also makes the most of the high speed gigabit Ethernet and the high performance FPGA.

4.5 Simulation results

In this section, the performance of this hybrid receiver algorithm is evaluated via computer simulations. As this hybrid algorithm is a combination of classical algorithm and DFE, the performance of different modules is partly assessed. Table 4.2 lists the details of the OFDM symbol for the simulation. One burst format of data that contains 582 data OFDM frames is used in this simulation. In the simulation, we adjust the CFO and SFO by adding an extra carrier frequency offset on the input data to simulate CFO in a real situation and using the FPGA

based resampler to tune the sampling rate of the receiver. Then, the Rayleigh fading channel is considered, with 9 taps for simulation as described in Table 4.3. Doppler effect with a different frequency shift is also considered. The channel process is simulated based on the model in Section2.3.

TABLE 4.2
OFDM Parameters

Parameter	Value
N_{SD}: number of data subcarriers	48
N_{SP}: number of pilot subcarriers	4
T_{FFT}: FFT and IFFT period	$3.2us$
T_{SIGNAL}: duration of the signal symbol	$4us(T_{CP}+T_{FFT})$
T_{CP}: CP duration	$0.8us(T_{FFT}/4)$
T_{SYM}: symbol interval	$4us(T_{CP}+T_{FFT})$
Sampling rate:	$20MHz$
Subcarrier Spacing:	$312.5KHz$
Modulation Scheme:	16 QAM

TABLE 4.3
Channel Taps in Simulation

Taps	Relative delay (ns)	Fading (dB)
1	0	-4.6
2	15	-2.0
3	25	-3.0
4	50	0
5	150	-4.3
6	225	-6.5
7	400	-3.0
8	525	-15.2
9	750	-21.7

Fig. 4.10 shows the normalized mean square error (NMSE) curves on the output of the CFO estimator under different SNR when SFO is 80 ppm. Doppler effects are not considered in this simulation. The performances of the system under different CFO are compared. The NMSE of the CFO estimation are obtained from 100 Monte Carlo trials on one SNR value and calculated for 50 OFDM symbols.

$$\mathrm{NMSE} = \frac{1}{N}\sum_{k=1}^{N}\left(\frac{\hat{f}_{\psi k} - f_{\psi}}{f_{\psi}}\right)^2$$

where f_ψ is the real CFO and $\hat{f}_{\psi k}$ is the estimated CFO of the k^{th} Monte Carlo run. During the simulations, a few carrier frequency offsets are chosen which range from 100 kHz to 300 kHz with 50 kHz step size. The SNR varies from 5 to 45 dB.

According to Fig. 4.10 the maximum NMSE is below $2*10^{-3}$ even when the situation is the worst SNR of 5 dB, which indicates that estimation is quite accurate. In addition, the NMSE for different CFOs is similar, with the largest MSE $1.4*10^{-3}$ and smallest $2.14*10^{-7}$except for the CFO = 300 kHz curve. These curves show that this CFO estimation algorithm is robust to different CFOs and SNRs. The CFO = 300 kHz curve has a higher MSE than the other CFO curves. This is because the subcarrier interval is 312.5 kHz in the adopted OFDM system. When CFO is closed to this value, the value of the subcarriers will be aliased on their adjacent subcarriers, which indicates that the CFO algorithm becomes invalid when CFO extends beyond that value. Thus, CFO = 312.5 KHz becomes a critical frequency, and the estimation for CFO = 300 kHz becomes worse. The NMSE keeps relatively low and decreases as SNR increases from 5 dB to 45 dB, which indicates that a higher SNR helps to enhance the estimation performance.

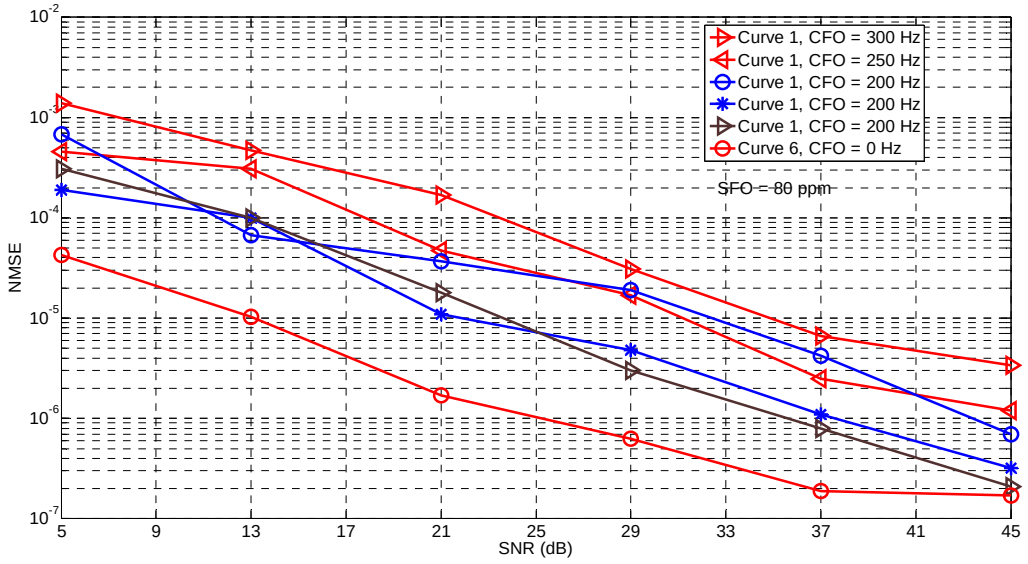

Figure 4.10 NMSE of CFO Estimation V.S. Varying SNRs for different CFOs

Fig. 4.11 shows the performance of the channel estimation. This simulation is carried out under different SNR, SFO, Doppler frequency shift scenarios. The

NMSE is calculated as depicted in previous simulations, based on the assumption of ideal CFO estimation. Maximum Doppler shifts are set to $f_d = 0Hz$ and $f_d = 20Hz$ which respectively correspond with motionless mobile receivers and a mobile receiver. In addition, two SFOs are selected to investigate the impact on CFR estimation. The NMSE curves for the two different Doppler frequencies against different SNR are plotted. Generally, the NMSE achieves good performance with NMSE constantly below 0.3185%, but a higher SNR will lead to a smaller NMSE. There is still fluctuation on the NMSE curve. This is because the square error of CFR estimation $(Y - X\hat{(H)})(Y - X\hat{(H)})^H$ in Eq. (4.11) is no longer a least square error under the condition of the Rayleigh fading channel which means the LS algorithm is not optimal for the Rayleigh fading channel.

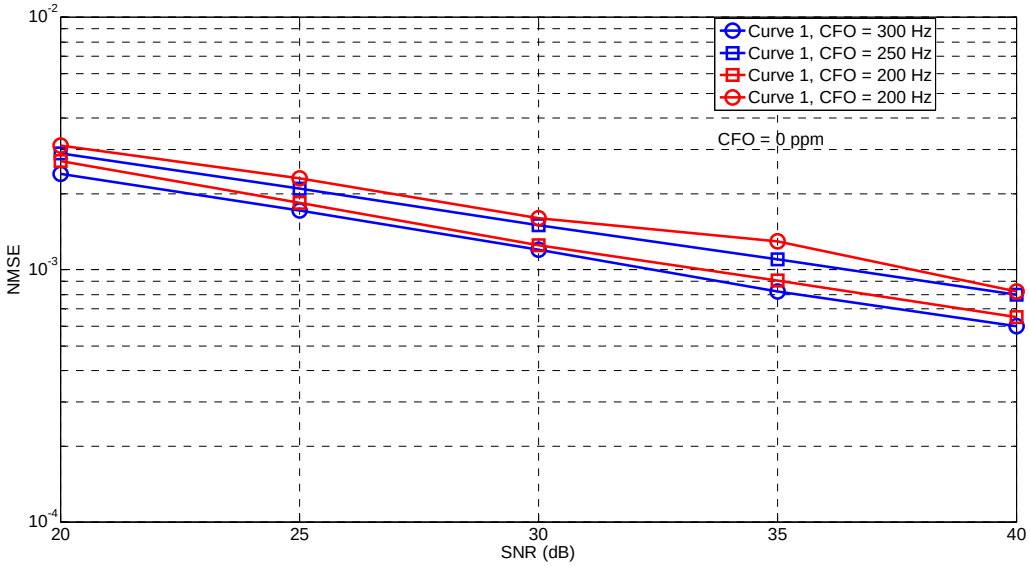

Figure 4.11 NMSE of Channel Estimation for Different SFO and Doppler Shifts

Because the preceding estimator does not compensate SFO, channel estimation is also influenced by SFO. The curves for $\mathrm{SFO} = 300\mathrm{ppm}$ are higher than that of the 50 ppm situation in terms of NMSE. As can be seen from Fig. 4.11, the channel estimation performance suffers from a slight degradation and Maximum Doppler shift changes from 0 Hz to 20 Hz. This is because Doppler spread inevitably leads to a non-constant frequency offset, which cannot be estimated by CFO estimator without the knowledge of all the subcarrier's channel information.

Fig. 4.12 shows the SFO estimation performance for different SFOs and SNRs. The error vector magnitude (EVM) data is calculated from the output signal of the SFO estimator, as depicted in Fig. 4.5. As a comparison, the EVM of the received signal before the SFO estimation is also presented. In this simulation, the CFO is still set to 0 kHz and SFO = 50 ppm and SFO = 150 ppm are chosen to obtain brief knowledge of the effects of different SFOs. As a point of reference, the ideal case with perfect frequency synchronization (SFO = CFO = 0) is also included in this simulation as Curve 1. As shown in Fig 10, Curve 3 and Curve 5 represent the EVM performance before SFO estimation, with a minimum EVM of 4% higher than SFO of estimator processed signal, which shows that SFO has a considerable impact on signal quality. Besides this, by comparing Curve 2 with Curve 3, and Curve 4 with Curve 5, we can find that the post-SFO-estimation EVM is reduced by as much as 13.3% when SNR equals 60 dB, which indicates that the SFO estimator can largely enhance the EVM performance of received signal. Though the estimator can significantly improve EVM performance, the residual SFO still has a marked effect on the EVM curve: the EVM for SFO = 150 ppm is about 0.4% higher than that of SFO = 50 ppm after the SFO estimation, when SNR is higher than 30 dB as Curve 2 and 4 depict. The EVM under lower SNR is still high and requires further compensation.

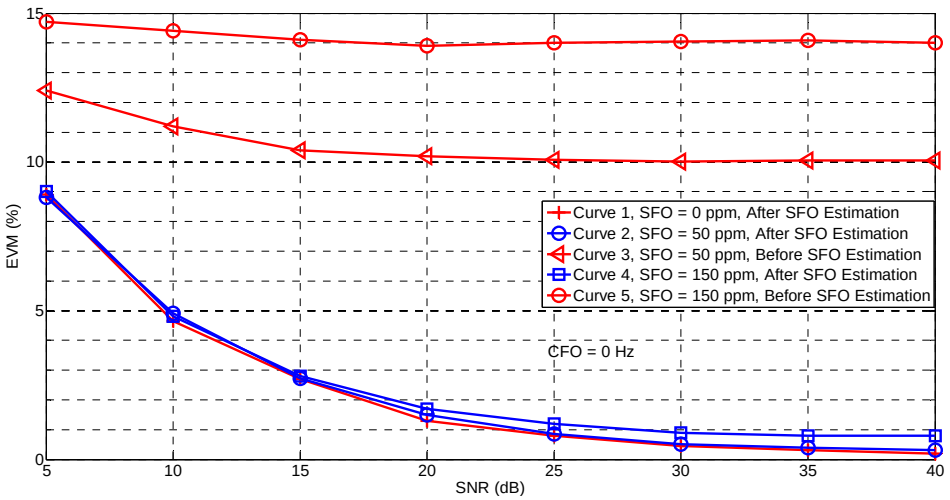

Figure 4.12 EVM Performance comparisons for SFO Estimator and Preceding Parts

Fig. 4.13 shows the EVM-versus-SNR performance curves for SFO = 0, 50, 150 ppm. This figure mainly shows the enhancement brought by DFE. The EVM data are calculated from the output signal of DFE and the pre-DFE part. The signal EVM with DFE is presented in blue curves. The signal EVM without DFE is presented in red curves. It can be seen that the DFE brings around 2 dB SNR enhancement for low SNRs. For higher SNRs, the DFE brings limited enhancement.

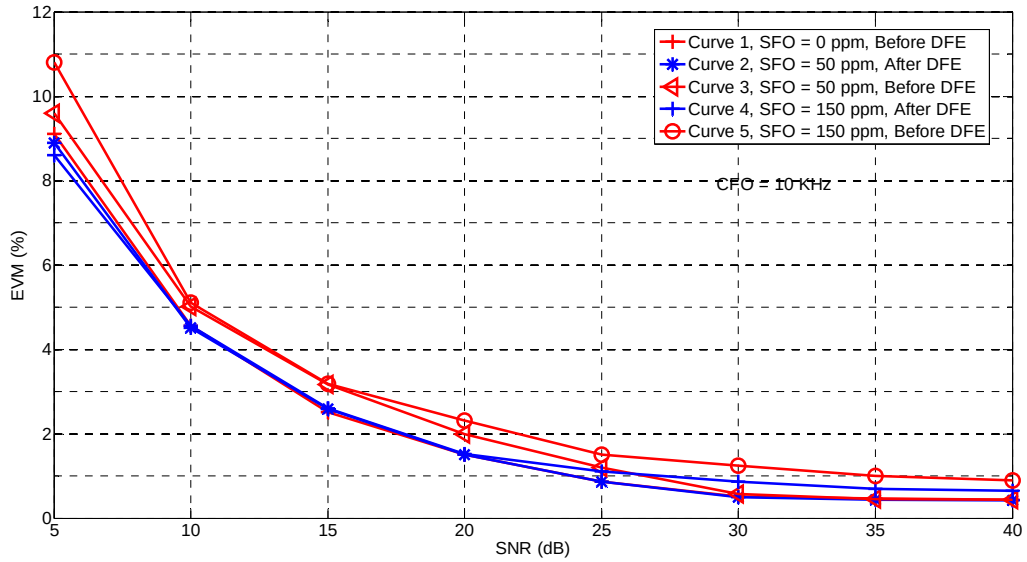

Figure 4.13 EVM Comparison between DFE and Pre-DFE Parts

Fig. 4.14 illustrates the performance comparison between proposed MMSE-DFE and conventional MMSE-DFE in [43]. This simulation uses the same experiments except that the modulation scheme is quaternary phase shift key (QPSK). During this simulation, the feedback and forward coefficients are calculated directly based on Eq. (4.37)-(4.39). As a comparison, the conventional MMSE-DFE in [78] is implemented. According to this figure, the performance of proposed and conventional MMSE-DFE yields a similar performance where the typical bit error rate (BER) is 0.01 when SNR is 10 dB. As the SNR increases, the BER of these two methods decreases.

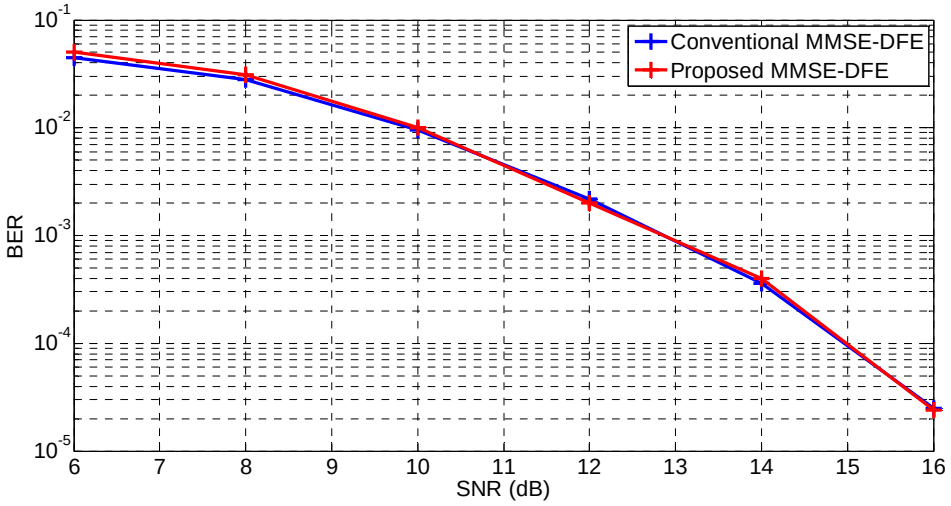

Figure 4.14 Performance of Proposed DFE and Conventional DFE

4.6 Conclusion

In this chapter, a hybrid pilot-aided OFDM receiver scheme is proposed. This estimation algorithm firstly carries out a timing domain coarse estimation to eliminate the dominant ICI by making use of CP. Furthermore, a low-complexity LS channel estimator is adopted to estimate CFR. Then, frequency domain fine estimation with pilot-aided linear interpolation is formulated which reduces the residual frequency offset. In addition, a low computational complexity MMSE-DFE scheme is introduced to enhance the EVM performance and this exhibits good performance at low SNR. A co-simulation platform is developed to speed up the algorithm verification process. The main contribution of this co-simulation is to propose a universal interface between MATLAB and FPGA which makes the most of high speed gigabit Ethernet and high performance FPGA, and to evaluate the proposed hybrid pilot-aided channel estimation for an OFDM system. With little need for consideration of data transmission and hardware limitations, the developers can concentrate on implementation, performance analysis and algorithm optimization. The simulation results based on this co-simulation platform have proven that significant EVM performance improvement can be obtained with the proposed hybrid pilot-aided channel estimation with a large range of CFO, SFO and CIR, which is effective for OFDM systems. It should be

noted that there exists some limitations for this receiver: a). The receiver algorithm copes with the Doppler effect by using MMSE-DFE. However, this DFE does not make use of features of Doppler effect. Hence, the performance could be degraded for high mobility scenarios. Further research for high mobility scenarios could be conducted. The solution could be time domain interpolation or frequency domain compensation. b). The introducing of MMSE-DFE brings higher computation complexity with little performance improvement. Hence, better solution to combat residual impairment could be proposed.

5. Subspace-based noise estimation

Signal-to-noise ratio (SNR) estimation is an important algorithm for in receivers. It provides prior knowledge for channel equalization, as described in Chapter 4. In addition, it also plays an important role in adaptive modulation in LTE system. Based on the knowledge that the received signal space consists of signal subspace and noise subspace, this chapter proposes a subspace-based SNR estimation solution to cope with the time-varying channel, with frequency selective effect and different OFDM pilot structure situations for LTE.

5.1 Introduction

The LTE adopts OFDM modulation for downlink transmission. At the receiver side, several techniques have been proposed to improve the received ODFM signal quality, including LMMSE channel estimation [117], and the previously proposed MMSE-DFE. These techniques are based on accurate Signal-to-Noise Ratio (SNR) estimation in the frequency selective fading channel. In addition, adaptive modulation and coding (AMC) are utilized to achieve high throughput in various channel conditions. The code rate and modulation scheme is adaptively changed according to the channel quality, which requires accurate SNR estimation. Hence, accurate SNR estimation is essential for receiver algorithm design.

A variety of SNR estimation methods have been investigated [45-47, 118, 119]. [118] makes use of a data-aided and decision-directed algorithm to cope with the SNR estimation problem in DVB-RCS systems. [45] utilizes zero point auto-correlation of the received signal to estimate SNR based on the assumption that the channel is constant throughout the observation period, which is not valid in practice. A few papers have investigated SNR estimation in the time variant

channel. In [46, 118], the Data-Aided (DA) maximum likelihood (ML) estimator is presented. [47] proposes a subspace-based method for an OFDM system. These algorithms give good SNR estimation performance in time-varying channel. However, they are not fully compatible with the pilot structures in LTE system. In 3GPP specification, the resource is allocated in the form of resource block (RB) in which different numbers and locations of subcarriers are allocated. The requirements for SNR estimation include:

1) The estimator can work with different pilot patterns, where the pilot number can be large or very small.

2) The estimator can cope with the time-varying channel.

In this chapter, a subspace based SNR estimator is introduced which can work with varieties of pilot patterns in a time varying channel. The advantage of this method is that the SNR can be obtained accurately in different conditions regarding pilot patterns. The chapter is organized as follows. In Section 5.2, the system model for this estimation algorithm is described. Section 5.3 presents this subspace-based SNR estimation algorithm. In Section 5.4, the simulation results and comparisons are presented. Finally, the conclusions are drawn in Section 5.5.

5.2 System model

5.2.1 Applicable pilot scenarios

LTE adopts an OFDMA scheme in which the radio resource is allocated to each user dynamically in terms of RB. Though the base station broadcasts the same reference signal pattern to all users, different users may share different radio resources. Hence, the pilot pattern within the accessible radio resource for each user is flexible. In addition, LTE also adopts AMC, in which the pilot pattern could be dynamically generated by the base station according to the subcarrier spacing, RB allocation, cyclic prefix type and slot number.

Fig. 5.1 presents a typical reference signal over two RBs. The bandwidth of each RB maps to an area of 180 KHz in frequency and 0.5 ms in duration. As can be seen from the figure, the pilot is allocated in stagger with a spacing of 2 in the frequency domain and 4 in the time domain within the two RBs. In practice, the RB allocation can be flexibly and continuously distributed in both the time and frequency domain, which indicates the pilot pattern can be sparse and uneven. Therefore, the SNR estimation must be compatible with a variety of pilot numbers and pilot patterns.

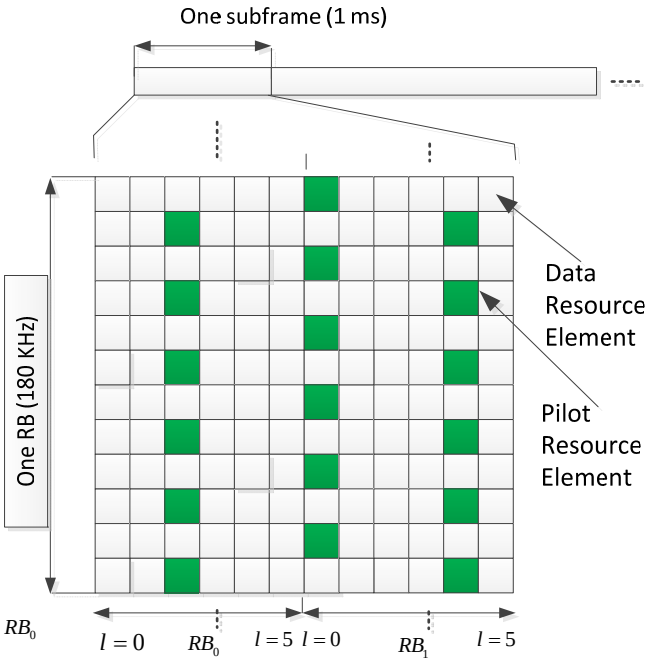

Figure 5.1 Pilot Pattern in One RB

5.3 System model

At the transmitter side, the pilot data $P_{i,k}$ at the k^{th} sub-carrier of i^{th} OFDM symbol is transferred into time domain data by IFFT and then converted to serial data. Cyclic prefix is then inserted to prevent Inter-Symbol Interference (ISI). After passing through a multipath-fading channel, the received signal after FFT can be written as (the following derivation only focuses on the symbols that

contain pilots. Hence, i in the formula refers to the i^{th} symbol that contains a pilot):

$$X_{i,k} = H_{i,k}P_{i,k} + n_{i,k} \tag{5.1}$$

where $H_{i,k}$ represents the channel frequency response at the k^{th} subcarrier of i^{th} OFDM symbol; and $n_{i,k}$ represents the AWGN noise with variance $\sigma_k = \mathbb{E}\{|n_{i,k}|^2\}$. The de-patterned signal can be expressed as:

$$Y_{i,k} = \frac{X_{i,k}}{P_{i,k}} = H_{i,k} + n_{i,k} \tag{5.2}$$

Assuming $|P_{i,k}|^2 = 1$, the noise power will not be changed by the de-patterning process. Therefore, the SNR of the received signal depends on the channel and noise power. The average SNR in this dissertation is defined as:

$$SNR = \frac{\mathbb{E}\{|H_{i,k}|^2\}}{\sigma_k^2} \tag{5.3}$$

The SNR estimation task can be decomposed into a signal power estimation problem to estimate the average channel power $\mathbb{E}\left\{|H_{i,k}|^2\right\}$ in the presence of noise; and a noise power estimation problem to estimate variance σ_k^2 in the presence of a time varying channel.

5.3.1 Conventional moving average method

The most common SNR estimation method is to use the moving average filter to filter out AWGN noise from the signal, which is adopted in WCDMA and 802.11 a/g/n systems [120, 121]. This method provides a good estimate of noise variance by averaging operations. It can also be transplanted to LTE system. The SNR estimation can be realized subcarrier-by-subcarrier.

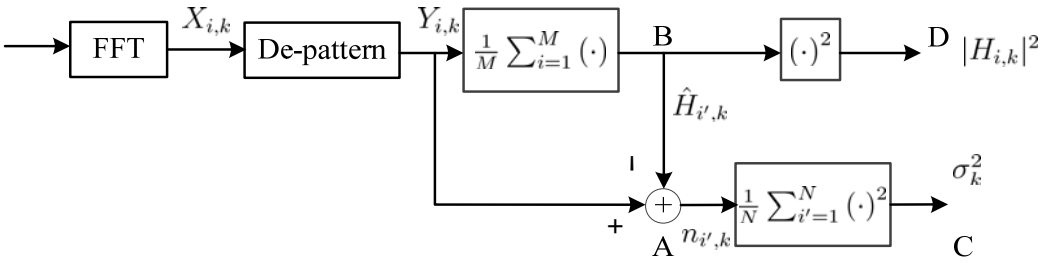

Figure 5.2 Moving Average Based SNR Estimation

Fig. 5.2 shows the SNR estimation method based on the moving average filter. Firstly, the de-patterned pilots at the k^{th} subcarrier are moving averaged over N OFDM symbols, as shown at Point B in Fig. 5.2. Under the assumption that the mean of noise is 0, the noise effect is removed from the signal component through the averaging operation. After that, the signal power is estimated by calculating the square of the signal as shown at Point D. The estimation of the signal power can be expressed as:

$$\left|\hat{H}_{i,k}\right|^2 = \frac{1}{M}\left|\sum_{l=1}^{M} Y_{i,k}\right|^2 \tag{5.4}$$

Secondly, the noise component can be estimated by subtracting the signal estimates from the de-patterned pilots, as shown at Point A. The instantaneous noise power (square of each noise sample) is averaged to estimate the mean noise power at Point C. The estimate of the noise power can be written as:

$$\sigma_k^2 = \frac{1}{N}\sum_{i'=1}^{N}\left(Y_{i',k} - \frac{1}{M}\sum_{i=1}^{M} Y_{i,k}\right)^2 \tag{5.5}$$

The moving average based SNR estimation gives good performance in AWGN channels. The larger M value gives a more accurate estimate of the signal component, which will in turn give a more accurate estimate of the noise component. However in time varying channels, the value of M should be smaller

than the coherence time of the channel and the accuracy of estimation is limited. In time varying channels, $H_{i,k}$ is a low-pass random process with a classical Jake's spectrum, and its bandwidth depends on the maximum Doppler frequency. The moving average filter does not well match the Jake's spectrum, thus the channel estimates at Point B in Fig. 5.2 cannot be very accurate. The inaccurate channel estimates in turn result in inaccurate noise estimates at Point A. The noise power will be over-estimated, resulting in underestimated SNR values as shown in Fig. 5.3.

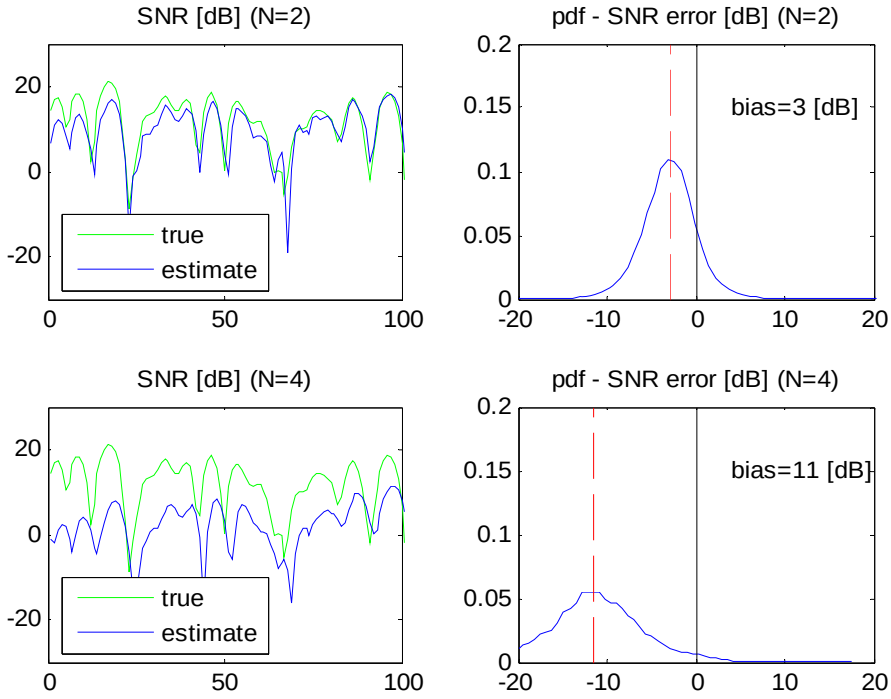

Figure 5.3 Moving Average SNR Estimation in Time Varying Fading.

In Fig. 5.3, Doppler frequency is set to 200 Hz, and noise power is -20dB. The true SNR value for one subcarrier is shown together with the estimated values. The upper two graphs are for moving average filter of Order 2, and the lower two are for Order 4. It shows that the bias of the SNR estimates go up to 11dB with a 4 tap moving average filter. Therefore, an alternative SNR estimation method is needed for fading channels.

5.3.2 Proposed subspace-based SNR estimation algorithm

Signal-spacing theorem is one of the foundations of signal processing [122]. The basic idea is to view the signal as vectors in a certain signal space, which is spanned by a set of bases. In [47], the noise power is estimated by means of decomposing the received pilot signals into a signal-space and noise space. This approach gives good performance when pilot numbers are large and assumes the pilots are evenly inserted into every OFDM symbol, whereas the number and pattern of pilots are uncertain in the LTE case. In this method, we focus on investigating the subspace based SNR estimation when pilot patterns and numbers are flexible. Fig. 5.4 shows the proposed SNR estimation procedure.

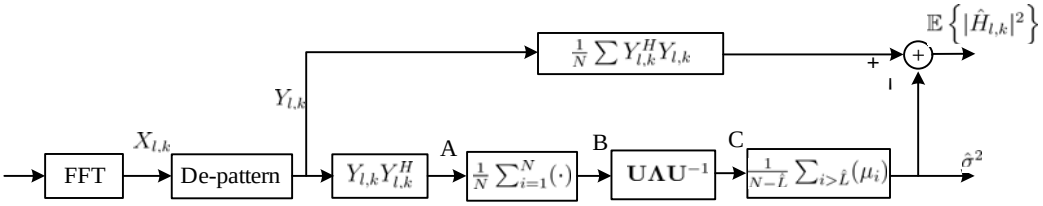

Figure 5.4 Proposed SNR estimation process

In the multipath channel, the de-patterned signal in Eq. (5.2) can be rewritten as

$$\begin{aligned} Y_{i,k} &= \frac{X_{i,k}}{P_{i,k}} \\ &= H_{i,k} + n_{i,k} \\ &= \sum_{n=0}^{L-1} h_{i,n} e^{-j\frac{2\pi k \tau_n}{N}} + n_{ik} \end{aligned} \tag{5.6}$$

where $h_{i,n}$ is the complex channel gain of the n^{th} path at i^{th} pilot-contained OFDM symbol; τ_n is the time delay of n^{th} path in terms of sample points.

Considering an observation time i, a group of pilots are received. Among them, M pilots are selected as observation vector, for example: $\mathbf{Y_i} = [Y_{ik_1}, Y_{ik_2}, Y_{ik_3}, \cdots, Y_{ik_M}]'$, where i is time index and k_M is the k_M^{th} pilot in i^{th} time index. For example, the pilot at $k_1^{th}, k_3^{th}, K_5^{th}$ subcarrier in Resource Block 0 and the pilot k_{25}^{th}, k_{30}^{th} subcarriers in Resource Block 1 are chosen as the observation vector: $\mathbf{Y_i} = [Y_{ik_1}, Y_{ik_3}, Y_{ik_5}, Y_{ik_{25}}, Y_{ik_{30}}]'$. Eq. (5.6) can be rewritten in

matrix as:

$$\mathbf{Y_i} = \mathbf{W_i}\mathbf{h_i} + \mathbf{n_i} \tag{5.7}$$

where $\mathbf{W_i}$ is a Fourier transform matrix,

$$\mathbf{W_i} = \begin{pmatrix} e^{\frac{-j2\pi k_1 \tau_0}{N}} & e^{\frac{-j2\pi k_1 \tau_1}{N}} & \cdots & e^{\frac{-j2\pi k_1 \tau_{L-1}}{N}} \\ e^{\frac{-j2\pi k_2 \tau_0}{N}} & e^{\frac{-j2\pi k_2 \tau_1}{N}} & \cdots & e^{\frac{-j2\pi k_2 \tau_{L-1}}{N}} \\ \vdots & \vdots & \ddots & \vdots \\ e^{\frac{-j2\pi k_M \tau_0}{N}} & e^{\frac{-j2\pi k_M \tau_1}{N}} & \cdots & e^{\frac{-j2\pi k_M \tau_{L-1}}{N}} \end{pmatrix}$$

and $\mathbf{h_i} = [h_{i0}, h_{i1}, h_{i2}, \cdots, h_{iL-1}]'$ is the channel impulse response at time i^{th} index and $\mathbf{n_i}$ is a $M \times 1$ vector representing AWGN noise. The following observation should also focus on the same pilot position in i^{th} time index, which guarantees all of the observation vector can be expressed by $\mathbf{W_i}$. After obtaining N settings of observation vector, the correlation matrix of $\mathbf{Y_i}$ is

$$\begin{aligned} \mathbf{R}_y &= \mathbb{E}\left\{\mathbf{Y_i}{\mathbf{Y_i}}^H\right\} \\ &= \frac{1}{N}\sum_{i=0}^{N-1} \mathbf{Y_i}{\mathbf{Y_i}}^H \\ &= \mathbf{W_i}\mathbb{E}\left\{\mathbf{h_i}{\mathbf{h_i}}^H\right\}{\mathbf{W_i}}^H + \sigma_N^2\mathbf{I} \\ &= \mathbf{\Phi} + \sigma_N^2\mathbf{I} \end{aligned} \tag{5.8}$$

where $(\cdot)^H$ denotes the conjugate transpose and $\mathbb{E}(\cdot)$ denotes the expectation operation. Because the rank of $\mathbf{W_i}$ is L and the rank of $\mathbb{E}\left\{\mathbf{h_i}\mathbf{h_i^H}\right\}$ is L, the rank of $\mathbf{\Phi}$ is L. Taking the Eigen-decomposition, the correlation matrix is

$$\mathbf{R}_y = \sum_{i=0}^{L-1} \lambda_i \zeta_\mathbf{i} {\zeta_\mathbf{i}}^H + \sigma_N^2\mathbf{I} \tag{5.9}$$

where $\zeta_\mathbf{i}$ and $\lambda_i$is the corresponding eigenvector and eigenvalue of $\mathbf{\Phi}$. Thus, the

observation signal can be viewed as consisting of a signal space spanned by an L dimension basis and an M dimension noise space. Assuming the eigenvalue of $\mathbf{R}_{\mathbf{y}}$is $\mu_1 \geq \mu_2 \geq \mu_3 \geq \cdots \geq \mu_M$, the smallest $M - L$ eigenvalues theoretically equal to σ_N^2. In practice, the difference between these eigenvalues can be very large. The noise power can only be estimated from these eigenvalues by:

$$\hat{\sigma}_N^2 = \frac{\sum_{i=L+1}^{M} \mu_i}{M - L} \tag{5.10}$$

According to Eq. (5.10), L is essential to compute the noise variance. L can be estimated by the Minimum Description Length (MDL) criterion presented in [123]. The MDL method was firstly applied to super-resolve the number of ssignal sources [123]. Further to this, this algorithm is applied to search the multipath channel components where the weak components can be ignored [124]. This criterion constructs the objective function:

$$MDL\,(k) = -\,2\lg\left(\frac{\prod_{i=k+1}^{M} \mu_i^{\frac{1}{M-k}}}{\frac{1}{M-k}\sum_{i=k+1}^{M} \mu_i}\right)^{(M-k)N} + \frac{1}{2}k\,(2M-k)\lg N \tag{5.11}$$

Then, the $\hat{L}$ can be obtained by minimizing this objective function:

$$\hat{L} = \arg\min_k MDL(k) \tag{5.12}$$

When the channel cannot be estimated accurately under severe noise conditions, the channel power approximately equals to:

$$\mathbb{E}\left\{|H_{i,k}|^2\right\} = \frac{1}{N}\sum_{i=0}^{N-1}\left(\mathbf{Y_i}^H\mathbf{Y_i} - \hat{\sigma}_N^2\right) \tag{5.13}$$

Then the SNR can be calculated as.

$$SNR = \frac{\mathbb{E}\left\{|H_{i,k}|^2\right\}}{\hat{\sigma}_k^2}$$

where $\mathbb{E}\left\{|H_{i,k}|^2\right\}$ and $\hat{\sigma}_k^2$ are obtained from Eq. (5.10) and (5.13), respectively.

- **Modified MDL method**

The classical MDL criterion in [123] estimates the path without regarding the power of each path which may lead to an overestimation ($\hat{L} > L$) in small pilot number situations. Table 5.1 demonstrates this phenomenon. The 16 pilots LTE signal is transmitted in the EVA-5 Hz channel [125], which has a channel length of 9. It can be seen that the estimated number of path $\hat{L}$ that minimizes the MDL criterion is 15, which corresponds to $k = 14$, whereas the optimum number of path $\hat{L}$ that minimizes the SNR normalized mean square error (NMSE) is 2, which corresponds to $k = 1$.

Table 5.1 Estimation Results of MDL Method

k	0	1	2	3	4	5
μ_k	319.5086	92.3797	52.4506	42.4244	29.3170	25.5680
$MDL(k)$	3269.1	2834.9	2632.4	2432.0	2317.1	2177.6
SNR NMSE	2.45	0.4485 (Minimum SNR NMSE)	3.9095	10.4341	17.5976	27.6895
k	6	7	8	9	10	11

μ	20.8666	17.8232	11.2994	9.9981	6.8162	4.4372
$MDL(k)$	2031.7	1836.6	1728.5	1551.3	1386.3	1233.2
SNR NMSE	40.7881	60.1878	78.3540	108.075	145	195
k	12	13	14	15		
μ	2.5193	1.6156	0.6958	0.0916		
$MDL(k)$	1127.9	983.2	295.4(Minimum MDL)	-		
SNR NMSE	252	361	644	-		

Note: μ_k is the k^{th} largest eigenvalue covariance matrix $\mathbf{R}_{\mathbf{y}}$.

The number of path can be very large in some channels. It is beneficial to focus on the dominant paths and ignore the weak paths for SNR estimation purposes when the pilot number is too small to estimate the noise power. This is because the channel power can be obtained via these dominant paths without much estimation error whereas the noise power estimation can be more accurate due to the fact that more eigenvalues are utilized. To achieve this, the method in [126] will be investigated. It is proposed that the eigenvalues are converted from $\{\mu_i\}$ to $(\{\mu_i\} + (max\{\mu_i\}/threshold))$. The dominant path can be obtained by adjusting the threshold. And adjusting the threshold to infinity will lead to classical MDL.

Table 5.2 Estimation Results of MDL and Modified MDL
(SNR = 20, threshold = 20)

Pilot no.	16	32	64	128	256
MDL (SNR NMSE)	1.7538	1.9943	3.6446	1.31e-5	5.05e-6
Modified MDL (SNR NMSE)	0.0017	0.0018	3.22e-4	0.225	5.47e-4

Furthermore, simulation shows that the modified MDL may lose effectiveness in some conditions and classical MDL gives better performance, as shown in Table 5.2. This is because the modified MDL method tends to reduce the number of

"channel eigenvalues" and increase the number of "noise eigenvalues". In addition, the classical MDL method can achieve an accurate channel length estimation in large pilot number situations. The power estimation of channel and noise will be accurate due to the accurate channel length estimation and utilization of large numbers of eigenvalues. In this situation, a flexible use of classical MDL method is proposed by adjusting the threshold and making a selection between conventional and modified MDL, according to the results in Table 5.2. The whole estimation procedure will be summarized in Fig. 5.5:

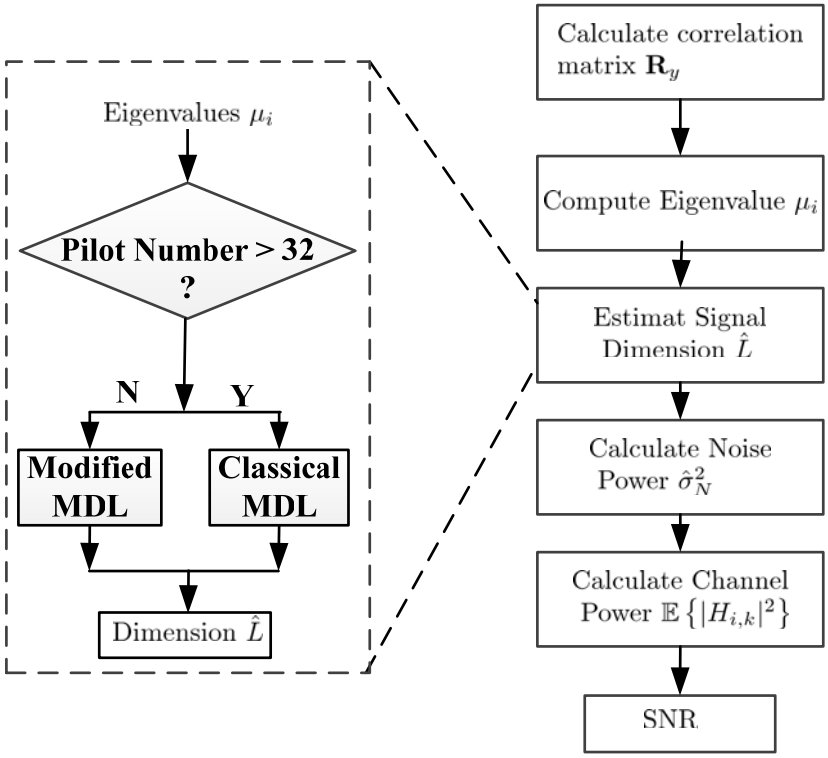

Figure 5.5 Proposed Subspace-based SNR Estimation

5.4 Simulation results

The algorithm performance is verified in both a PC and laboratory environment. The MATLAB based simulation platform provides the LTE downlink physical layer protocol in which the reference signal and user RBs can be configured flexibly. The laboratory environment consists of a fading channel emulator and Aeroflex PXI modules. The fading channel emulator can provide a real time Over-the-Air (OTA) wireless fading channel environment. The PXI modules in the

simulation consist of a PXI 3020 function generator and 3030 digitizer. which can provide a real AWGN channel with a wide range of SNR. In the laboratory verification process, the PXI 3020 generates LTE downlink signal which is controlled by the PXI panel on the PC. Afterwards, the RF signal is fed to the PXI 3020 digitizer with/without a channel emulator in the RF chain, to simulate the fading channel and pure AWGN. The digitized signal is then analyzed using MATLAB. The laboratory test bench is configured, as shown in Fig. 5.6. The time varying channel is EVA and ETU, with different Doppler frequencies as specified in [125]. In addition, LTE reference signals are also generated with different pilot patterns and pilot numbers to verify this estimator. The simulations for both the classical MDL method and proposed method are thus conducted. Table 5.3 shows the main simulation parameters.

Table 5.3 Important Simulation Parameters

Parameter Name	Parameter Range
Sampling Rate	30.72 MHz
Signal Bandwidth	20 MHz
Subcarrier Spacing	7.5 KHz, 15 KHz
Pilot Spacing in Frequency	2 or 4 subcarriers
Pilot Spacing in Time	4 OFDM symbols
Channel Conditions	AWGN, EVA, ETU[125]
Doppler Frequency	5 Hz, 70 Hz, 300 Hz

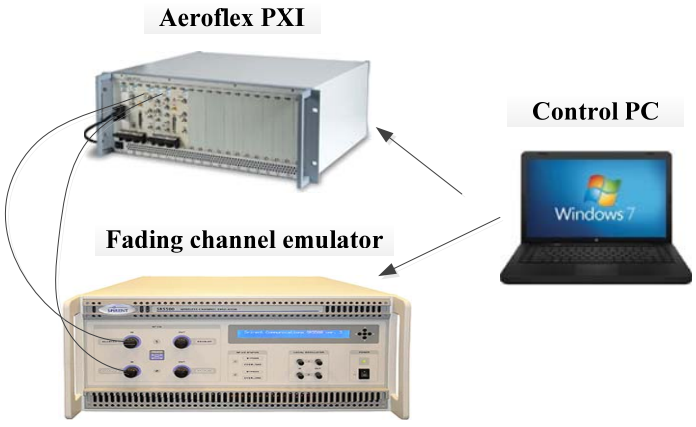

Figure 5.6 Laboratory Testbench Configuration

Fig. 5.7 shows the normalized mean square error (NMSE) of estimated SNR using

the proposed method in the EVA and ETU channels, with 5 Hz and 70 Hz Doppler frequencies. This simulation is conducted in MATLAB, which utilizes an LTE signal consisting of 256 pilot subcarriers and 256 data subcarriers. These pilot subcarriers and data subcarriers are uniformly distributed in 22 RBs, with subcarrier spacing of $7.5KHz$. It is demonstrated that the estimation gives the worst error of 1% NMSE at SNR of 2 dB in different fading channels. For higher SNR scenarios, the proposed estimation method yields good performance.

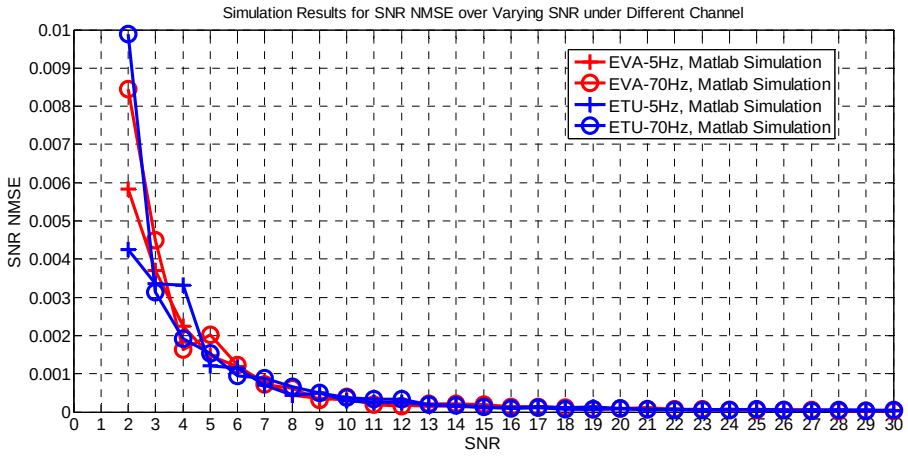

Figure 5.7 SNR NMSE v.s. SNR for Different Channels

The simulation is also carried out using Aeroflex PXI modules. The PXI 3020 is an arbitrary waveform generator which can operate from 100 MHz to 6 GHz. The 20 MHz bandwidth reference signal is first generated on MATLAB with the baseband signal filtered via the EVA-300 Hz channel. In order to emulate the downlink transmission in the AGWN channel, the deteriorated signal is then fed into the PXI 3030 directly. The RF signal power is tuned to simulate different SNR scenarios. The RF output is then captured by the PXI 3030 digitizer and analyzed in MATLAB. Fig. 5.8 shows the estimation performance. It can be shown that the proposed algorithm yields a maximum error of 9% at 5 dB SNR when 16 pilots are used. As actual SNR increases, the estimation results become more accurate. The results are reliable when actual SNR is higher than 20 dB. Another finding is that the estimation is more accurate when larger numbers of pilots are used. This is because larger numbers result in a higher dimension correlation matrix. Hence more eigenvalues are averaged to estimate the SNR. It

can also be seen that the estimation results of 16 and 32 pilots achieve accurate estimation performance, which verifies the modified MDL method.

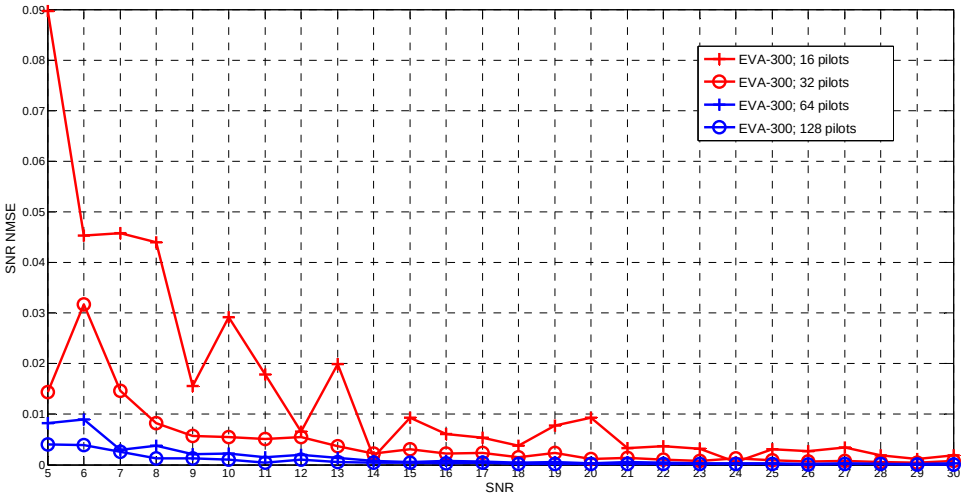

Figure 5.8 SNR Estimation Result with Different Pilot in PXI Modules

The estimation performance in the fading channel is verified with the help of the fading channel emulator, as shown in Fig. 5.6. In this emulation, the PXI 3020 generates a 20MHz bandwidth RF signal. Then, the RF signal passes through the channel emulator. Afterwards, the deteriorated signal is captured by the PXI 3030. The pilot that are distributed in the whole bandwidth and modified MDL is adopted, which means only the MDL method is used to estimate the channel components. Fig. 5.9 shows the estimation results. It can be seen that the proposed SNR estimation achieved accurate results with minimum SNR estimation error.

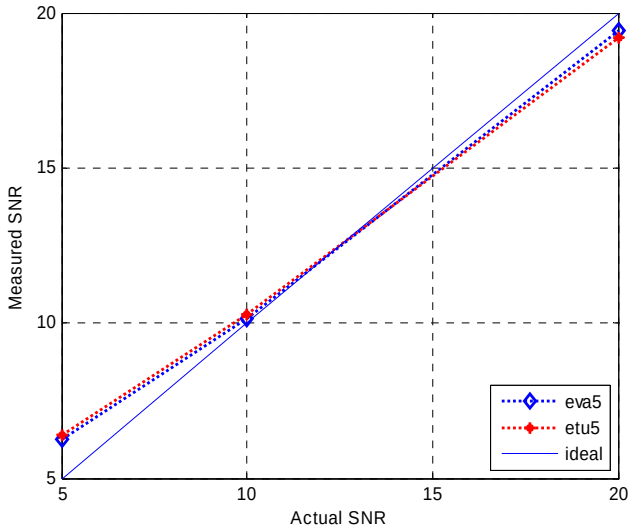

Figure 5.9 Emulation Results for Subspace-based Noise Variance Estimation

Fig. 5.10 compares the performance of different estimation methods under an EVA-5 Hz channel in a MATLAB simulation. The conventional moving average filter method is also simulated, as shown in green curves. In this simulation, we adopted 3 different numbers of pilots, namely, 16, 64 and 256. This configuration of number of pilots aims to verify the robustness of the 3 algorithms when different pilot pattern are used. The performance of classical MDL method is shown in red curves. The performance of proposed method is shown in blue curves. It can be seen that the classical MDL method gives large bias when numbers of pilot is small. According to the green curves, the moving average method gives biased results when SNR is high, The proposed method keeps good linearity for small numbers of pilots over the whole SNR range. For larger numbers of pilots, namely 256, the proposed method gives 9 dB estimation error, which indicates that it is better to use less numbers of pilot.

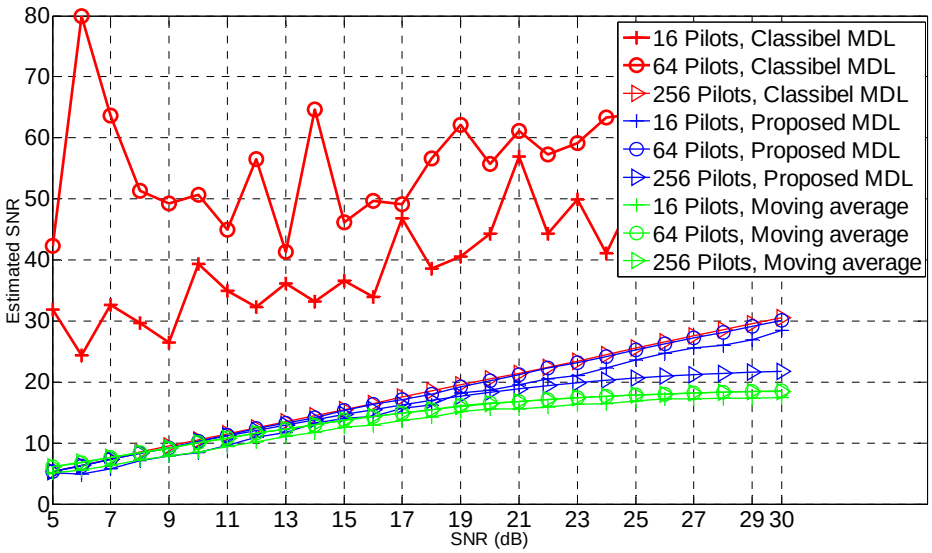

Figure 5.10 Comparison of Different SNR Estimation Methods

5.5 Conclusion

This chapter presents an SNR estimation approach that is suitable for the different pilot patterns and numbers in LTE systems. This approach is based on sub-space decomposition. Unlike the conventional moving average based SNR estimation methods, this estimator utilizes distributed pilots in different RBs and adaptively adjusts the estimation method according to the pilot numbers. Simulation on PC and Aeroflex PXI modules shows the estimator gives an accurate SNR estimation performance in a time varying channel. However, there exists some estimation error when larger numbers of pilot is used for estimation for SNRs. It is recommended that less numbers of pilot to be used. This approach can be implemented in the other services in LTE, TD-LTS, LTE-Advanced systems, where pilots data are adopted. As the complexity of eigen-decomposition is relatively high when L is large, future study will focus on reducing the complexity by methods such as eigenvalues tracking, or smallest eigenvalue evaluation.

6. Robust CRS interference cancellation

Heterogeneous networks are introduced in LTE Release 10+ to improve the link performance. The architecture introduces co-existence of Macro and Pico cell which can alleviate the potential traffic congestion caused by increased user density. Along with the co-existence of different cells comes the disadvantage of inter-cell interference. Although almost blank subframe (ABS) is proposed to mitigate the interference, the reference signal in ABS still inevitably causes interference. This chapter focuses on the interference cancellation by utilizing the information in the ABS. First, the interfering signal model which takes account of the channel effect, time and frequency error is presented. Based on this model, an interference cancellation scheme is studied. The timing and carrier frequency offset of the interfering signal is compensated. Afterwards, the reference signal of interfering cell is generated locally and channel response is estimated by making use of channel statistics. Then, the interfering signal is reconstructed based on the previous estimate of channel, timing and carrier frequency offset. The interference is then mitigated by subtracting the estimate of interference signal and LLR puncturing. Computer simulation results show that the proposed interference cancellation algorithm significantly improves the performance in different channel conditions.

6.1 Introduction

Heterogeneous network (HetNet) with macro and pico cell is introduced to meet the huge traffic demand and to extend the coverage. In this network topology, the high power (1~40 W) macro cell provides basic coverage and the low power (250 mW) pico cell serves as a complementary cell. The pico cell can functionally extend network coverage and off-load data traffic of macro-cell, which reduces

cost and increase frequency efficiency. It provides flexibility for end users to deploy pico cells by themselves. In such a case, only closed UE group (CSG) UE can access the pico cell while non-CSG UEs are not allowed to access eve they are within the coverage of a pico cell. Hence, the not CSG will suffer interference from pico cell. Apart from this, the UEs served by pico cell will also receive RF signal from neighboring high power macro cells. Thus, the end users suffer not only signal decay but also severe interference transmissions of neighboring cells. This is a common problem when the pico cell works to off-load the data traffic of neighboring macro cells. This issue is even servere when users of the pico cell stay within the coverage of macro cells with range extension enabled [127].

In Release 10, Enhanced inter-cell interference coordination (eICIC) is introduced to address this issue. eICIC proposes two techniques. First, the signal strength is biased to pico-cell which reduces the interference power. However, this is not realistic because the broadcast users cannot provide the essential channel information to the network when it adopts unidirectional link. Second, macro cell remains silent for certain periods, termed almost blank subframe (ABS) [128]. During the ABS, the physical downlink shared channel (PDSCH) is empty [127]. Hence, UE will not receive PDSCH during ABS period and the inter-cell interference can be alleviated. However, the users can still receive cell specific reference signal (CRS), paging channel (PCH), physical broadcast channel (PBCH), and synchronization channels (PSS/SSS) which degrades the performance. Hence, the further eICIC (FeICIC) is proposed in Release 11 to eliminate this CRS interference problem.

The neighbor cell (NC) CRS interference can be divided into colliding and non-colliding scenarios. In colliding CRS scenario, the NC CRS overlap the serving cell (SC) CRS. In non-colliding CRS scenario, the NC CRS interferes the data/control REs. A few researches on CRS interference mitigation were conducted. In [52, 53], Hard/soft log-likelihood radio (LLR) puncturing method is proposed for non-colliding CRS scenario. The direct CRS interference cancellation is studied in [54, 55], where the colliding interfering CRS channel is

estimated directly. However, these methods assume the interfering CRS aligns with the serving RE in time and frequency domain. In practice, the timing and frequency offset introduces estimation error which significantly degrade the performance.

In this contribution, CRS interference cancellation algorithm which makes use of channel statistics is investigated. First, the interfering signal is analyzed and modeled. Further, the interference cancellation algorithm is discussed based on this model. The algorithm makes uses of primary synchronization signal (PSS) and secondary synchronization signal (SSS) to obtain timing offset (TO) and carrier frequency offset (CFO). Then, the channel response is estimated by utilizing channel statistics. Afterwards, the interference signal is reconstructed. Then, interference is alleviated by subtracting interfering signal from received signal and LLR puncturing.

The rest of this chapter is organized as follows: The interference is analyzed and modeled in Section 6.2. Section 6.3 discusses interference cancellation algorithms. The computer simulation is presented in Section 6.4 and Section 6.5 gives the summary.

6.2 Interference analysis and model

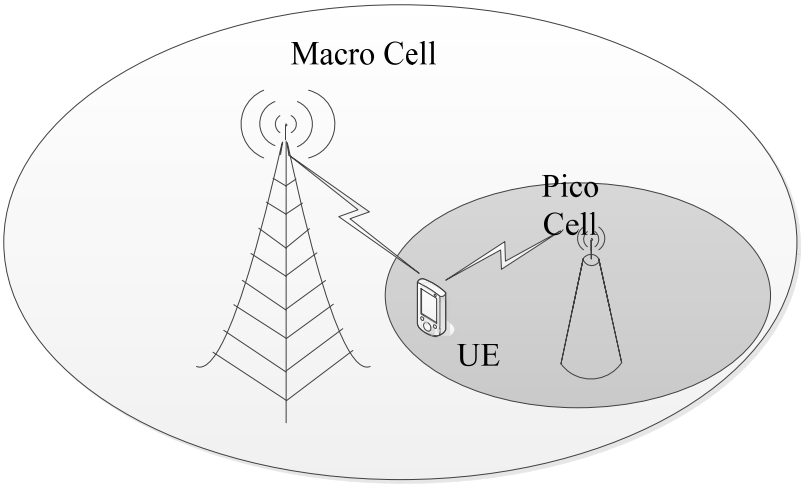

Figure 6.1 Inter-cell Interference between Macro and Pico Cell

Fig. 6.1 is an illustration of typical inter-cell interference scenario between macro and pico cells, in which the LTE service is delivered to the UE via pico cell and the downlink signal from macro cell interferes the UE at the edge of pico cell. To alleviate the inter-cell interference, the ABS is transmitted by the macro cell, during which only certain control signals are transmitted, such as CRS. However, the CRS still cause interference to the UE. Fig. 6.2 shows the received signal of one resource block (RB) with one interference cell. As shown in this figure, the CRS signal from neighboring macro cell overlaps the data resource elements (REs) in the time and frequency grid. Due to the STO and CFO between the interfering cell and UE, the received interfering signal suffers STO and CFO as shown in Fig. 6.2.

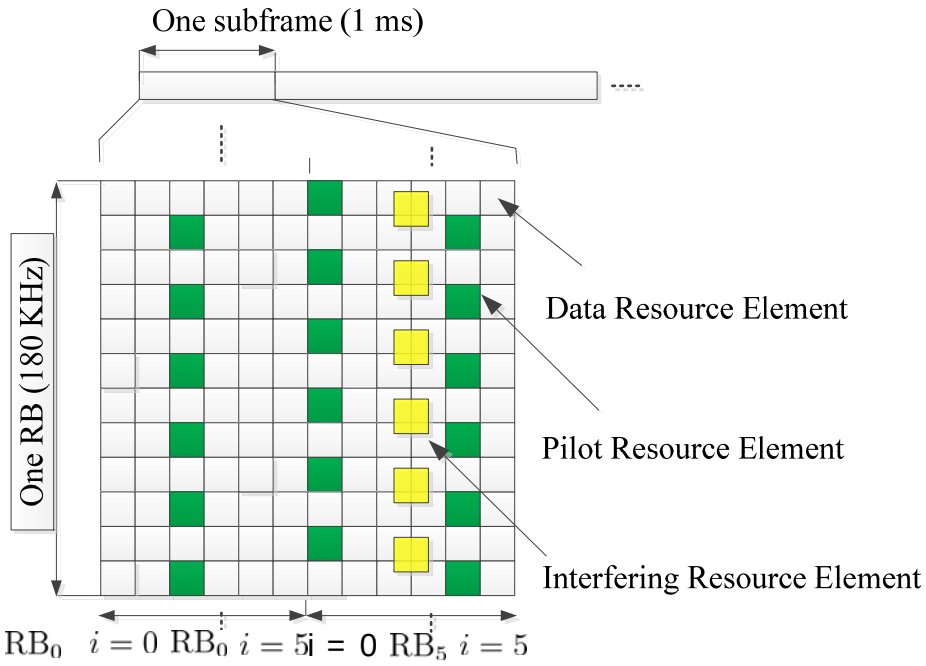

Figure 6.2 Received signal in time and frequency grid

The LTE downlink transmission employs OFDM modulation, in which the frequency domain signal $X_{i,k}$ of i^{th} OFDM symbol is transferred to time domain signal $x_i(n)$ via N-point Fast Fourier Transform (FFT):

$$\begin{aligned} x_i(n) &= \frac{1}{\sqrt{N}} \sum_{k=0}^{N-1} X_{i,k} e^{j2\pi nk/N} \\ &= \frac{1}{\sqrt{N}} \sum_{k=0}^{N-1} (d_{i,k} + p_{i,k}) e^{j2\pi nk/N} \end{aligned} \tag{6.1}$$

where $d_{i,k}$ and $p_{i,k}$ represent the data and pilot respectively.

Then the signal is transmitted over a multipath propagation channel take into account the additive white Gaussian noise (AWGN). At the receiver side, the received signal can be written as:

$$y_i(n) = \sum_{l=0}^{L-1} h_l x_i(n - \tau_l) + w(n) \tag{6.2}$$

where h_l and τ_l are the gain and the delay of the l^{th} path, respectively; and $w(n)$ is the AWGN. Due to the STO and CFO, the corrupted signal in the case of inter-cell interference is:

$$\begin{aligned} y_i(n) &= y_i^{(0)}(n) + y_i^{(1)}(n) + w(n) \\ &= \frac{1}{\sqrt{N}} \sum_{k=0}^{N-1} H_{i,k}^{(0)} X_{i,k}^{(0)} e^{j2\pi nk/N} + \\ &\quad \frac{1}{\sqrt{N}} \sum_{k=0}^{N-1} H_{i,k}^{(1)} X_{i,k}^{(1)} e^{j2\pi (n-d)(k+f_\psi)/N} + \\ &\quad + w(n) \end{aligned} \tag{6.3}$$

where $y_0^{(0)}(n)$ and $y_0^{(1)}(n)$ are the serving and interfering signal respectively; $H_{i,k}^{(0)}$ and $H_{i,k}^{(1)}$ are the frequency response of the serving and interfering channel; d and f_ψ is the relative timing and frequency offset between the interfering and UE cell. After applying the N-point FFT, the OFDM symbol is given by [36]:

$$\begin{aligned} Y_{i,k} &= Y_{i,k}^{(0)} + Y_{i,k}^{(1)} \\ &= H_{i,k}^{(0)} X_{i,k}^{(0)} + \sum_{n=-N/2}^{N/2} e^{\frac{j2\pi nd}{N}} \cdot H_{i,n}^{(1)} X_{i,n}^{(1)} \Phi_n + W_{i,k} \end{aligned} \tag{6.4}$$

where $H_{i,k}^{(0)}$ and $H_{i,k}^{(1)}$ denote the channel coefficients of serving and interfering cell at k^{th} subcarrier respectively; Φ_i stands for the inter-carrier interference (ICI). During the ABS, only certain control signal is transmitted and the CRS signal from interfering cell overlaps the data REs of serving cell as shown in Fig. 6.2. The signal model at the data RE of the serving cell with interference can be written as:

$$Y_{i,k} = H_{i,k}^{(0)} d_{i,k}^{(0)} + \sum_{n=-N/2}^{N/2} e^{\frac{j2\pi nd}{N}} H_{i,n}^{(1)} p_{i,n}^{(1)} \Phi_n + W_{i,k} \tag{6.5}$$

According to Eq. (6.5), the relative timing offset d between interfering and serving cell causes phase shift $e^{\frac{j2\pi nd}{N}}$ on n^{th} subcarrier. The terms Φ_n in Eq. (6.5) arises from CFO term f_ψ, which results in inter-carrier interference (ICI). This model shows single-input single-output (SISO) antenna case only. The multiple-input multiple-output (MIMO) antenna case can be easily derived based on Eq. (6.5). However, the number of RE will increase since the number of interference CRS increases with number of antenna ports, which results in more severe interference. These problems will be addressed in Section 6.3.

6.3 Interference cancellation algorithm

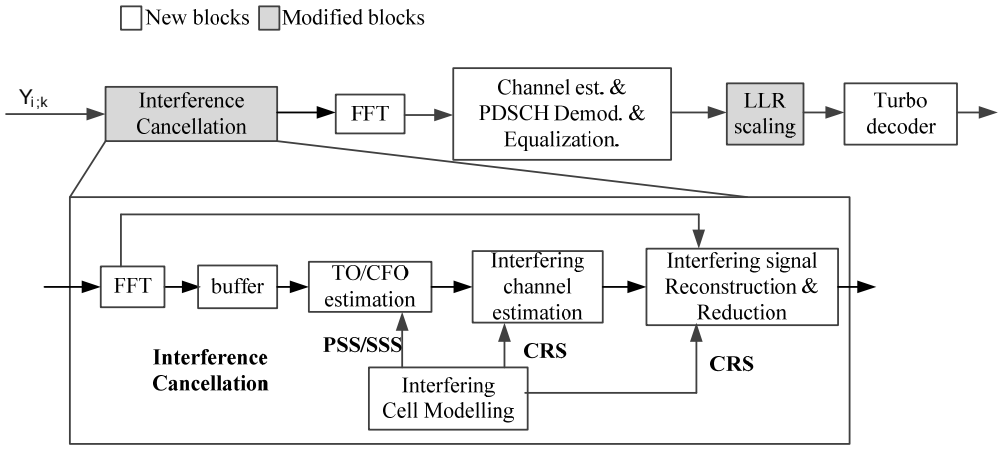

Figure 6.3 CRS Interference Cancellation Receiver Architecture

The proposed cancellation algorithm is shown in Fig. 6.3. Based on the conventional LTE receiver modules, this algorithm intoduces the following parts: TO/CFO estimation, interfering channel estimation, interfering cell modeling and interfering signal reconstruction and reduction. In CFO/TO estimation, the relative frequency offset and timing offset between the interfering cell and serving cell is estimated by using PSS/SSS generated in interfering cell modeling. Next, the interfering channel estimation is conducted based on the compensated signal. The interfering signal is then reconstructed based on the previous estimation and subtracted from the received signal. Finally, due to the inaccurate estimation of SNR, the log-likelihood ratio (LLR) is scaled to adjust the SNR mismatch.

6.3.1 TO/CFO estimation

The objective of this module is to retrieve interfering OFDM symbol timing and estimate the CFO of the interfering cell. Many timing and frequency synchronization algorithms have been developed. Most of them exploit the periodic nature of the time-domain signal by using cyclic prefix (CP) [129-131] or pilot data [132, 133]. However, the data REs are zero in ABS, which significantly reduces the power of CP. The low SNR of CP makes it difficult for both timing and frequency synchronization. However, thePSS and SSS can be used. The PSS and SSS are at the last and second-last symbol in the time slot 0 and slot 10 as shown in Fig. 6.4. The PSS $\mathrm{ppp(n)}$ and SSS $\mathrm{sss(n)}$ in frequency domain is given by:

$$pss(n) = \begin{cases} e^{\frac{j\pi un(n+1)}{63}} & n = 0, 1, \cdots, 30 \\ e^{\frac{j\pi u(n+1)(n+2)}{63}} & n = 31, 32, \cdots, 61 \end{cases}$$

And

$$sss(2n) = \begin{cases} s_0^{(m_0)}(n)c_0(n) & \text{time slot } 0 \\ s_1^{(m_1)}(n)c_0(n) & \text{time slot } 10 \end{cases}$$

$$sss(2n+1) = \begin{cases} s_1^{(m_1)}(n)c_1(n)z_1(m_0)(n) & \textit{time slot } 0 \\ s_0^{(m_0)}(n)c_1(n)z_1(m_1)(n) & \textit{time slot } 10 \end{cases}$$

where u is 25, 29 or 34 corresponding to the physical layer identity $N_{ID}^{(2)}$; m_0 and m_1 are derived from the physical layer cell identity group$N_{ID}^{(1)}$. Because the entire PSS/SSS symbol only contains PSS/SSS signal, which means the PSS/SSS symbol could be used for synchronization. As the time domain PSS/SSS symbol can make full use of CP and gives better performance, this paper adopts time domain synchronization method. The timing and frequency offset can be estimated by utilizing the cross-correlation of PSS/SSS [131]:

$$\left\{\hat{d}, \hat{f}_\Delta\right\} = \arg\max_{d, f_\Delta} \left(|C(d, f_\Delta)|\right) \tag{6.6}$$

where

$$C(d, f_\Delta) = \sum_{d=1}^{N/2} s_i^*(n) r(n+d) e^{\frac{-2\pi f_\Delta n}{N}} \tag{6.7}$$

and $r(n+d)$ is the received signal with a delay of d.

and $r(n)$ and $s_i(n)$ are the received and locally generated symbols which contain PSS/SSS. Note that the generation of PSS/SSS is based on the assumption of ideal cell search. The cell search algorithm in inter-cell interference scenario is beyond of the scope of this dissertation. After the timing and frequency synchronization of the interfering signal, the interfering channel response can be estimated.

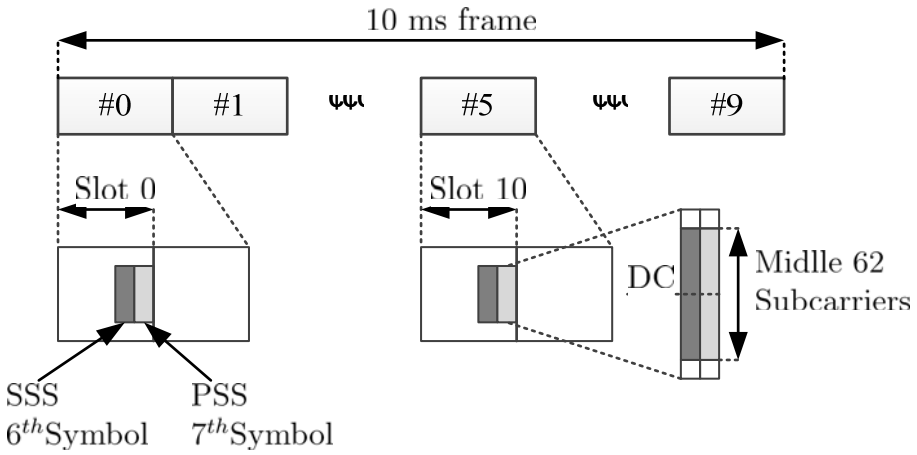

Figure 6.4 Synchronization Signal

6.3.2 Interfering channel estimation

Before interference cancellation, it's essential to estimate the NC CRS channel response. Based on the estimation of Eq. (6.6), the relative position of NC CRS on time-frequency grid is determined. When the NC CRS interferes to data/control RE of the SC, the NC CRS does not collide with SC CRS, namely non-colliding scenario. Otherwise, the NC CRS overlap SC CRS which causes colliding interference. In non-colliding scenario, the data/control RE can be viewed as noise which will be shown later. Whereas, the interference caused by collided CRS make is possible to estimate the interfering channel accurately since the SC CRS is known. Hence, the interfering channel estimation of these two scenarios will be treated separately.

- **Non-colliding scenario**

In this scenario, the data RE of SC can be regarded as interference for NC CRS REs. Hence, the CS CRS channel can be estimated by using some conventional methods. The channel estimation can be based on Lease Square (LS) or Minimum Mean-Square (MMSE) [117, 134]. The MMSE algorithm is show to shown 10-15 dB gain in signal-to-noise ratio (SNR) for the same mean square error of channel estimation over LS estimation [117]. However, the MMSE is more complex than

the LS algorithm. The proposed algorithm adopts LS method. After timing and frequency offset compensation, Eq. (6.5) can be approximated as:

$$Y_{i,k} = H_{i,k}^{(0)} d_{i,k}^{(0)} + H_{i,k}^{(1)} p_{i,k}^{(1)} + W_{i,k} \tag{6.8}$$

The interfering CRS sequence $p^{(1)}$ can be expressed from the following equation:

$$p^{(1)} = \frac{1}{\sqrt{2}}(1 - 2c(2n)) + j\frac{1}{\sqrt{2}}(1 - 2c(2n+1)) \tag{6.9}$$

where $c(n)$is generated by a length-31 Gold sequence, the state of which is initialized according to the cell ID, slot number and antenna port. Assuming that the UE conducts ideal cell search, the interfering CRS $p_{i,k}^{(1)}$ can be generated locally. Applying LS channel estimation, the estimate of interfering channel can be written as:

$$\hat{H}_{i,k}^{(1)} = Y_{i,k}/p_{i,k}^{(1)} = H_{i,k}^{(1)} + H_{i,k}^{(0)} d_{i,k}^{(0)}/p_{i,k}^{(1)} + W_{i,k}/p_{i,k}^{(1)} \tag{6.10}$$

According to Eq. (6.10), the data RE of serving cell $H_{i,k}^{(0)} d_{i,k}^{(0)}/p_{i,k}^{(1)}$ becomes interference whose power is relatively high. Hence, the estimate in Eq. (6.10) is inaccurate. Numeric studies in [135] show that the distribution of the interfering signal is close to Gaussian for larger RB size and non-Gaussian for smaller RB size. And the mean of the distribution converges to 0. Hence, the expectation of Eq. (6.10) can be derived as:

$$\begin{aligned}
\hat{H}_{i,k}^{(1)} &= \mathbb{E}\left\{Y_{i,k}/p_{i,k}^{(1)}\right\} \\
&= \mathbb{E}\left\{H_{i,k}^{(1)} + H_{i,k}^{(0)} d_{i,k}^{(0)}/p_{i,k}^{(1)} + W_{i,k}/p_{i,k}^{(1)}\right\} \\
&= \mathbb{E}\left\{H_{i,k}^{(1)}\right\} + \mathbb{E}\left\{H_{i,k}^{(0)} d_{i,k}^{(0)}/p_{i,k}^{(1)}\right\} \\
&\quad + \mathbb{E}\left\{W_{i,k}/p_{i,k}^{(1)}\right\} \\
&\approx \mathbb{E}\left\{H_{i,k}^{(1)}\right\}
\end{aligned} \tag{6.11}$$

Eq. (6.11) gives a good estimation of mean value of interfering channel. Hence, the mean value of the interfering channel can be estimated by using a moving average window in the time dimension as shown in Fig. 6.5. If the moving average window length M is within the coherence time of the channel, $\hat{H}_{i,k}^{(1)}$ could be approximated by $\mathbb{E}\left\{\hat{H}_{i,k}^{(1)}\right\}$. The procedure of the interfering channel estimation is shown in Fig. 6.5:

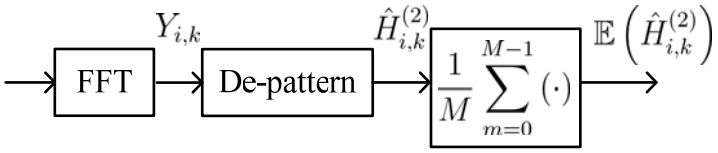

Figure 6.5 Non-colliding Interfering Channel Estimation

In MIMO and unknown bandwidth scenarios, The interference cancellation algorithm should be aware of the correct antenna number and bandwidth of the interference. However, this information is not available at the UE before UE decides to handover to that cell. Therefore, the interference cell antenna number and bandwidth need to be estimated at the UE.

This paper proposes a simple way is that IC control block module always set the maximum possible bandwidth and antennas, i.e. 20 MHz and 4 antennae, and antenna for LTE Release 10. Then, the interfering cell channel estimation and interference modelling block estimates channel accordingly. If the actual bandwidth is smaller than 20MHz, the power of the CRS outside the signal band will be to zero. The estimate of the channel that is out of the signal bandwidth is:

$$\begin{aligned}\mathbb{E}\left\{\hat{H}_{i,k,out}^{(1)}\right\} &= \mathbb{E}\left\{H_{i,k}^{(1)}\right\}_{out} + \mathbb{E}\left\{H_{i,k}^{(0)} d_{i,k}^{(0)} / p_{i,k}^{(1)}\right\}_{out} \\ &\quad + \mathbb{E}\left\{W_{i,k}/p_{i,k}^{(1)}\right\}_{out} \\ &\approx 0 + 0 + 0\end{aligned} \tag{6.12}$$

Eq. (6.12) indicates that the estimate of the neighbour cell channel could filter out the interference and noise by moving average method. So the power of the channel estimates is a reliable measurement to detect the signal bandwidth. The similar approach could be applied to the antenna number detection as well.

- **Colliding scenarios**

When the NC CRS collides with SC CRS, the received signal becomes:

$$Y_{i,k} = H_{i,k}^{(0)} p_{i,k}^{(0)} + H_{i,k}^{(1)} p_{i,k}^{(1)} + W_{i,k} \tag{6.13}$$

There are two unknown channel parameters $H_{i,k}^{(0)}$ and $H_{i,k}^{(1)}$ in this equation, which means using the SC CRS and NC CRS is insufficient to estimate the channel. In this scenario, it can be assumed that the UE channel is slow time variant in which the channel stays stationary during several consecutive symbols, i.e. $H_{i,k} = H_{i-1,k}$. In practice, the pico cell will be deployed in indoor environment where the assumption is true in most of time. Considering two consecutive collided symbols that contain CRS, the received signal is

$$\begin{bmatrix} Y_{i,k} \\ Y_{i-1,k} \end{bmatrix} = \begin{bmatrix} p_{i,k}^{(0)} & p_{i,k}^{(1)} \\ p_{i-1,k}^{(0)} & p_{i-1,k}^{(1)} \end{bmatrix} \begin{bmatrix} H_{i,k}^{(0)} \\ H_{i,k}^{(1)} \end{bmatrix} + \mathbf{W}_{i,k} \tag{6.14}$$

The channel estimation can be calculated by using LS method:

$$\begin{bmatrix} \hat{H}_{i,k}^{(0)} \\ \hat{H}_{i,k}^{(1)} \end{bmatrix} = \begin{bmatrix} p_{i,k}^{(0)} & p_{i,k}^{(1)} \\ p_{i-1,k}^{(0)} & p_{i-1,k}^{(1)} \end{bmatrix}^{+} \begin{bmatrix} Y_{i,k} \\ Y_{i-1,k} \end{bmatrix} \tag{6.15}$$

where $\left[\cdot\right]^{+}$ is the matrix pseudo-inverse operation. Both the inferring channel and serving channel can be estimated. Though the above equation gives a solution for SISO system, it is easy to be applied in the MIMO systems. The receiver can

switch between non-colliding and colliding algorithm according to the timing-frequency offset.

6.3.3 Interfering signal reconstruction and reduction

After estimating TO/CFO and channel response, the estimated of interference signal can be reconstructed based on the locally generated time domain CRS. The relative timing offset d is potentially larger than the duration of CP which causes ISI within the OFDM window of desired signal. Hence, reconstructing frequency domain interfering signal symbol by symbol could result in inaccurate interference cancellation. This algorithm reconstructs the interfering signal in the time domain and subtracts it from the received signal in time domain directly:

$$\hat{y}^{(0)}(n) = y(n) - \hat{y}^{(1)}(n + \hat{d}) e^{\frac{-j2\pi \hat{f}_{\psi} n}{N}} * \hat{h}_l \tag{6.16}$$

where

$$\hat{h}_l = FFT \left\{ \hat{H}_i^{(1)} \right\}$$

6.3.4 LLR scaling

In this LTE receiver, the log-likelihood ratio (LLR) is calculated for bit-rate decoding, which is based on the post-equalized SINR per RE as shown in Fig. 6.3. The log-likelihood of data symbol is defined as:

$$\log F\left(Y_{i,k} | S_{i,k}\right) = \frac{-\|Y_{i,k} - H_{i,k} S_{i,k}\|^2}{2\sigma_n^2} \tag{6.17}$$

Then the LLR of the turbo decoder is defined as:

$$L_{i,n} = \max_{S_{i,k} \in \mathbf{S}_n^1} \left[\log F\left(Y_{i,k} | S_{i,k}\right)\right] - \max_{S_{i,k} \in \mathbf{S}_n^0} \left[\log F\left(Y_{i,k} | S_{i,k}\right)\right] \tag{6.18}$$

where $\mathbf{S}_n^0$ and $\mathbf{S}_n^1$ is the constellation symbol sets whoes n^{th} bit is 0 and 1 respectively. It shows that the LLR calculation is inaccurate if there exists SNR estimation error. Denoting the SNR estimation mismatch as:

$$\zeta_m = \frac{\mathrm{SNR}_{est}}{\mathrm{SNR}_{act}} = \frac{\sigma_n^2}{\hat{\sigma}_n^2} \tag{6.19}$$

where σ_n^2 and $\hat{\sigma}_n^2$ stands for the actual and estimated noise power respectively. Then the LLR should be scaled as:

$$\tilde{L}_{i,n} = \zeta_m L_{i,n} \tag{6.20}$$

In receiver, LLR scaling is applied after interference cancellation and the noise power is assumed to be flat across the whole signal bandwidth. Thus the LLR scaling factor can be represented by the post-equalized signal power. If IC can eliminate the interference, there will not be any interference at the LLR scaling stage. However, due to the inaccuracy of the neighbouring cell channel estimation, we cannott remove interference completely. When calculating the post-equalized SINR, the residual interference term is not seen. Therefore the LLR scaling factor at the data RE with interference needs to be compensated. In the numerical study, we find that when reducing the LLR value by 2 at RE with interference, we achieve the best results.

6.4 Simulation results

In this section, the performance of proposed IC algorithm will be evaluated. A typical two-cell interference scenario is simulated as shown in Fig. 6.1: The serving cell is set to deliver the data packet with 10 MHz bandwidth and different modulation and coding schemes (MCS), whereas the interfering cell transmits normal ABS with bandwidth of 5 MHz. During ABS, the NC CRS overlaps the data and pilot RE of SC signal which causes inter-cell interference. The power of NC CRS is set to equal to SC CRS. The desired and interfering signal pass through time varying channel with a delay spread smaller than the duration of CP.

In the simulation, the EVA [125] channel model with different Doppler frequency is adopted to investigate the IC performance in different channel conditions. The arriving time of desired and interfering signal is adjusted to evaluate the effect of relative timing offset. In addition, different CFO is applied to interfering signal to evaluate its effects. In order to generate correct PSS/SSS/CRS for IC, the user is assumed to conducts ideal cell search. Key simulation parameters are listed below:

Table 6.1 Key Simulation Parameters

Parameters	Serving Cell	Neighbour Cell
Bandwidth (MHz)	10	5
Antenna Port	SISO/SIMO	SISO
Relative Power (dB)	0	0
MCS	MCS 8/16	N/A
Channel Model	EVA 5/70/150/200	EVA 5/70/150/200
Channel Encoder	LTE Turbo Code	LTE Turbo Code

Fig. 6.5 (a)-(d) show BLER performance versus signal-to-noise ratio (SNR) in different IC scenarios. The MCS 8 and MCS 16 are adopted. The signal is transmitted via EVA channel with 5 Hz Doppler frequency at different SNR. The antenna multiplex mode is set to SIMO and 2×2 MIMO. The block error rate (BLER) selected as the performance criteria, and it is calculated based on 10000 block transmissions. For comparison, the BLER of interference-free-free and interfered transmission without IC are presented as reference in blue and grey curves respectively. The figure also shows the performance with IC in red curve. The effect of LLR scaling is also depicted in pink and yellow curve respectively.

By comparing the blue and grey curves in figure (a)-(d), the CRS interference causes performance degradation during the SNR range of interest. As the red curve shows, the proposed IC algorithm can significantly improves BLER performance which is nearly close to the interference-free case as the red curve for SIMO MCS 8, 16 and MIMO MCS 8. There is also considerable improvement for MIMO MCS 16, where the BLER is whith 2 dB than ideal situation. In addition, it can be found that LLR scaling brings some improvement after the IC. The pure

LLR scaling brings limited performance improvements as [53, 54] shown. However, the interference cancellation combined with LLR scaling yield best performance.

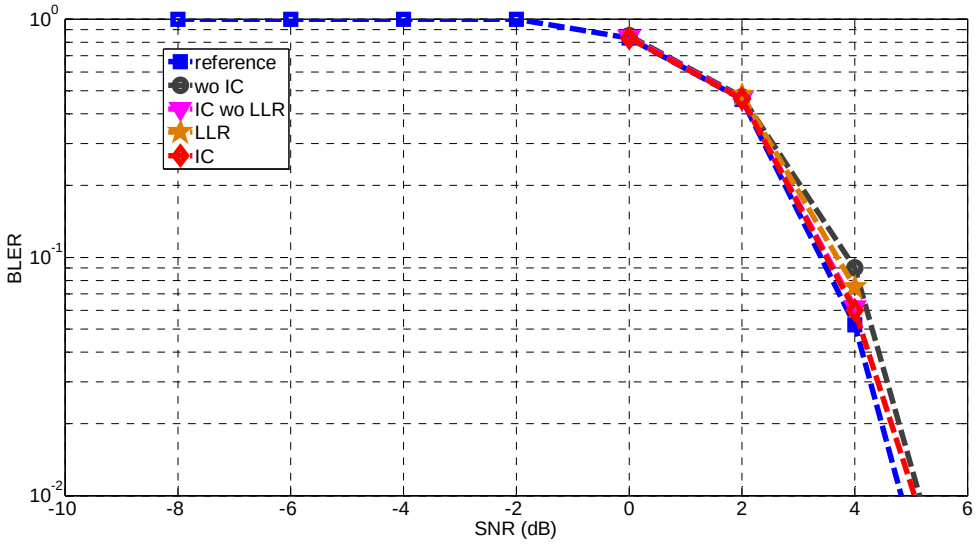

(a). SIMO, MCS 8

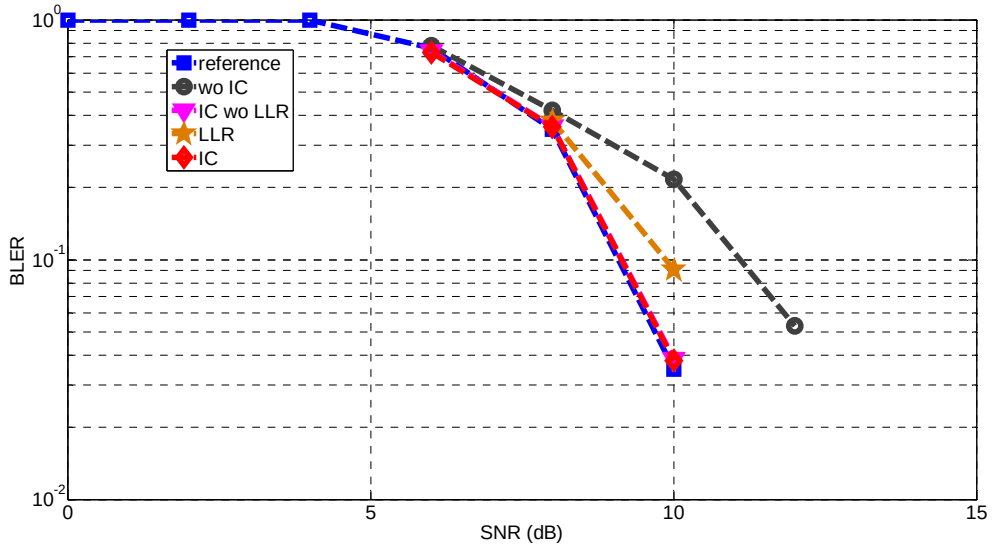

(b). SIMO, MCS 16

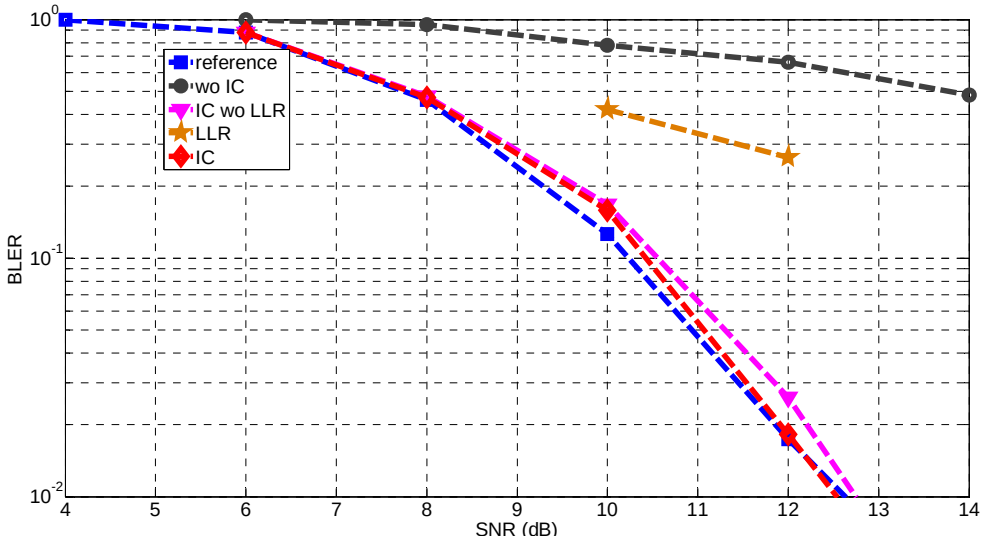

(c). MIMO, MCS 8

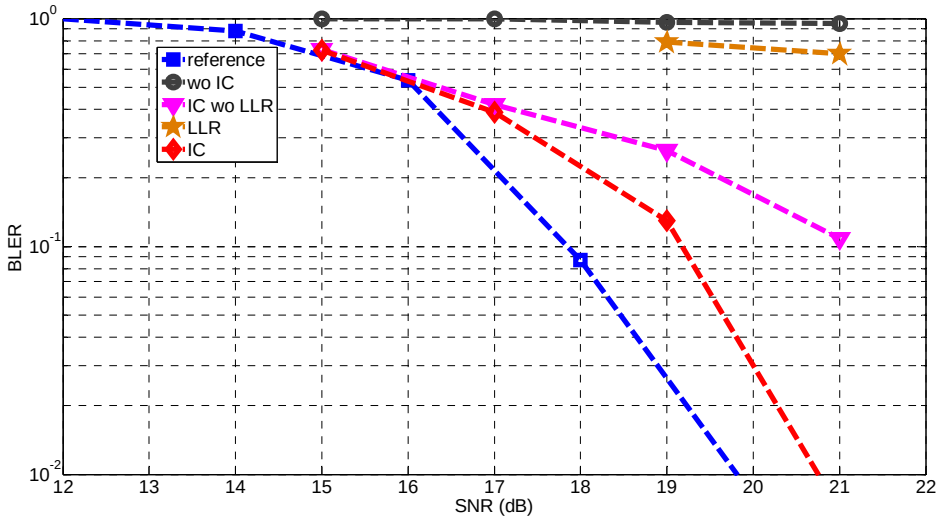

(d). MIMO, MCS 16

Figure 6.5 BLER performance versus SNR in dfferent IC scenario

Fig. 6.6 (a)–(d) show the BLER performance of different Doppler frequency scenarios. The SIMO MCS 18 modulation is adopted in this simulation. The Doppler frequency varies from 5 Hz to 200 Hz. The interference-free case is presented as a reference as shown in blue curve. The performance of interfering and IC case are shown in black and red curves respectively. According to Fig. 6.6 (a)-(b), the performance of proposed IC significantly improves the BLER performance for different SNR and Doppler frequencies which verifies the robustness of the IC algorithm.

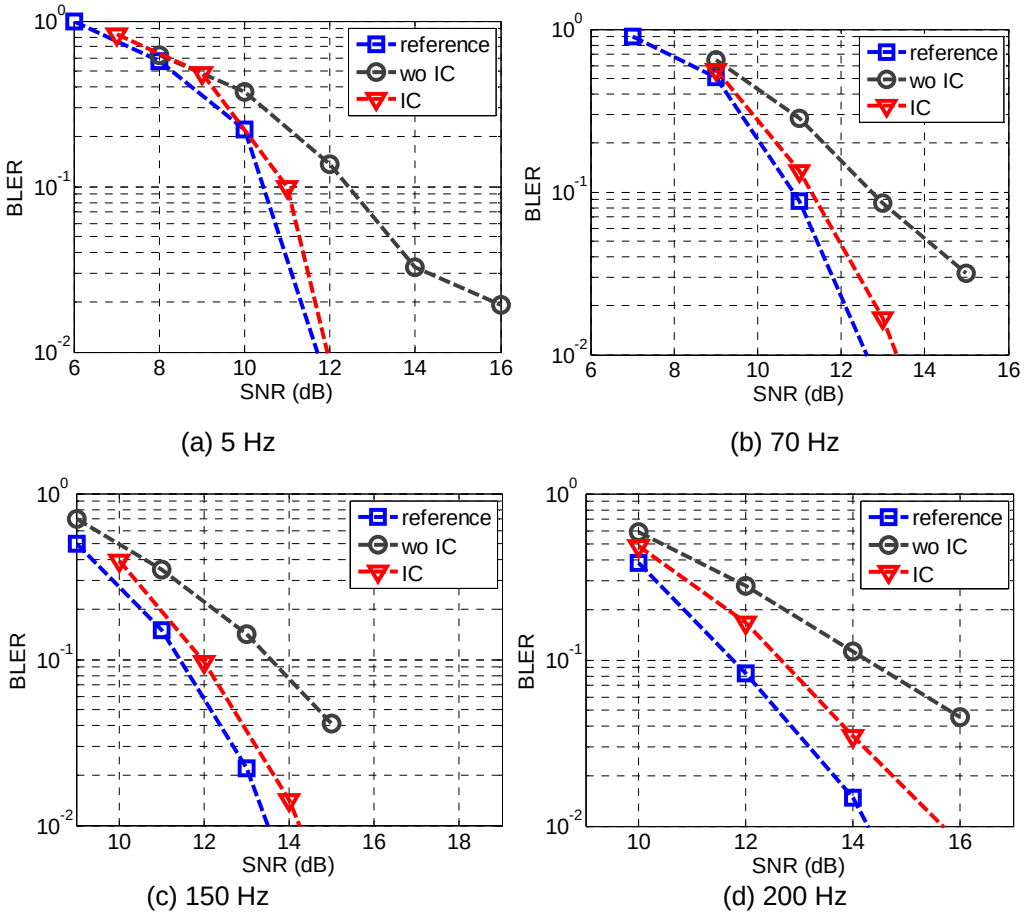

Figure 6.6 BLER Performance of Different Doppler Frequency Scenarios

Fig. 6.7 shows the impact of the average window length on the BLER performance in EVA 70 Hz. As shown in Fig. 6.7, the estimate of interfering channel $\hat{H}_{i,k}^{(1)}$ is approximated by averaging M times. This is based on the assumption that the length of moving average window is within the coherence time of the channel, otherwise it will bring inaccuracy due to the fast varying of the channel. In practice, this assumption is correct. This is because the UE which is attached to femto cell and on the cell edge is more likely to be slowly moving objects, such as pedestrian etc. High mobility objects, such as vehicles and high speed trains etc, will be attached to large cells. For the high mobility objects are attached femto cells, the period of attaching will be very short due to its high mobility. Hence, this algorithm will not face high mobility channels in most of the time. Because the statistical expectation in Eq. (6.11) is approximated by using moving average, the window length could not be too small. The figure shows that smaller window size gives better BLER performance. However, there will be no

significant different when window length is larger than 20.

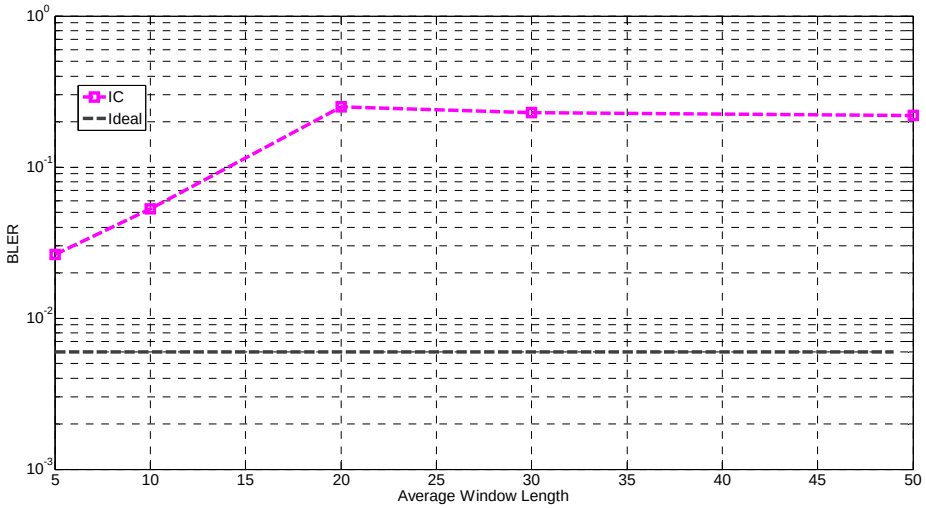

Figure 6.7 Effect of Average Window Length

Fig. 6.8 shows effect of CFO on the BLER performance. The performance of proposed IC algorithm and the combined IC (comIC) algorithm in [54] is implemented as a reference. In the author directly solve the channel matrix by using two consecutively received pilot symbols. It assumes that the channel remains invariant within a resource block. By de-mapping two consecutively received pilot symbols, the coefficient for MIMO channel could be calculated with the help of LS algorithm. Then a Wiener filter is applied to alleviate the influence of serving cell. Unlike comIC method, the proposed algorithm makes use of the statistics of channel to mitigate the influence of serving cell. According to this figure, the performance of comIC gradually degrades as the CFO increase. As contrary, there is no significant performance degradation for proposed IC algorithm. This verifies the effectiveness of frequency synchronization method when CFO is large.

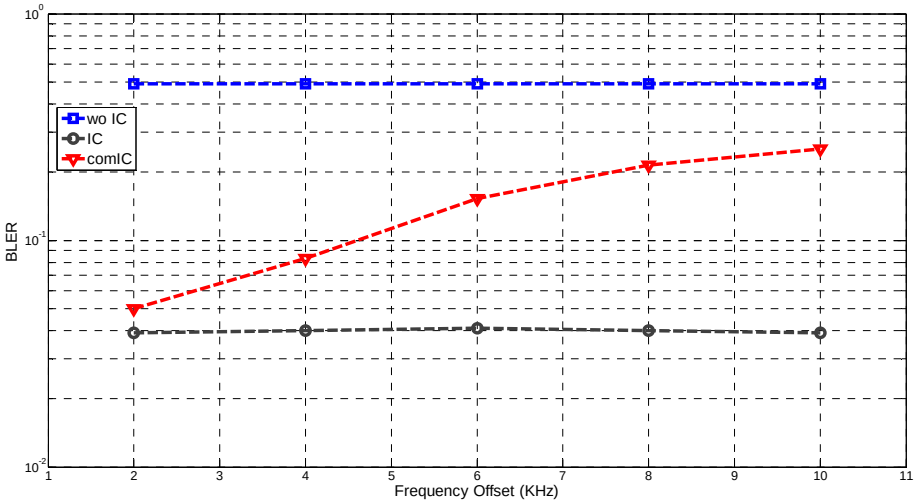

Figure 6.8 BLER Performance vs. Frequency Offset

Fig. 6.9 also shows the effect of TO on the BLER performance. MCS 22 modulation is adopted. The channel is set to EVA 5Hz and SNR is set to 16 dB. The performance of proposed IC shown in red curve. As a comparison, the combined IC (comIC) algorithm in [54] is shown in grey curve. The red curve shows that proposed IC achieves significant improvement when there is small delay or very large delay (the inference pilot almost overlaps with the adjacent symbol). When the delay is larger than half of OFDM symbol, the BLER of grey curve increase which means timing synchronization is required. The red curve shows that the IC with timing synchronization achieves robust performance within the interested timing offset range.

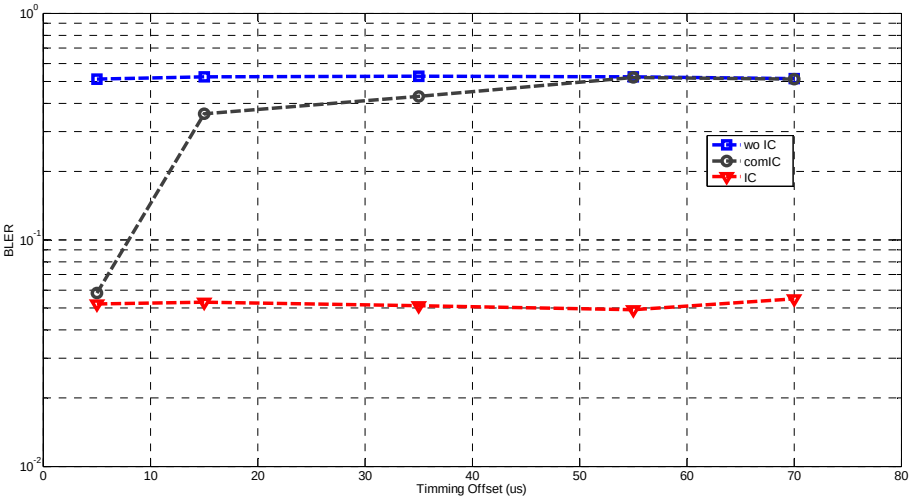

Figure 6.9 BLER Performance vs. Timing Offset

6.5 Conclusion

This chapter aims to cancel the inter-cell interference which is caused by the CRS during the ABS in cell edge. This chapter firstly studies the signal model, which takes into account the interference signal, channel effect, timing and frequency offset. Based on this model, an interference cancellation scheme is proposed: the timing and frequency offset is compensated firstly by using the PSS/SSS. Then, the interfering channel is estimated by utilizing the statistics of the channel. The interfering signal is then reconstructed locally. Finally, the interference is alleviated by subtracting the reconstructed interference signal and LLR scaling. The computer simulation results show that the proposed interference cancellation algorithm can achieve significant performance improvement in different channel conditions. Compared with the current algorithm which makes use of Wiener filter, the proposed method only conducts moving average, which consumes less computation complexity. So far, the simulation has verified that this algorithm works find when the SINR is 0 dB. However, when range extension is introduced, the SINR could varies from -9 dB to 9 dB, This means that the timing and frequency synchronization could face some problems as the current synchronization methos is only based on PSS/SSS. In the future, synchronization with the help of pilots will be investigated.

7. Conclusions

7.1 Discussions

In this dissertation, techniques for performance enhancement of LTE and beyond systems are studied. On the transmitter side, a self-IQ-demodulation based compensation scheme for FD I/Q imbalance is proposed. This scheme makes use of a power detection circuit of the generic DCT and deigns a special test signal. The signal and controlled LO leakage is transmitted first. The RF signal modulates itself in the diode and generates a baseband signal which carries the FD I/Q imbalance information. The training signal and LO is transmitted in a “time division” way which realizes self-IQ-demodulation. The I/Q imbalance parameter is resolved from the demodulated complex valued baseband data.

At the receiver side, an optimum OFDM receiver is designed to cope with the STO, CFO, SFO, and the doubly selective channel. The impact of CFO, STO and fading channel is mitigated in the coarse estimation stage where low computation hybrid algorithms are adopted. The dominant STO and CFO are firstly eliminated by the CP-based algorithm and the CFR is estimated by LS algorithm. Further to this, the residual CFO and SFO are eliminated using a pilot-based correlation method in the fine estimation stage. In order to combat the impact of residual frequency error and imperfection channel estimation caused by Doppler shift, a low computationally complex MMSE-DFE is developed. Moreover, a FPGA-based co-simulation platform is developed. This combines the advantages of MATLAB and FPGA, which speeds up the algorithm verification process.

A subspace-based SNR estimation algorithm is proposed for this receiver. This algorithm estimates the power in the signal space and noise space respectively and provides an accurate SNR estimates for the reliable equalizer and AMC. In order to mitigate the interference from neighbouring cells, the receiver also includes a

new CRS interference cancellation scheme. In this scheme, the CRS interference is cancelled with the help of SC data and channel statistics. LLR enhancement helps to improve the BLER performance. The impact of STO and CFO from NC is alleviated.

Compared with conventional techniques, this dissertation generally makes several improvements in terms of performance, cost and computational complexity. The proposed self-IQ-demodulation based compensation scheme yields a 50dB IRR which meets the requirements of most wideband systems. The conventional method manually calibrates the I/Q imbalance with the help of external instruments which is expensive and low in efficiency. By contrast, the proposed self-IQ-demodulation based compensation scheme only utilizes the internal diode and ADC and the calibration can be realized automatically with 10dB IRR improvement. This reduces the hardware cost and increases calibration efficiency.

The optimum OFDM receiver adopts several classical estimation algorithms and achieves typical EVM performance of 1.9% at SNR of 20 dB for 16QAM. The newly derived MMSE-DFE avoids the Cholesky decomposition in conventional MMSE-DFE by optimizing the cost function and only requires 5N multiplication operations and 3N addition operations. The sub-space based SNR estimation algorithm yielding estimation error stays below 0.09 even when it works in high mobility channels, whereas the conventional moving average methods become ineffective. It flexibly adjusts the decomposed signal and noise space, which makes it suitable for time-variant channel and flexible pilot allocation scenarios in LTE/beyond systems. In addition, the FPGA based co-simulation platform adopts universal data interface which makes it flexible to implement algorithm in FPGA. Co-simulation with hardware in chain speeds up the whole algorithm verification process.

For this proposed CRS interference cancellation algorithm, it improves the robustness when CFO and STO appear and the performance is enhanced by LLR puncturing compared with conventional algorithms.

7.2 Further work

In this thesis, LTE/beyond system performance enhancement techniques are theoretically investigated. A low cost FD transmitter I/Q imbalance compensation scheme is proposed leading to satisfactory IRR improvement. An optimum OFDM receiver is designed which reduces computational complexity and is suitable for hardware implementation. The CRS interference cancellation performance is also refined.

However, some improvements can be achieved with a future work:

1). I/Q imbalance estimation methods: The current estimation is based on digitized RF data from an 8 bit oscilloscope which hampers the estimation accuracy. And the higher order effect of the diode is simulated in MATLAB. Though it achieves a satisfactory result, performance needs to be verified In practice. Hence, the first stage could be conducting the experiment on a real wide band diode. Furthermore, a multiplier could be applied in the feedback path where the LO can be directly used for I/Q demodulation. The introduction of a multiplier is expected to significantly reduce harmonics and other interferences. Hence, other non-linear distortion could be estimated. Tthe second stage could be introducing a multiplier in the feedback path and developing automatic calibration algorithms for other non-linear distortions.

2). Receiver timing and frequency synchronization algorithm: The current receiver algorithm mitigates the impact of STO and CFO with the help of CP correlation. It is suitable for CP OFDM systems. Further LTE systems, isotropic orthogonal transform algorithm (IOTA) could be adopted which contains no CP [136]. Hence, more compatible timing and frequency synchronization algorithms need to be developed.

3). CRS interference cancellation: The current CRS interference cancellation assumes only one NC contributes to the interference. However, more cells will be deployed in further LTE releases which means more interfering cells. In this context, cancellation algorithms that can search for interfering cell and cancel interference from a specific cell are needed. In addition, the current interference cancellation assuming that cells search for interfering cell is correct. However, the synchronization channel from different cells overlaps, making it difficult to decode the cell ID. Hence, a reliable cell search in the interfering scenario is also needed. To summarize, further work on CRS interference cancellation would be:

A). Develop a multi-cell CRS interference cancellation algorithm. As the timing and frequency estimation could be inaccurate when SNR, future work will include accurate timing and frequency synchronization by making use of pilot symbols.

B). Develop a reliable cell search algorithm when several interfering cells are active.

Reference

[1] ITU. (2014). *Key 2005-2014 ICT data for the world by geographic regions and by level of development*. Available: http://www.itu.int/en/ITU-D/Statistics/Pages/stat/default.aspx?utm_source=twitterfeed&utm_medium=twitter.co.jp

[2] Y. Chen, "Soft Handover Issues in Radio Resource Management for 3G WCDMA Networks," 2003.

[3] C. K. Toh, *Ad hoc mobile wireless networks: protocols and systems*: Pearson Education, 2001.

[4] A. Electronics. *2G – 3G Cellular Wireless data transport terminology,* . Available: http://www.arcelect.com/2G-3G_Cellular_Wireless.htm

[5] D. Astely, E. Dahlman, G. Fodor, S. Parkvall, and J. Sachs, "LTE release 12 and beyond," *Communications Magazine, IEEE*, vol. 51, pp. 154-160, 2013.

[6] J.-S. Lee, Y.-W. Su, and C.-C. Shen, "A comparative study of wireless protocols: Bluetooth, UWB, ZigBee, and Wi-Fi," in *Industrial Electronics Society, 2007. IECON 2007. 33rd Annual Conference of the IEEE*, 2007, pp. 46-51.

[7] C. Evans-Pughe, "Bzzzz zzz [ZigBee wireless standard]," *IEE Review*, vol. 49, pp. 28-31, 2003.

[8] S. Fiehe, J. Riihijärvi, and P. Mähönen, "Experimental Study on Performance of IEEE 802.11 n and Impact of Interferers on the 2.4 GHz ISM Band," in *Proceedings of the 6th International Wireless Communications and Mobile Computing Conference*, 2010, pp. 47-51.

[9] 802.16.1a-2013. *IEEE Standard for WirelessMAN-Advanced Air Interface for Broadband Wireless Access Systems --Amendment 2: Higher Reliability Networks*. Available: http://standards.ieee.org/findstds/standard/802.16.1a-2013.html

[10] 3GPP TS 36.814, "Evolved Universal Terrestrial Radio Access (E-UTRA); Further advancements for E-UTRA physical layer aspects (Release 9)," v. 9.0.0 Mar. 2010.

[11] E. U. T. R. Access, "and Evolved Universal Terrestrial Radio Access Network (E-UTRAN); Overall description; Stage 2 (Release 10), 3GPP Technical Specification TS 36.300 V10. 2.0, Dec. 2010," ed.

[12] P. Bhat, S. Nagata, L. Campoy, I. Berberana, T. Derham, L. Guangyi, *et al.*, "LTE-advanced: an operator perspective," *Communications Magazine, IEEE,* vol. 50, pp. 104-114, 2012.

[13] J. K. Cavers and M. W. Liao, "Adaptive compensation for imbalance and offset losses in direct conversion transceivers," *Vehicular Technology, IEEE Transactions on,* vol. 42, pp. 581-588, 1993.

[14] J. Crols and M. S. J. Steyaert, "Low-IF topologies for high-performance analog front ends of fully integrated receivers," *Circuits and Systems II: Analog and Digital Signal Processing, IEEE Transactions on,* vol. 45, pp. 269-282, 1998.

[15] D. S. Hilborn, S. P. Stapleton, and J. K. Cavers, "An adaptive direct conversion transmitter," *Vehicular Technology, IEEE Transactions on,* vol. 43, pp. 223-233, 1994.

[16] B. Razavi, "Design considerations for direct-conversion receivers," *Circuits and Systems II: Analog and Digital Signal Processing, IEEE Transactions on,* vol. 44, pp. 428-435, 1997.

[17] M. Valkama, M. Renfors, and V. Koivunen, "Advanced methods for I/Q imbalance compensation in communication receivers," *Signal Processing, IEEE Transactions on,* vol. 49, pp. 2335-2344, 2001.

[18] L. Anttila, M. Valkama, and M. Renfors, "Frequency-Selective <emphasis>I/Q</emphasis> Mismatch Calibration of Wideband Direct-Conversion Transmitters," *Circuits and Systems II: Express Briefs, IEEE Transactions on,* vol. 55, pp. 359-363, 2008.

[19] K. Minseok, Y. Maruichi, and J. Takada, "Parametric Method of Frequency-Dependent I/Q Imbalance Compensation for Wideband Quadrature Modulator," *Microwave Theory and Techniques, IEEE Transactions on,* vol. 61, pp. 270-280, 2013.

[20] P. Mathecken, T. Riihonen, S. Werner, and R. Wichman, "Performance Analysis of OFDM with Wiener Phase Noise and Frequency Selective Fading Channel," *Communications, IEEE Transactions on,* vol. 59, pp. 1321-1331, 2011.

[21] T. M. Schmidl and D. C. Cox, "Robust frequency and timing synchronization for OFDM," *Communications, IEEE Transactions on,* vol. 45, pp. 1613-1621, 1997.

[22] M. Faulkner, T. Mattsson, and W. Yates, "Automatic adjustment of quadrature modulators," *Electronics Letters,* vol. 27, pp. 214-216, 1991.

[23] R. Marchesani, "Digital precompensation of imperfections in quadrature modulators," *Communications, IEEE Transactions on,* vol. 48, pp. 552-556, 2000.

[24] H. Xinping and M. Caron, "Efficient Transmitter Self-Calibration and Amplifier Linearization Techniques," in *Circuits and Systems, 2007. ISCAS 2007. IEEE International Symposium on*, 2007, pp. 265-268.

[25] J. Tuthill and A. Cantoni, "Efficient compensation for frequency-dependent errors in analog reconstruction filters used in IQ modulators," *Communications, IEEE Transactions on*, vol. 53, pp. 489-496, 2005.

[26] D. Lei, M. Zhengxiang, D. R. Morgan, M. Zierdt, and G. T. Zhou, "Frequency-dependent modulator imbalance in predistortion linearization systems: modeling and compensation," in *Signals, Systems and Computers, 2004. Conference Record of the Thirty-Seventh Asilomar Conference on*, 2003, pp. 688-692 Vol.1.

[27] S. A. Leyonhjelm and M. Faulkner, "The effect of reconstruction filters on direct upconversion in a multichannel environment," *Vehicular Technology, IEEE Transactions on*, vol. 44, pp. 95-102, 1995.

[28] M. Windisch and G. Fettweis, "Adaptive I/Q imbalance compensation in low-IF transmitter architectures," in *Vehicular Technology Conference, 2004. VTC2004-Fall. 2004 IEEE 60th*, 2004, pp. 2096-2100 Vol. 3.

[29] S. Burglechner, G. Hueber, and A. Springer, "On the estimation and compensation of IQ impairments in direct conversion transmitters," in *Wireless Technology, 2008. EuWiT 2008. European Conference on*, 2008, pp. 69-72.

[30] A. J. Goldsmith and P. P. Varaiya, "Capacity of fading channels with channel side information," *Information Theory, IEEE Transactions on*, vol. 43, pp. 1986-1992, 1997.

[31] L. J. Cimini, "Analysis and simulation of a digital mobile channel using orthogonal frequency division multiplexing," *Communications, IEEE Transactions on*, vol. 33, pp. 665-675, 1985.

[32] W. Jakes, "Microwave Mobile Channels," *New York: Wiley*, vol. 2, pp. 159-176, 1974.

[33] P. Schniter, "Low-complexity equalization of OFDM in doubly selective channels," *Signal Processing, IEEE Transactions on*, vol. 52, pp. 1002-1011, 2004.

[34] T. Strohmer and S. Beaver, "Optimal OFDM design for time-frequency dispersive channels," *Communications, IEEE Transactions on*, vol. 51, pp. 1111-1122, 2003.

[35] M. Rupp, C. Mehlführer, and M. Wrulich, *Evaluation of HSDPA and LTE: from testbed measurements to system level performance*: John Wiley & Sons, 2011.

[36] N.-L. Hung, T. Le-Ngoc, and K. Chi-Chung, "RLS-Based Joint Estimation and Tracking of Channel Response, Sampling, and Carrier Frequency Offsets for OFDM," *Broadcasting, IEEE Transactions on,* vol. 55, pp. 84-94, 2009.

[37] N.-L. Hung, T. Le-Ngoc, and N. H. Tran, "Iterative Receiver Design With Joint Doubly Selective Channel and CFO Estimation for Coded MIMO-OFDM Transmissions," *Vehicular Technology, IEEE Transactions on,* vol. 60, pp. 4052-4057, 2011.

[38] C. Jianwu, W. Yik-Chung, M. Shaodan, and N. Tung-Sang, "Joint CFO and Channel Estimation for Multiuser MIMO-OFDM Systems With Optimal Training Sequences," *Signal Processing, IEEE Transactions on,* vol. 56, pp. 4008-4019, 2008.

[39] M. Speth, S. A. Fechtel, G. Fock, and H. Meyr, "Optimum receiver design for wireless broad-band systems using OFDM. I," *Communications, IEEE Transactions on,* vol. 47, pp. 1668-1677, 1999.

[40] M. Speth, S. Fechtel, G. Fock, and H. Meyr, "Optimum receiver design for OFDM-based broadband transmission .II. A case study," *Communications, IEEE Transactions on,* vol. 49, pp. 571-578, 2001.

[41] K. Feher, *Advanced digital communications: systems and signal processing techniques*: Noble Publishing Corporation, 1997.

[42] N. Al-Dhahir and J. M. Cioffi, "Block transmission over dispersive channels: transmit filter optimization and realization, and MMSE-DFE receiver performance," *Information Theory, IEEE Transactions on,* vol. 42, pp. 137-160, 1996.

[43] A. Stamoulis, G. B. Giannakis, and A. Scaglione, "Block FIR decision-feedback equalizers for filterbank precoded transmissions with blind channel estimation capabilities," *Communications, IEEE Transactions on,* vol. 49, pp. 69-83, 2001.

[44] D. Williamson, R. A. Kennedy, and G. W. Pulford, "Block decision feedback equalization," *Communications, IEEE Transactions on,* vol. 40, pp. 255-264, 1992.

[45] H. Shousheng and M. Torkelson, "Effective SNR estimation in OFDM system simulation," in *Global Telecommunications Conference, 1998. GLOBECOM 1998. The Bridge to Global Integration. IEEE,* 1998, pp. 945-950 vol.2.

[46] H. Abeida, "Data-Aided SNR Estimation in Time-Variant Rayleigh Fading Channels," *Signal Processing, IEEE Transactions on,* vol. 58, pp. 5496-5507, 2010.

[47] X. Xiaodong, J. Ya, and Y. Xiaohu, "Subspace-based noise variance and SNR estimation for OFDM systems " in *Wireless Communications and Networking Conference, 2005 IEEE*, 2005, pp. 23-26 Vol. 1.

[48] A. Khandekar, N. Bhushan, T. Ji, and V. Vanghi, "LTE-Advanced: Heterogeneous networks," in *Wireless Conference (EW), 2010 European*, 2010, pp. 978-982.

[49] A. Damnjanovic, J. Montojo, W. Yongbin, J. Tingfang, L. Tao, M. Vajapeyam, *et al.*, "A survey on 3GPP heterogeneous networks," *Wireless Communications, IEEE*, vol. 18, pp. 10-21, 2011.

[50] S. Parkvall, A. Furuskar, and E. Dahlman, "Evolution of LTE toward IMT-advanced," *Communications Magazine, IEEE*, vol. 49, pp. 84-91, 2011.

[51] 3GPP R1-105335, "Details of almost blank subframes," Ericsson STEricsson,Oct. 2010.

[52] Qualcomm Inc. R4-102350, "Enabling communication in harsh interference scenarios," 3GPP-RAN WG4 AH#10-03, Bratislava, Jul. 2010.

[53] Qualcomm Inc R4-123313, "Link level simulations for FeICIC with 9dB cell range expansion," 3GPP-RAN WG4 #63, Prague, May 2012.

[54] H. Ming and X. Wen, "Macro-femto inter-cell interference mitigation for 3GPP LTE-A downlink," in *Wireless Communications and Networking Conference Workshops (WCNCW), 2012 IEEE*, 2012, pp. 75-80.

[55] B. E. Priyanto, S. Kant, F. Rusek, H. Sha, C. Jianjun, and C. Wugengshi, "Robust UE Receiver with Interference Cancellation in LTE Advanced Heterogeneous Network," in *Vehicular Technology Conference (VTC Fall), 2013 IEEE 78th*, 2013, pp. 1-7.

[56] 3GPP TS 36.211, "Evolved Universal Terrestrial Radio Access (E-UTRA): Physical channels and modulation," v 10.0.0 Dec. 2011.

[57] A. A. Abidi, "Direct-conversion radio transceivers for digital communications," *Solid-State Circuits, IEEE Journal of*, vol. 30, pp. 1399-1410, 1995.

[58] M. Suarez, O. Zlydareva, and E. P. Ling, "LTE/WiMAX multimode mobile transceiver, comparison of performances and power efficiency issues," in *Aerospace Conference, 2013 IEEE*, 2013, pp. 1-10.

[59] B. Razavi, "Challenges in portable RF transceiver design," *Circuits and Devices Magazine, IEEE*, vol. 12, pp. 12-25, 1996.

[60] L. Noor and A. Anpalagan, "Direct conversion receiver for radio communication systems," *Potentials, IEEE,* vol. 24, pp. 32-35, 2005.

[61] K. Martin, "Complex signal processing is not-complex," in *Circuits and Systems, 2004. MWSCAS '04. The 2004 47th Midwest Symposium on*, 2004, pp. xvi-xvi.

[62] N. Zimmermann, *Design and implementation of a broadband RF-DAC transmitter for wireless communications*: Universitätsbibliothek, 2011.

[63] J. G. Proakis, "Digital communications, 1995," ed: McGraw-Hill, New York.

[64] H. Hashemi, "Impulse response modeling of indoor radio propagation channels," *Selected Areas in Communications, IEEE Journal on,* vol. 11, pp. 967-978, 1993.

[65] E. U. T. R. Access, "Multiplexing and channel coding (Release 9). 3GPP Organizational Partners TS 36.212 Rev. 8.3. 0," ed: May, 2008.

[66] M. Pelcat, "Rapid prototyping and dataflow-based code generation for the 3GPP LTE enodeb physical layer mapped onto multi-core DSPs," Ph. D. dissertation, Dissertation, INSA Rennes, 210 p, 2010.

[67] A. Ghosh, R. Ratasuk, B. Mondal, N. Mangalvedhe, and T. Thomas, "LTE-advanced: next-generation wireless broadband technology [Invited Paper]," *Wireless Communications, IEEE,* vol. 17, pp. 10-22, 2010.

[68] P. Garcia, A. Ortega, J. De Mingo, and A. Valdovinos, "Nonlinear distortion cancellation in OFDM systems using an adaptive LINC structure," in *Personal, Indoor and Mobile Radio Communications, 2004. PIMRC 2004. 15th IEEE International Symposium on*, 2004, pp. 1506-1510 Vol.2.

[69] Z. W. Zheng, Y. Zhi-Xing, P. Chang-Yong, and Y.-S. Zhu, "Effects of nonlinear distortion and imperfect parameters estimation on the performance of OFDM-based DTTB systems," *Broadcasting, IEEE Transactions on,* vol. 51, pp. 237-243, 2005.

[70] A. Chini, W. Yiyan, M. El-Tanany, and S. Mahmoud, "Hardware nonlinearities in digital TV broadcasting using OFDM modulation," *Broadcasting, IEEE Transactions on,* vol. 44, pp. 12-21, 1998.

[71] I. T. Lu and C. Jiang, "Joint transmitter and receiver IQ imbalance estimation and compensation for OFDM systems," in *Radio and Wireless Symposium (RWS), 2010 IEEE,* 2010, pp. 476-479.

[72] S. Kexuan, I. Darwazeh, H. Li-Ke, and A. Jones, "Optimal pilot based frequency-dependent I/Q imbalance compensation for wideband direct-

conversion transmitters," in *Wireless Communications and Networking Conference (WCNC), 2012 IEEE*, 2012, pp. 226-231.

[73] A. Nassery, S. Byregowda, S. Ozev, M. Verhelst, and M. Slamani, "Built-In Self-Test of Transmitter I/Q Mismatch and Nonlinearity Using Self-Mixing Envelope Detector," *Very Large Scale Integration (VLSI) Systems, IEEE Transactions on*, vol. 23, pp. 331-341, 2015.

[74] G.-J. Van Rooyen, "Baseband compensation principles for defects in quadrature signal conversion and processing," University of Stellenbosch, 2005.

[75] P. Kiss and V. Prodanov, "One-tap wideband I/Q compensation for zero-IF filters," *Circuits and Systems I: Regular Papers, IEEE Transactions on*, vol. 51, pp. 1062-1074, 2004.

[76] L. Chia-Liang, "Impacts Of I/q Imbalance On Qpsk-ofdm-qam Detection," in *Consumer Electronics, 1998. ICCE. 1998 Digest of Technical Papers. International Conference on*, 1998, pp. 384-385.

[77] A. G. K. C. Lim, V. Sreeram, and W. Guo-Qing, "Digital compensation in IQ modulators using adaptive FIR filters," *Vehicular Technology, IEEE Transactions on*, vol. 53, pp. 1809-1817, 2004.

[78] J. Tuthill and A. Cantoni, "Optimum precompensation filters for IQ modulation systems," *Communications, IEEE Transactions on*, vol. 47, pp. 1466-1468, 1999.

[79] M. Valkama, *Advanced I/Q signal processing for wideband receivers: Models and algorithms*, 2001.

[80] B. Vargha, J. Schoukens, and Y. Rolain, "Static nonlinearity testing of D/A converters," in *Instrumentation and Measurement Technology Conference, 2001. IMTC 2001. Proceedings of the 18th IEEE*, 2001, pp. 1684-1689 vol.3.

[81] J. J. De Witt, "Modelling, estimation and compensation of imbalances in quadrature transceivers," PhD, University of Stellenbosch, 2011.

[82] L. Ding, M. Zhengxiang, D. R. Morgan, M. Zierdt, and G. T. Zhou, "Compensation of Frequency-Dependent Gain/Phase Imbalance in Predistortion Linearization Systems," *Circuits and Systems I: Regular Papers, IEEE Transactions on*, vol. 55, pp. 390-397, 2008.

[83] L. Anttila, P. Handel, and M. Valkama, "Joint Mitigation of Power Amplifier and I/Q Modulator Impairments in Broadband Direct-Conversion Transmitters," *Microwave Theory and Techniques, IEEE Transactions on*, vol. 58, pp. 730-739, 2010.

[84] U. Mengali and A. N. D'Andrea, *Synchronization techniques for digital receivers*: Springer, 1997.

[85] S. S. Haykin, *Adaptive filter theory*: Pearson Education India, 2008.

[86] V. P. G. Jiménez, Y. Jabrane, A. G. Armada, B. A. E. Said, and A. A. Ouahman, "High power amplifier pre-distorter based on neural-fuzzy systems for OFDM signals," *Broadcasting, IEEE Transactions on,* vol. 57, pp. 149-158, 2011.

[87] A. Prochazka and R. Neumann, "High Frequency Distortion Analysis of a Semiconductor Diode for CATV Applications," *Consumer Electronics, IEEE Transactions on,* vol. CE-21, pp. 120-130, 1975.

[88] R. W. Lucky, "Automatic equalization for digital communication," *Bell System Technical Journal, The,* vol. 44, pp. 547-588, 1965.

[89] A. Bo, Y. Zhi-Xing, P. Chang-Yong, G. Jian-hua, W. Yong, and L. Zhen, "On the synchronization techniques for wireless OFDM systems," *Broadcasting, IEEE Transactions on,* vol. 52, pp. 236-244, 2006.

[90] W. Lu, Z. Xian-Da, L. Pei-Sheng, and S. Yong-Tao, "A closed-form blind CFO estimator based on frequency analysis for OFDM systems," *Communications, IEEE Transactions on,* vol. 57, pp. 1634-1637, 2009.

[91] L. Jian, L. Guoqing, and G. B. Giannakis, "Carrier frequency offset estimation for OFDM-based WLANs," *Signal Processing Letters, IEEE,* vol. 8, pp. 80-82, 2001.

[92] H. Defeng and K. B. Letaief, "Carrier frequency offset estimation for OFDM systems using subcarriers," *Communications, IEEE Transactions on,* vol. 54, pp. 813-823, 2006.

[93] W. Zhu, Y. Li, X. Zhou, and J. Yu, "Blind Channel Estimation Algorithm with Simplified Implementation for OFDM System," in *Networks Security Wireless Communications and Trusted Computing (NSWCTC), 2010 Second International Conference on*, 2010, pp. 274-277.

[94] S. Ghadrdan, M. Ahmadian, S. Salari, and M. Heydarzadeh, "An improved blind channel estimation algorithm for OFDM systems," in *Telecommunications (IST), 2010 5th International Symposium on*, 2010, pp. 421-425.

[95] S. Coleri, M. Ergen, A. Puri, and A. Bahai, "Channel estimation techniques based on pilot arrangement in OFDM systems," *Broadcasting, IEEE Transactions on,* vol. 48, pp. 223-229, 2002.

[96] T. Hrycak, S. Das, G. Matz, and H. G. Feichtinger, "Practical Estimation of Rapidly Varying Channels for OFDM Systems," *Communications, IEEE Transactions on,* vol. 59, pp. 3040-3048, 2011.

[97] K. Yong-Hwa and L. Jong-Ho, "Joint Maximum Likelihood Estimation of Carrier and Sampling Frequency Offsets for OFDM Systems," *Broadcasting, IEEE Transactions on,* vol. 57, pp. 277-283, 2011.

[98] M. Morelli and M. Moretti, "Fine carrier and sampling frequency synchronization in OFDM systems," *Wireless Communications, IEEE Transactions on,* vol. 9, pp. 1514-1524, 2010.

[99] S. U. Qureshi, "Adaptive equalization," *Proceedings of the IEEE,* vol. 73, pp. 1349-1387, 1985.

[100] S. Haykin, *Communication systems*: John Wiley & Sons, 2008.

[101] K. Shi, E. Serpedin, and P. Ciblat, "Decision-directed fine synchronization in OFDM systems," *Communications, IEEE Transactions on,* vol. 53, pp. 408-412, 2005.

[102] A. Stamoulis, S. N. Diggavi, and N. Al-Dhahir, "Estimation of fast fading channels in OFDM," in *Wireless Communications and Networking Conference, 2002. WCNC2002. 2002 IEEE*, 2002, pp. 465-470.

[103] G. De Michell and R. K. Gupta, "Hardware/software co-design," *Proceedings of the IEEE,* vol. 85, pp. 349-365, 1997.

[104] S. Haykin, "Cognitive radio: brain-empowered wireless communications," *Selected Areas in Communications, IEEE Journal on,* vol. 23, pp. 201-220, 2005.

[105] K. Amiri, S. Yang, P. Murphy, C. Hunter, J. R. Cavallaro, and A. Sabharwal, "WARP, a Unified Wireless Network Testbed for Education and Research," in *Microelectronic Systems Education, 2007. MSE '07. IEEE International Conference on*, 2007, pp. 53-54.

[106] F. Classen, *Systemkomponenten für eine terrestrische digitale mobile Breitbandübertragung: Dissertation*: Shaker, 1996.

[107] M. Morelli, C. C. J. Kuo, and P. Man-On, "Synchronization Techniques for Orthogonal Frequency Division Multiple Access (OFDMA): A Tutorial Review," *Proceedings of the IEEE,* vol. 95, pp. 1394-1427, 2007.

[108] S. Wu and Y. Bar-Ness, "OFDM channel estimation in the presence of frequency offset and phase noise," in *Communications, 2003. ICC '03. IEEE International Conference on*, 2003, pp. 3366-3370 vol.5.

[109] K. Manolakis, D. M. Gutierrez Estevez, V. Jungnickel, W. Xu, and C. Drewes, "A Closed Concept for Synchronization and Cell Search in 3GPP LTE Systems," in *Wireless Communications and Networking Conference, 2009. WCNC 2009. IEEE*, 2009, pp. 1-6.

[110] R. Tesi, M. Hamalainen, and J. Iinatti, "Channel Estimation Algorithms Comparison for Multiband-OFDM," in *Personal, Indoor and Mobile Radio Communications, 2006 IEEE 17th International Symposium on*, 2006, pp. 1-5.

[111] V. K. Jones and G. C. Raleigh, "Channel estimation for wireless OFDM systems," in *Global Telecommunications Conference, 1998. GLOBECOM 1998. The Bridge to Global Integration. IEEE*, 1998, pp. 980-985 vol.2.

[112] Y. Young-Hwan, K. Joonbeom, and S. Hyoung-Kyu, "Pilot-Assisted Fine Frequency Synchronization for OFDM-Based DVB Receivers," *Broadcasting, IEEE Transactions on*, vol. 55, pp. 674-678, 2009.

[113] H. Meng-Han and W. Che-Ho, "Channel estimation for OFDM systems based on comb-type pilot arrangement in frequency selective fading channels," *Consumer Electronics, IEEE Transactions on*, vol. 44, pp. 217-225, 1998.

[114] L. Rugini, P. Banelli, R. C. Cannizzaro, and G. Leus, "Channel Estimation and Windowed DEF for OFDM with Doppler Spread," in *Acoustics, Speech and Signal Processing, 2006. ICASSP 2006 Proceedings. 2006 IEEE International Conference on*, 2006, pp. IV-IV.

[115] L. Favalli, P. Savazzi, and S. Somma, "Improved Block DFE Equalization for Mobile WiMAX OFDM Systems," in *Global Telecommunications Conference, 2007. GLOBECOM '07. IEEE*, 2007, pp. 3384-3388.

[116] S. Tomasin and N. Benvenuto, "A reduced complexity block iterative DFE for dispersive wireless applications," in *Vehicular Technology Conference, 2004. VTC2004-Fall. 2004 IEEE 60th*, 2004, pp. 1693-1697 Vol. 3.

[117] J. J. van de Beek, O. Edfors, M. Sandell, S. K. Wilson, and P. Ola Borjesson, "On channel estimation in OFDM systems," in *Vehicular Technology Conference, 1995 IEEE 45th*, 1995, pp. 815-819 vol.2.

[118] A. Ijaz, A. B. Awoseyila, and B. G. Evans, "Signal-to-Noise Ratio Estimation Algorithm for Advanced DVB-RCS Systems," *Broadcasting, IEEE Transactions on*, vol. 58, pp. 603-608, 2012.

[119] A. Wiesel, J. Goldberg, and H. Messer-Yaron, "SNR estimation in time-varying fading channels," *Communications, IEEE Transactions on*, vol. 54, pp. 841-848, 2006.

[120] G. T. R4-000020, "Simulation Results of CPICH RSCP/RSSI vrs. CPICH RSCP/ISCP," Jan 2000.

[121] J. Heiskala and J. Terry Ph D, *OFDM wireless LANs: A theoretical and practical guide*: Sams, 2001.

[122] J. G. Proakis, *Digital signal processing: principles algorithms and applications*: Pearson Education India, 2001.

[123] M. Wax and T. Kailath, "Detection of signals by information theoretic criteria," *Acoustics, Speech and Signal Processing, IEEE Transactions on,* vol. 33, pp. 387-392, 1985.

[124] M. A. R. Khan and D. S. Poskitt, "Description length based signal detection in singular spectrum analysis," *Monash Econometrics and Business Statistics Working Papers,* vol. 13, 2010.

[125] 3GPP TS 36.101, "Evolved universal terrestrial radio access (E-UTRA), user equipment (UE) radio transmission and reception," v .11.0 Mar. 2012.

[126] K. W. Cheung and S. W. Cheung, "Super-resolving multipath channels using modified MDL," *Electronics Letters,* vol. 34, pp. 43-45, 1998.

[127] S. N. S. Kshatriya, S. Kaimalettu, S. R. Yerrapareddy, K. Milleth, and N. Akhtar, "On interference management based on subframe blanking in Heterogeneous LTE networks," in *Communication Systems and Networks (COMSNETS), 2013 Fifth International Conference on*, 2013, pp. 1-7.

[128] S. Deb, P. Monogioudis, J. Miernik, and J. P. Seymour, "Algorithms for Enhanced Inter-Cell Interference Coordination (eICIC) in LTE HetNets," *Networking, IEEE/ACM Transactions on,* vol. 22, pp. 137-150, 2014.

[129] J. J. van de Beek, M. Sandell, and P. O. Borjesson, "ML estimation of time and frequency offset in OFDM systems," *Signal Processing, IEEE Transactions on,* vol. 45, pp. 1800-1805, 1997.

[130] M. Speth, D. Daecke, and H. Meyr, "Minimum overhead burst synchronization for OFDM based broadband transmission," in *Global Telecommunications Conference, 1998. GLOBECOM 1998. The Bridge to Global Integration. IEEE*, 1998, pp. 2777-2782 vol.5.

[131] K. Chi-Chung, M. Ronghong, and S. Miao, "A New Data Rotation Based CP Synchronization Scheme for OFDM Systems," *Broadcasting, IEEE Transactions on,* vol. 51, pp. 315-321, 2005.

[132] B. Jong-Seob and S. Jong-Soo, "Effective Symbol Timing Recovery Based on Pilot-Aided Channel Estimation for MISO Transmission Mode of DVB-T2 System," *Broadcasting, IEEE Transactions on,* vol. 56, pp. 193-200, 2010.

[133] W. Xianbin, T. T. Tjhung, W. Yiyan, and B. Caron, "SER performance evaluation and optimization of OFDM system with residual frequency and timing offsets from imperfect synchronization," *Broadcasting, IEEE Transactions on,* vol. 49, pp. 170-177, 2003.

[134] S. Bingulac, "On the compatibility of adaptive controllers," in *Proc. 4th Annu. Allerton Conf. Circuits and Systems Theory*, 1994, pp. 8-16.

[135] F. Cheng, C. Hongyu, M. Meng, and J. Bingli, "On Statistical Properties of Co-channel Interference in OFDM Systems," *Communications Letters, IEEE,* vol. 17, pp. 2328-2331, 2013.

[136] J. Du, P. Xiao, J. Wu, and Q. Chen, "Design of isotropic orthogonal transform algorithm-based multicarrier systems with blind channel estimation," *Communications, IET,* vol. 6, pp. 2695-2704, 2012.

Appedix A: The Effect of Resampler

In this simulation, the resampler is implemented in FPGA. The resampler is implemented based on a Aeroflex resampler IP core which uses polyphase FIR filters. The following figure shows the relationship between desired SFOand actual data offset over 1000000 data samples which respresent actual SFO. It can be seen that the co-simulation platform produces accurate SFO.

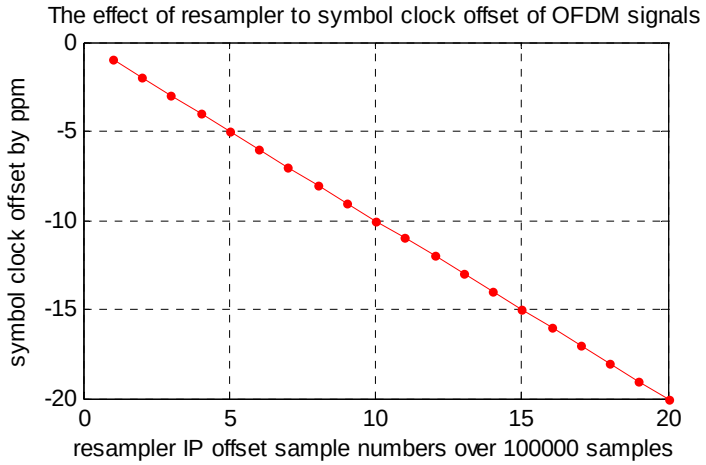

Appedix B: The Effect of Resampler to EVM of OFDM Signal

In this simulation, the co-simulation platform tunes the SFO from 1 to 20 ppm, which is minor values and can't be achieved by MATLAB. According to this figure, the SFO directly influences the output EVM which exhibits a linear relationship.

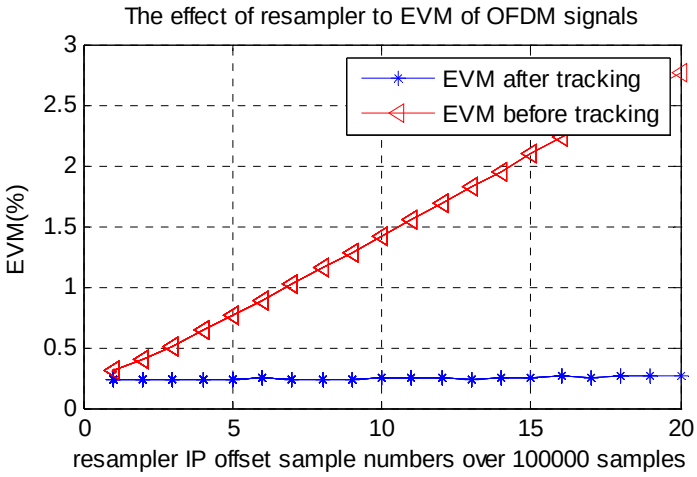
The effect of resampler to EVM of OFDM signals
EVM after tracking
EVM before tracking
EVM(%)
resampler IP offset sample numbers over 100000 samples
0
0.5
1
1.5
2
2.5
3
0
5
10
15
20